MONTAN
UNIVERSITÄT
LEOBEN

Chair of Materials Physics

Doctoral Thesis

In-situ investigations of hydrogen-material interaction

Agustina Massone

April 2021

MONTANUNIVERSITÄT LEOBEN
www.unileoben.ac.at

AFFIDAVIT

I declare on oath that I wrote this thesis independently, did not use other than the specified sources and aids, and did not otherwise use any unauthorized aids.

I declare that I have read, understood, and complied with the guidelines of the senate of the Montanuniversität Leoben for "Good Scientific Practice".

Furthermore, I declare that the electronic and printed version of the submitted thesis are identical, both, formally and with regard to content.

Date 08.04.2021

Signature Author
Agustina Massone

This work has been carried out under the scope of the COMET program within the K2 Center "Integrated Computational Material, Process and Product Engineering (IC- MPPE)" (Project No 859480). This program is supported by the Austrian Federal Ministries for Climate Action, Environment, Energy, Mobility, Innovation and Technology (BMK) and for Digital and Economic Affairs (BMDW), represented by the Austrian research funding association (FFG), and the federal states of Styria, Upper Austria and Tyrol.

Montanuniversität Leoben
Department of Materials Science, Chair of Materials Physics
Jahnstraße 12
A-8700 Leoben

Acknowledgments

I am pleased to acknowledge the help and contribution of many people over the past years in order to complete my dissertation.

First of all, I would like to thank Prof. Dr. Daniel Kiener, who gave me the opportunity to pursue my PhD, even when I had to come from another continent, and supported me during all these years. His knowledge, expertise, kindness and sense of humor contributed to a great experience and helped me to face many challenges in the way and to grow so much professionally. So, thank you for everything!

All the employees of the Department of Materials Physics and MCL contributed to the success of this work. The technicians and metallographers were of great help contributing with their great skills and being always willing to help. I also owe an immense gratitude to all my colleagues and friends from the institute. All of them made this time in a foreign country feel like home and I am proud to be part of this institution.

Finally, I would also like to thank my family and friends in Argentina for their unconditional support. They were always there for me to celebrate my accomplishments but also to cheer me up when things did not go as well as I wanted to. From the bottom of my heart, thank you all!

Abstract

With the necessity of finding alternative energy sources towards a greener world, new technical challenges are emerging. The improvement and development of existing or new materials is a requirement needed to implement these new alternatives energy sources. As hydrogen is believed to be a potential energy carrier, which can produce electricity with no emission of CO_2, the interaction of hydrogen with the mentioned materials has to be understood, so that these can perform safely in such environments. The effect of hydrogen on materials has been studied for many years but the different experimental methodologies and results obtained lead to different interpretations and controversies.

The main focus of this thesis was devoted to developing a novel experimental methodology to study hydrogen effects. A sophisticated novel approach, which combines in-situ hydrogen charging, tensile testing and high-resolution observation was developed. The method allows monitoring the deformation of any metallic sample without the risk of hydrogen outgassing. This is critical in materials with high hydrogen diffusivity that upon ex-situ hydrogen charging would lose the hydrogen once the test is started.

The novel in-situ method was applied to study the effect of hydrogen on three materials: a nickel-based alloy, a complex phase steel and a tungsten-based alloy. The mechanical properties, fracture surface morphologies and crack propagation behavior were investigated with and without hydrogen, proving different hydrogen embrittlement susceptibility degrees for each material. Moreover, hydrogen concentration was calculated with a simple analytical model and with a more sophisticated simulation model.

Finally, recently developed in-situ and in-operando methods were reviewed. All of these methods can be applied to study materials used in different hydrogen-related applications and should be considered in our pathway towards a green energy society.

Content

List of figures

List of abbreviations

H	Hydrogen
FC	Fuel cell
FCV	Fuel cell vehicle
HE	Hydrogen embrittlement
b.c.c.	Body-centered cubic
f.c.c.	Face-centered cubic
h.c.p.	Hexagonal closed-packed
IHE	Internal hydrogen embrittlement
HEE	Hydrogen environment embrittlement
HEDE	Hydrogen-induced decohesion
HELP	Hydrogen-enhanced localized plasticity
AIDE	Adsorption-induced dislocation emission
TEM	Transmission electron microscope
SEM	Scanning electron microscope
SSR	Slow strain-rate
I	Current
U	Voltage
AHSS	Advanced high-strength steels
CP	Complex phase

1. Motivation and aim of the work

With the present increasing global energy demand and the tendency towards a greener world, renewable energies have gained notable attention. Based on the current consumption rate, the present supply of fossil fuels may be finished in less than 50 years. Moreover, the emissions of CO_2 due to fuel burning contribute to the global climate change. In other words, the implementation of alternative energy sources is the only way towards a safe future.

Even though these new energy supplies could help solving the main environmental problems, their development and implementation present many challenges that need to be addressed. Hydrogen (H) plays an important role in greener energy supplies being an attractive alternative energy carrier, and one of the main challenges is related with the materials needed for this application. These materials have to be able to perform under H atmosphere without losing their properties.

Since many years, it has been known that H can have detrimental effects on the mechanical properties of certain metals, with the risk of provoking a failure of the components. Due to this reason, the study of H-material interactions is an ongoing research topic that has attracted the attention of many scientists due to the controversial findings and interpretations. Although many mechanisms of H effects have been proposed, there are still no agreements on how H acts. These controversies arise, from one side, due to the fact that it is very challenging to investigate the effect of such a small atom, and on the other side, that the results have a great dependency on the experimental setup used and the conditions of the tests.

Therefore, the aim of this work is to develop and implement a novel in-situ method to study H-material interactions in order to progress in the study of H-related effects to lay out pathways to design and/or modify materials with outstanding mechanical properties that can perform in H-environments.

2. Introduction

2.1. The importance of hydrogen

The depletion of fossil fuels and the global growth in energy demand is a factor of concern at the present, leading to the search of other sources of energy. As shown in Fig. 1a, the world electricity consumption is in constant increase and, as depicted in Fig. 1b, the majority of the energy supply comes from non-renewable energy sources, such as coal, oil and natural gas [1]. In contrast, the renewable energy sources provide only a small portion of the energy needed. In order to decrease CO_2 emissions and meet the energy demand in the long-term future, green energies have to be considered and H is believed to be a possible future energy source. Its ability to replace fossil fuels could address one of the world's major environmental problems [2].

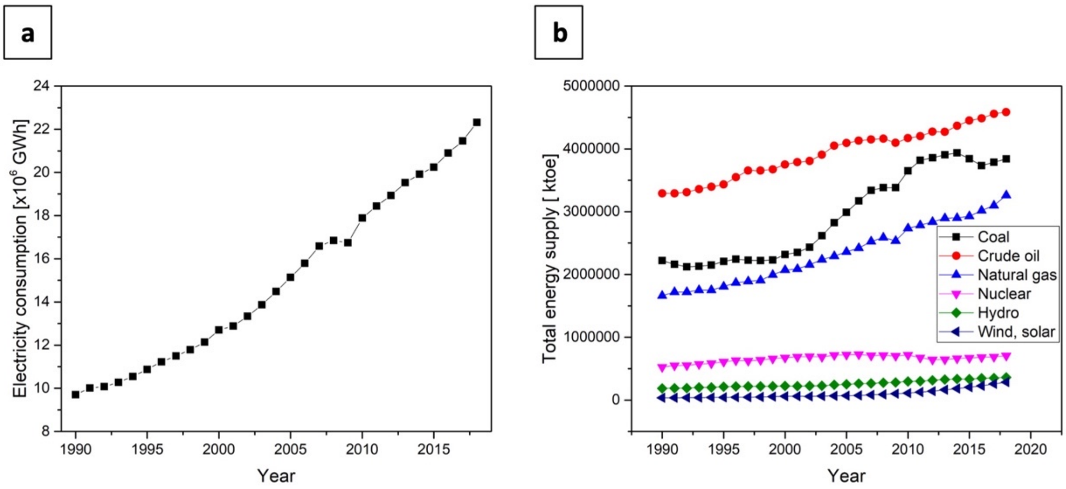

Figure 1. (a) Electricity consumption and (b) total energy supply. (Data taken from [1])

Fuel cells (FCs) are electrochemical devices that convert the chemical energy of a fuel, usually H, and efficiently produce electricity [3]. FCs produce electricity by the energy released from the reaction of H and oxygen atoms. Fig. 2 [4] shows a scheme of a very simple FC, which consists in two platinum electrodes submerged in an aqueous acid electrolyte. H_2 dissociates into protons and electrons in the left electrode, and the flow of electrons from left to right produces electricity. Electrons recombine with protons and oxygen when they reach the right electrode, producing water as product. FCs have many advantages compared to combustion technology. For instance, they are much smaller in size, more efficient, silent, have no or low environmental impact and can cover a wide range of applications [5].

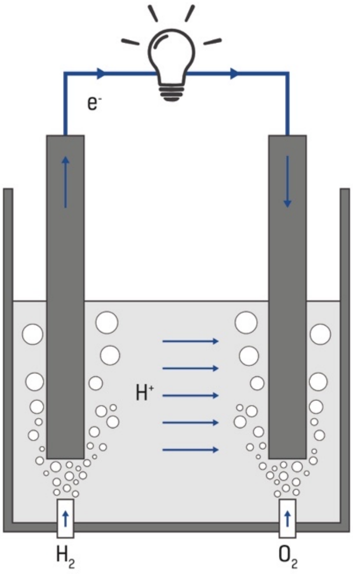

Figure 2. Scheme of a simple fuel cell

Currently, the main user of fossil derived products is the automotive industry [6] and FC vehicle (FCV) has been expected to improve the content of exhaust gas from vehicles, and thus contribute to the realization of a clean environment. The current target in the development of FCVs is high-pressure H storage at a final pressure of approximately 70 MPa [7]. Many metallic materials have been used for the high-pressure H storage. For example, aluminium alloys for a metallic liner in the H storage tank in FCV; a low-alloy steel for the metallic pressure vessel in the H station; stainless steels for the pressure valve, gauge, safety valve, spring and pipe; Ni-based superalloys for the H flow measuring instrument; and copper alloys for the reducing valve in the high-pressure system [7]. Metals used in these devices are exposed to H and thus, H embrittlement (HE) is the most critical factor for the safe use of FCVs.

Therefore, current regulations and standards highly restrict the component materials that can be exposed to high-pressure H. For example, only two types of metallic materials with excellent H resistance, a stainless steel and an aluminum alloy, are allowed according to the JARI (Japan Automobile Research Institute) standards [8]. The use of steels with body-centered cubic (b.c.c.) structure, which are highly susceptible to H, is restricted for those high-pressure H components [9]–[12]. However, for the widespread commercialization of H systems, carbon steels and low alloy steels are likely to be used to reduce production costs. To enable such H-sensitive steels to be used in commercial FCVs and H refuelling stations, it is necessary to understand the mechanism of H-induced degradation and how to prevent it.

H has an important role, not only in FCVs, but also in nuclear fusion energy. This is also an alternative for clean energy, as it has no emission of CO_2 and can produce around ten million times more energy than combustion of a carbon atom in coal [13]. Components within the reactor core have to withstand severe environmental conditions and must tolerate high temperatures, corrosion and radiation damage. For instance, the development of plasma facing materials is one of the challenges in the design of nuclear reactors. Their role is to protect the first wall from the high particle flux and transport thermal energy away from the surface [14]. The materials should, therefore, have high resistance to erosion by particle bombardment and high thermal conductivity. Fig. 3 shows the synergetic factors which act on plasma-facing components. Thermal loads can produce failure of joints, cracking and recrystallization; the bombardment of neutrons can produce irradiation damage; and the exposure to plasma can produce sputtering, H retention or even HE leading to component failures [15], [16]. Therefore, also for this application, the study of H-material interaction is of crucial importance.

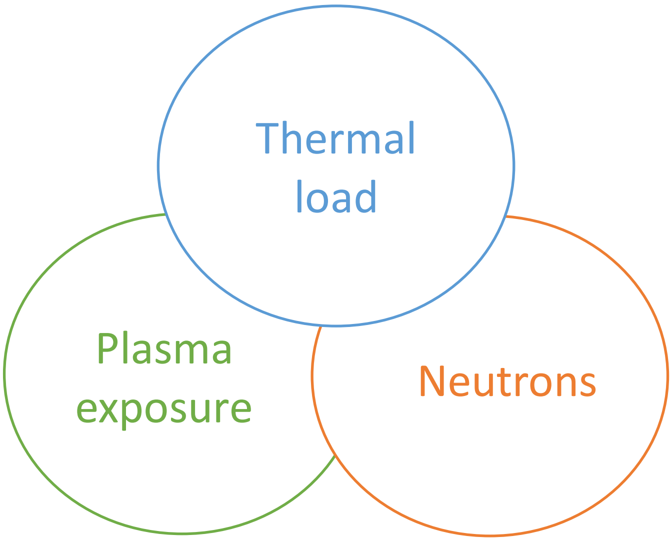

Figure 3. Synergetic factors on plasma-facing components

2.2. The effect of hydrogen on materials

The use of high-strength structural materials for a number of lightweight applications is nowadays a huge necessity. Besides FCVs, common uses of these materials include aerospace, marine, chemical process and medical applications. Even though developing materials with high tensile strength and high fracture toughness is possible, their outstanding properties can be negatively affected in the presence of H [17]–[24].

HE can be linked to corrosion and corrosion-controlled processes. The ductility and load bearing capacity of a component can be reduced by the introduction of H. Susceptible materials can have catastrophic brittle failures at stresses below the yield stress under the presence of H. HE does not affect all metallic materials equally and the susceptiblity depends on the materials' microstructure, the tensile strength, H concentration, among others [25]. The common HE features are an applied tensile stress and H dissolved in the material.

H can be loaded during service, but also upon fabrication. During service, it can be loaded in off-shore structures, which are structural pieces under cathodic protection; in gas storage and transport, as mentioned above; in acidic environment; among others. Regarding loading during fabrication, since the H solubility in the molten metal is much higher than when it is in the solid condition, H can be loaded in the metallurgical process [26]. It can also be loaded during fabrication processes, such as roll forming, machining, welding and drilling; but also in treatments like carbonizing, cleaning, phosphating and electro-plating [27], [28].

In most metals, the solubility of H at room temperature is very low. Anyways, its presence strongly influences their mechanical properties. Even at low temperatures, H atoms can diffuse rapidly through the crystal lattice and can thus be trapped at defects possessing a sufficient binding energy. However, the small number of H atoms causing this effect poses a big challenge on experimental studies.

The first reports about HE were published as early as 1875 by Johnson [29]. He saw that after immersing iron in different acids like hydrochloric or dilute sulphuric acid, the metal showed a decrease in toughness and strength but only temporary in character. Even though Johnson's description remains appropriate, the reduction in metal's mechanical properties has been shown to occur within a certain temperature and strain rate range and is reversible if H is removed [9], [30]–[34]. Nevertheless, since Johnson's first report, various strong views on the mechanisms of HE have been vigorously reviewed in the literature and the nature, causes and control of H-related degradation of metals have been studied by many scientists. This has led to numerous partly controversial findings and interpretations [1], [2], [3], [4]–[10], [11]–[20], [21]–[24].

HE susceptibility depends on the strength of the material and residual stresses; pressure, temperature and exposure time; applied strain rate and surface condition of the material; the concentration of H and H traps; the presence of metallic coatings; the microstructure of the material; heat treatment of the material, among others [44]. All of these factors can be grouped into three main groups, as shown in Fig. 4 [45]. These factors can be divided into mechanical, material and environmental factors and HE will only occur if the three of them coexist [45].

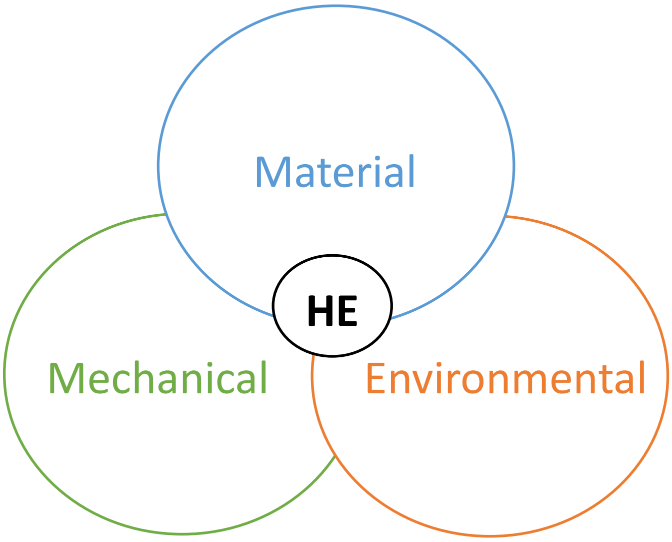

Figure 4. Description of HE interaction aspects

- Mechanical factors: These refer to the type of loading to which the material is subjected. This is related to whether it is a monotonic or cyclic loading, if there are residual stresses present, the load and state of stress, etc.

In general, the contact between H gas and a steel surface at room temperature, for example, cannot be considered as a problem. On the one hand, the dissociation constant of H_2 at room temperature is very high, and on the other hand, the diffusion coefficient is very low [46]. Nevertheless, the formation of cracks is possible if there is a combined effect of mechanical stress concentration and H dissociation. H can penetrate into the metal lattice easier if there is a tension field, even if only microscopically [47].

- Material factors: HE depends on the crystal structure, the presence of second phases, H solubility and diffusion, hydride formation, among others. Material strength is one of the most important parameters regarding HE susceptibility [48]. As strength increases, materials become harder, less ductile, less tough and more susceptible to HE. For example, when considering steel microstructures, martensitic structures are considerably more susceptible than ferrite, austenite or bainitic steels.

Moreover, coarse-grained materials are more susceptible to embrittlement than fine ones. Additionally, impurities and non-metallic inclusions, result from uncontrolled heat treatments, can dramatically increase the HE susceptibility [49].

- Environmental factors: There is a dependence on the H source, whether an electrolyte, gas, aerosol, plasma, etc.; on the H fugacity, since it has been documented that high H fugacities promote measurable effects on mechanical properties; on whether external and/or internal H is present; among others. Thereby, internal H refers to test specimens that are pre-charged with H prior to testing and external H refers to specimens that are tested in H atmospheres.

There are several manifestation of HE and depending on the damage produced and the source of H, HE can be classified as "internal hydrogen embrittlement" (IHE) or as "hydrogen environment embrittlement" (HEE) [25].

IHE involves concentration of pre-existing H in regions of high hydrostatic stress, resulting in cracking under applied stresses below yield stress. Materials inherently retain a small amount of residual H as they are produced. Vacuum degassing techniques have improved to the extent where H concentrations are roughly in the order of 1 ppm. Internal H can also be introduced during the manufacturing processes. For example, steels are typically electroplated with Zn, which acts as sacrificial metal, and, since the process is not 100% efficient, H can be absorbed during the coating deposition [28]. On the other hand, HEE involves subcritical cracking of materials under sustained loads in H atmospheres. Thereby, H may originate from gaseous H or be generated from a corrosion reaction [25].

Materials have been shown to behave differently in HEE and IHE conditions. A previous work by Symons [50] comparing IHE to HEE proposed many differences and similarities between them. The difference between both could be related to a changes in the characteristic fracture distance (which is a microstructure-related parameter) and in the embrittlement mechanism. The mentioned work on the alloy X-750 showed that, while both H-induced decohesion and H-enhanced plasticity might be responsible for IHE, HEE appeared to be caused by H-induced decohesion.

Once H is loaded into the material, solute H occupies and diffuses between interstitial lattice sites in metals, and can be trapped at other sites. The trapping sites include some solute atoms, free surfaces and sites between the first few atomic layers beneath surfaces, mono-vacancies and vacancy clusters, dislocation cores and strain fields, grain boundaries, precipitate/matrix interfaces and strain fields around precipitates, inclusion/matrix interfaces, and voids and internal cracks. These traps have different trapping strengths and are characterized by their nature, i.e., reversible or irreversible, saturable or unsaturable [51]. For example, a dislocation core is a saturable, reversible trap; while voids and cracks are unsaturable, reversible traps. An example of irreversible traps are precipitate/matrix interfaces or carbide particles, among others.

Regarding H diffusion, diffusivity in pure metals at ambient temperatures is primarily determined by the crystal structure, with H-diffusion coefficients around four to five orders of magnitude higher for b.c.c. metals compared with face-centred-cubic (f.c.c.) and hexagonal close-packed (h.c.p.) metals [52]. This can be explained considering the distance between nearest-neighbor interstitial sites, which is smaller in b.c.c. lattices. Larger distances are correlated with lower diffusivities [53]. In alloys with complex microstructures, effective diffusion values at ambient temperatures decrease with increasing number and strength of traps. Also, H diffusivity increases with increasing temperature, since H can be released from deeper traps and diffuse to surfaces more rapidly. Furthermore, H can be transported faster by mobile dislocations than by lattice diffusion when it is present at dislocation cores or as atmospheres around dislocations [25].

2.3. Proposed hydrogen embrittlement mechanisms

There are several mechanisms proposed for HE and the most commonly cited mechanisms include [54], [55]:

- H pressure buildup mechanism, in which the pressure of H bubbles provides the stress for the formation and propagation of a crack.
- H-induced reduction of surface energy, in which H is adsorbed at the crack tip or surface imperfections, reducing the surface energy for crack propagation.
- H-induced decohesion, in which H reduces of the cohesive strength of the lattice.
- H accumulation at precipitates and second-phase particles, which can lead to dislocation generation or crack nucleation and growth.
- Formation and fracture of a brittle hydride.
- H-induced reduction in the stacking-fault energy.
- H-enhanced localized plasticity, in which H promotes the dislocation mobility.
- H-enhanced strain-induced vacancies.
- Adsorption-induced dislocation emission.

It is not only thought that one of these mechanisms predominates, but it also believed that more than one model work in parallel to each other leading to HE. The operative mechanism/s depend on the material, the H charging conditions and the loading state. From these candidate mechanisms, some have evolved over the years and have been supported by experimental observations and strong personal views:

2.3.1. H-induced decohesion (HEDE)

HEDE was first proposed by Geberich and Oriani [56], [57]. In this mechanism, the atomic bonding at the crack tip is weakened by the presence of H in solid solution, as shown in Fig. 5. Direct evidence of this mechanism has not been shown until now and is supported primarily by observations in some non-hydride forming systems, where there is no significant local deformation, by theoretical and thermodynamics calculations.

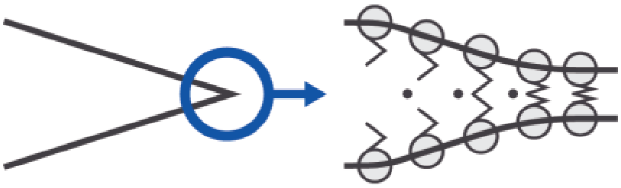

Figure 5. Scheme of HEDE mechanism

The decohesion theory [57] for H-induced crack propagation postulates that the chemical potential of dissolved H is lowered in some regions at crack fronts and larger H concentrations than that of equilibrium are reached. As a consequence, the large H accumulation lowers the maximum resistive cohesive force between atoms. The decohesion hypothesis states that weakening of interatomic bonds occur in preference to slip.

Direct experimental evidence of the HEDE model is difficult to obtain, since there are hardly any techniques for directly observing events on the atomic scale at crack tips. The model is mainly supported by the analysis of the fractured morphological features obtained from macroscopic tests and by models with several simplifications, which remain to be validated. [58] Moreover, it lacks supporting evidence from direct experimental observations.

2.3.2. H-enhanced localized plasticity (HELP)

This mechanism is based on the increased dislocation mobility and the failure is produced by plastic deformation mechanisms. It was first suggested by Beachem [59], who based on observations of tear ridges and dimples on fracture surfaces of H embrittled steels suggested that the effect of H was to “unlock” rather than “lock” dislocations. He proposed that H allowed dislocations to multiply or move at reduced stresses.

Later on, the HELP mechanism was presented by several authors [60]–[63], based on observations that in certain range of temperatures and strain rates, the presence of H in solid solution decreased the barrier to dislocation motion, thereby increasing the amount of deformation that occured in a localized region adjacent to the fracture surface. The fracture process is believed to be a highly localized plastic failure rather than an embrittlement. Robertson et al. [61] reported that by adding H to an environmental cell, the dislocation mobility of stresses specimens increased and decreased by removing H. They observed this behaviour for edge, screw and mixed dislocations and for isolated dislocations, in addition to dislocation tangles in b.c.c., f.c.c. and h.c.p. metals which exhibited HE. Furthermore, increased dislocation velocity was also observed for Frank-Read sources and dislocations terminating at surfaces.

It was proposed [62] that H forms an atmosphere around dislocations and other elastic stress centres. H is believed to reduce the interaction energy between dislocations and obstacles, as well as among themselves, so they can move at lower levels of applied stress. Direct experimental evidence was provided by deformation experiments inside a transmission electron microscope (TEM) [61], [63], [64]. A scheme of the model is shown in Fig. 6.

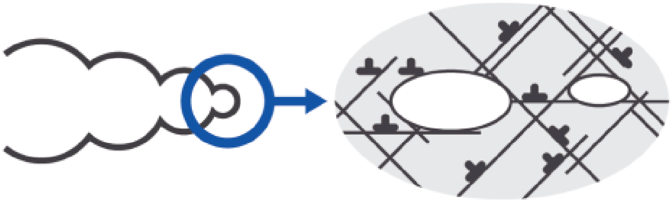

Figure 6. Scheme of HELP mechanism

The HELP model is mainly based on in situ observations of the dislocations in an environmental TEM. As a descriptive mechanism, HELP has found widespread support; however, there are still disagreeing voices. For example, it is found not to be realistic in b.c.c. metals, since a large amount of

H concentration would be required to reach the softening effect that HELP proposes as a result of the reduction of dislocation interactions due to H shielding effect [65]. Furthermore, it has been argued that dissociation and ionization of the H_2 molecule be the electron beam increased the fugacity by several orders of magnitude [66].

2.3.3. Adsorption-induced dislocation emission (AIDE)

Based on similarities between H-assisted cracking and adsorption-induced liquid-metal embrittlement observed in many materials, Lynch proposed the AIDE mechanism [35], [67]–[69], shown if Fig. 7. It claims that H weakens interatomic bonds, promoting dislocation emission from crack tips. As a result, the greater proportion of dislocation activity leads to faster crack growth. In this model, the term “dislocation emission” involves not only nucleation, but also their subsequent movement away from the crack tip. The nucleation stage involves the formation of a dislocation core and surface step by shearing of atoms over several atomic distances. Thus, adsorbed H facilitates this process by weakening of interatomic bonds.

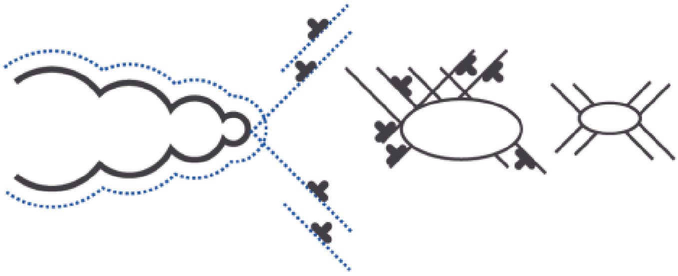

Figure 7. Scheme of AIDE mechanism

In the AIDE model, crack growth involves not only dislocation emission from crack tips, but also nucleation and growth of microvoids ahead of a crack tip. This can also occur at other sites in the plastic zone ahead of cracks, such as second-phase particles and slip-band intersections, since the stresses required for dislocation emission are rather high. Void formation contributes to crack growth and resharpening of crack tips.

Comparing the schemes of the proposed mechanisms, while in the HEDE mechanism the crack tip is sharp, in HELP and AIDE there is a blunting of the crack. The HELP mechanism proposes that there is a small localization of deformation, which is shown in the figure with color, result of high hydrostatic stresses and the concentration of H. AIDE, on the other hand, can be considered as a combination of HEDE and HELP and even that in this case there is no localization of deformation, the dislocation activity in front of the crack leads to small crack tip opening angles. In ductile crack growth, in comparison, only a small portion of the dislocations emanated from crack tip sources intersect the crack tip to produce crack advance. When H is present, on the other side, the coalescence of cracks with voids occur at lower strains and shallower dimples are produced [25].

2.4. State of the art

One of the major causes of the arguments of HE mechanisms is due to the difficulty of capturing the effect in the different time and length scales associated with the phenomenon. H diffusion is considered fast and can vary with different test temperatures and stress/strain rates. The interaction between H and metal atoms, defects and/or cracks require an analysis under atomic and/or mesoscopic length scale. There are several different methods to analyse the effect of H, and the experimental conditions (e.g. H charging conditions, geometry of the sample and structure stability) must be carefully controlled to justify if inconsistencies are found or to explain the origin of possible contradictions.

Since HE failures are time-dependent, the time component should also be incorporated in any experimental method to investigate H effect. HE testing can be performed by means of sustained load tests, which consists in applying a specific static load for a fixed period of time. Other analytical alternatives are slow strain rate (SSR) tests or the incremental step load test. In these tests, there is increase of the applied load until rupture of the sample and, therefore, the time component is incorporated in the test. When the loading rate is slow enough, the measurement of the HE threshold stress for a given material under H concentration is possible.

Fracture-mechanics parameters, such as threshold stress-intensity factors and crack velocities at high K-values for statically loaded specimens, are other common measures of susceptibility. Many researchers have worked on this topic over the past years. Kim et al. [70] developed an analytical model to investigate H effect on the K_c value and fracture toughness of steels. Song and Curtin [71] also develop a model to investigate the effect of H on a crack tip in Ni and created a mechanism map that predicts the transition from ductile to brittle fracture. Experimental work has also been performed by testing, for example, notched micro- beams with and without H [72]–[75]. By testing micro cantilevers, the effect of H on fracture toughness can be evaluated. Rogne et al. [72] showed the influence of H on the initiation of the fracture and plasticity of the crack tip in an iron aluminide intermetallic alloy.

The effect of H on materials can also be investigated microscopically regarding the fatigue crack growth behaviour [20], [76]–[78]. From the viewpoint of the H movement and the concentration of H at fatigue crack tips, the H content of materials, the H diffusion rate, the cyclic load frequency and the stress fields in the vicinity of crack tips must be considered for studying HE with this approach. Ogawa et al. [78] analyzed the influence of H on fatigue crack growth behavior of stainless steels. They investigated fatigue mechanisms, martensitic transformation and H content, and showed that martensitic transformation accelerated fatigue crack growth under H atmosphere.

Regarding H charging conditions, H can be delivered into specimens by several different ways, for example by cathodic charging [41], [45], by exposure to high-pressure H gas [79], via H plasma [80], [81], among others. Electrochemical charging is the most conventional charging method and has been used in combination with nanoindentation [82]–[85], with microcantilever bending tests [75] and with SSR tests [22], [43], [86]–[88]. Despite its ease of use, it has several disadvantages. For instance, under certain conditions, the charging can produce damage in the material by the charging itself and not due to H action. Therefore, plasma charging has received attention and is gaining popularity as a H source. Depover et al. [89] compared plasma with electrochemical charging on a dual phase steel and concluded that, even though the effect of electrochemical charging was more pronounced, both methodologies exhibited the same tendency.

HE studies can be made either with ex or in-situ charging. In the cases where in-situ studies are not possible, samples have to be pre-charged with H. Issues concerning the pre-charging approach are the outgassing of H when the sample is removed from the charging device (in particular in materials with high H diffusivity), structural degradation of the metal due to cathodic charging (in the case where H is charged by this method), and that the charging potentially introduces H only within the surface layer of the samples and the center remains uncharged. With in-situ H charging, on other hand, there is a continuous supply of H, which avoids the risk of outgassing. Moreover, in-situ H charging can be combined with in-situ observation [74], [80], [81], [90]–[92] to monitor deformation in order to focus not only on the analysis of post-mortem morphologies, but also to gain knowledge about the H-microstructure interaction.

Many in-situ experimental methods have been developed in the last years. One of the first in-situ approaches, already mentioned, was developed by Robertson, Birnbaum and Sofronis [62],

[90]. They performed small scale tests in an environmental TEM and their observations of the movement of dislocations under H atmosphere led to the proposal of the HELP mechanism. Nanoindentation combined with electrochemical charging has also become very popular for HE studies [41], [45], [82]–[84], [93], [94]. With this technique it is possible to analyze the effect of H on the hardness and Young's modulus, on the dislocation nucleation and perform multiple tests in a single grain. In this case there is no in-situ observation, but in-situ H charging while mechanical testing. Based on this, Kim et al. [92] developed a technique to perform both microstructural and mechanical analysis while H charging. This method is similar to the previous mentioned but, in this case, nanoindentation is performed inside a scanning electron microscope (SEM). Besides the analysis of mechanical properties with H charging, having in-situ observation allows, for example, the investigation of H effect at specific microstructural features. Furthermore, in combination with silver decoration, H distribution and diffusion paths can also be investigated.

Following the line of in-situ observation, micro-cantilever bending tests have been also applied inside an SEM to obtain a full observation of H effect on deformation processes [73], [75], [91]. In these cases, H charging was performed either by electrochemical charging or by atomic H, product from the reaction of the tested alloy and water. Another possible charging used recently in in-situ methods is with H-plasma [80], [81], [89], [95], [96]. With these methods, H was charged in-situ inside an SEM while performing a tensile test, allowing a high-resolution observation during the test. Comparing plasma and electrochemical charging, plasma charging has the advantage that the surface damage is minimized, providing reliable results, which are not influenced by the charging itself.

In conclusion, HE is a well-known phenomenon that affects a large number of high-performance materials. Nevertheless, until today, it is not clear which is the mechanism that predominates. In addition, although there is considerable evidence from some experiments, researchers do not agree on the fundamental mechanisms causing the embrittlement. The previously mentioned proposed models of H-cracking may occur conjointly in some cases, and depend on the material, its microstructure, the environment, the temperature, the applied strain-rate or stress-intensity factor, which can lead to difference in fracture modes. Furthermore, depending on the experimental approach, results can differ and be classified as one or another mechanism. For this reason, it is crucial to have experimental methodologies with well-defined parameters and reliable results.

3. Summary of the results

In this chapter, the most important results of the thesis will be presented, together with their discussion and impact. Fig. 8 shows a scheme of the papers done within this work. The first paper consists of the development of the method and a case study that shows its validity. The second paper deals with the application of the method to investigate the effect of a H in a fast diffusion material, showing that only observation during in-situ charging allows addressing H effects. Finally, the third paper reviews recently developed in-situ and in-operando methods that can be implemented and applied in many H-related technologies. These three papers are summarized in the next section.

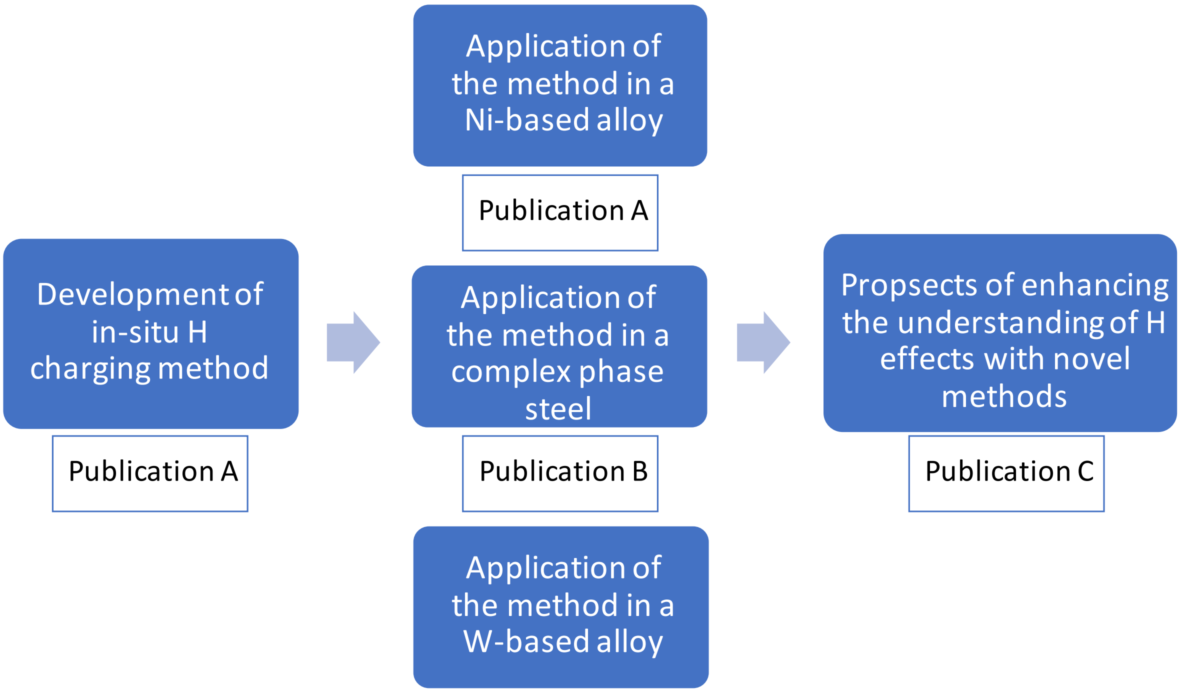

Figure 8. Scheme of investigated topics and publications done within this work

This section will be divided into the development of the methodology, the effect of H on a Ni-based alloy, a complex phase steel and a W-based alloy, and an overview of recently developed methodologies that can be employed in H-related technologies.

3.1. Development of in-situ plasma charging method

As aforementioned, the controversies in the results over the past years make it necessary to develop new methodologies with well-defined parameters, which can provide reliable results. With this aim, a novel in-situ method was developed to investigate H-material interactions. This methodology combines in-situ H charging, mechanical testing and observation, defining the three HE interaction parameters; mechanical, material and environmental, from Fig. 4.

Radio frequencies plasma discharges are commonly used for materials processing, such as thin film deposition, surface modification and etching. Therefore, this configuration was chosen for H charging. Fig. 9 depicts a scheme of a radio frequency plasma discharge. It consists in two electrodes confined in a vessel, in which H gas is supplied creating, as a result, H plasma.

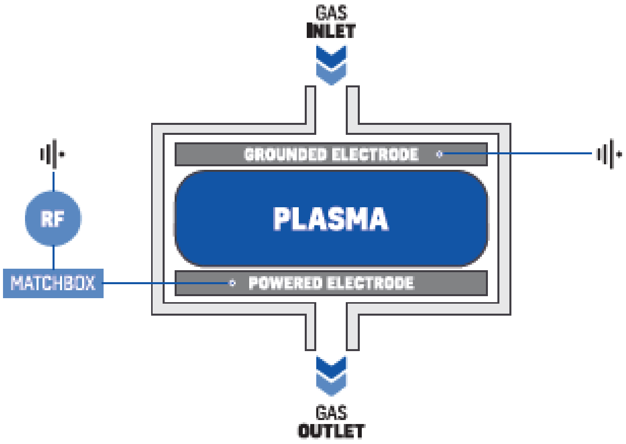

Figure 9. Scheme of a radio-frequency plasma discharge

Fig. 10a shows a scheme of the miniaturized plasma cell in the SEM and 10b a cross section of the tensile sample with the H-charging and observation directions [80]. The miniaturized plasma cell consists in a stainless-steel cup, which is powered by a high-frequency power supply and has a 2 mm opening at the top. A metallic tensile sample, which acts as counter electrode is, is placed on the top of the cup and is, in this way, charged from the bottom. Deuterium was chosen as the working gas so that H content can be determined more precisely by thermal desorption or nuclear reaction analysis.

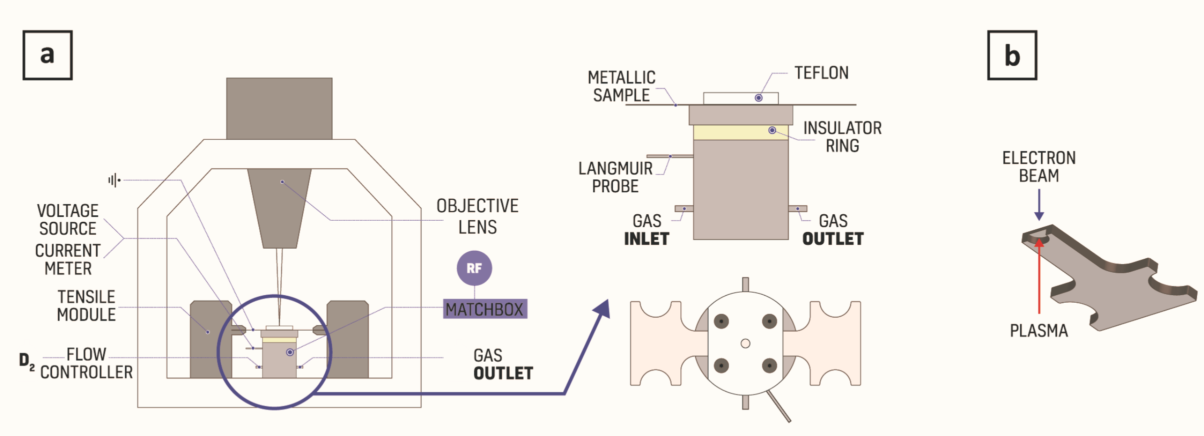

Figure 10. (a) Scheme of miniaturized plasma cell inside the SEM and (b) cross section of tensile sample with H-charging and observation directions

In order to obtain a faster H-diffusion through the thickness of the sample, the center area has a thickness reduction. The charging is conducted inside an SEM equipped with a tensile module in order to monitor the deformation in the center charged area of the samples during H-charging. Since the charging is conducted from the bottom, the top observed surface is contamination-free. A Teflon disk with an aperture in the center and an indium wire gasket is used to seal the cell and allows the displacement of the sample due to its low friction coefficient.

As mentioned, the designed sample geometry deviated from standardized geometries. Therefore, a three-dimensional mechanical finite element simulation was performed to investigate stresses distribution through the thickness of the samples. The results showed that the hydrostatics stress, maximum principal stress and Von Mises stress were homogenous, proving that the geometry design did not have an influence on the results.

Plasma parameters were investigated with a first protype with Langmuir probe measurements. This method consists in inserting a tungsten wire into the plasma and measure the current (I) drained by varying the applied bias voltage (U). With these values, different I-U curves can be obtained for different gas flow rates, and with their analysis, the electron density, electron temperature and ion flux can be calculated, as detailed in reference [80]

With the ion flux φ_I, an analytical model, which is based on ion-driven permeation in plasma charging, can be used to calculate H concentration. Fig. 11 shows the concentration profile of a sample charged with plasma from one side and subjected to vacuum on the other side.

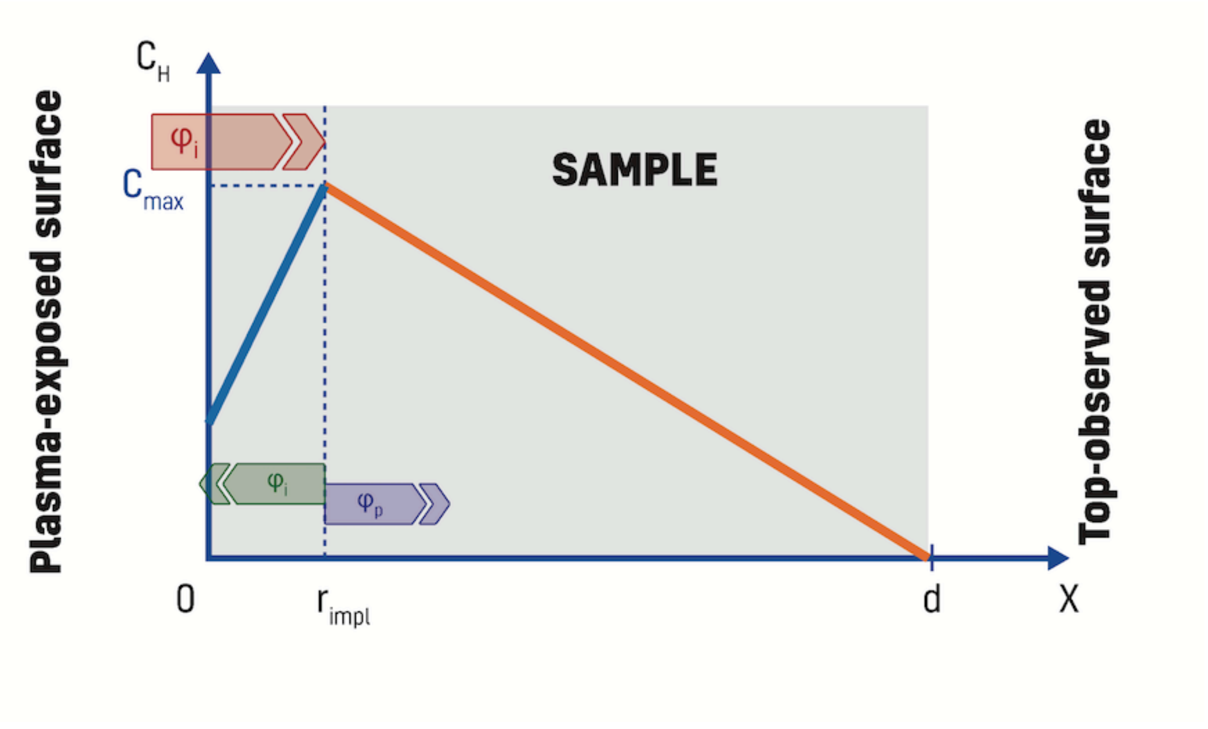

Figure 11. H concentration profile in a plasma-charged sample

The concentration increases linearly until the mean implantation depth r_{impl} and from this point decreases linearly until 0 at the top of the sample. With a Monte-Carlo program [97], r_{impl} (where the maximum concentration is) and the implanted and reflected coefficients can be calculated. There are three possible permeation processes, depending on the relative rate of recombination and diffusion on both sides of the sample. One is diffusion-limited on both sides and the H concentration can be calculated with Equation 1. The other two cases are recombination-limited on one side and diffusion-limited on the other side, and recombination-limited in both sides. For these two cases, Equation 2 can be used.

$$C_{max} = \frac{r_{impl} * (1-R) * \varphi_i}{\rho * D_H} \quad (1)$$

$$C_{max} = \sqrt{\frac{\varnothing_i}{k_f}} \quad (2)$$

Here C_{max} is the maximum lattice concentration, r_{impl} the mean implatantion depth, R the reflection coefficient, φ_I the ion flux, ρ the density of the material, D_H the H diffusion coefficient and k_f the recombination coefficient.

With the values calculated with the Monte-Carlo program, the density and diffusion coefficient of H of the selected material, and the recombination coefficient, which can be calculated from different sources [98]–[100], the maximum concentration of H in the material can be calculated for the three types of permeation cases.

3.2. Effect of hydrogen on a Ni-based alloy

To validate the in-situ method, the first material selected was a Ni-based alloy (Alloy 718) in the solution annealed condition. The H susceptibility of this material has already been widely studied and reported [21], [37], [101]–[103], making the Alloy 718 a perfect model material. Fig. 12 shows the microstructure of the material with an inverse pole figure, showing the presence of twin boundaries. The grain size is around 100 µm.

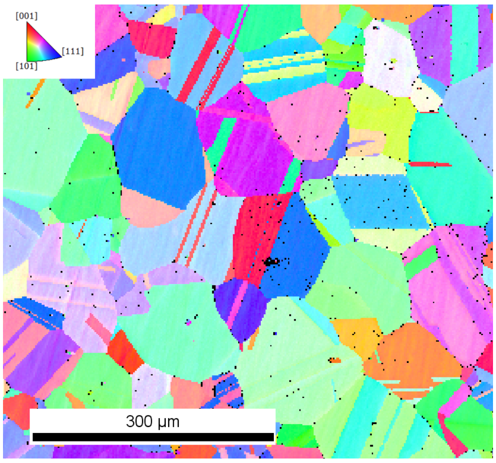

Figure 12. Inverse pole figure in the normal direction of Alloy 718

Two batches were used to investigate the effect of pre-charging time and pre-straining. For the first case, samples were pre-charged with different time durations and also charged while testing, while in the second case the samples were first pre-strained, below and beyond yield point, and then charged with H before continuing the tensile test. For all the cases a SSR test was performed. This testing technique was chosen since usually the embrittlement effect is enhanced with slower strain rates as H has more time to diffuse to areas with higher stress concentrations.

Due to the non-standard sample geometry configuration, load-elongation instead of stress-strain were analyzed. In the first set of experiments, all the curves converged to approximately the same maximum load and the elongation was reduced in all charged specimens. Moreover, with the in-situ images it was possible to monitor crack propagation. As expected, with increasing H charging time, crack propagation rate increased. The fracture surfaces were also investigated after the tests and they changed from ductile microvoid coalescence failure, in the uncharged case, to brittle intergranular and “quasi cleavage” failure, in accordance with previous reports in literature [22], [43], [104], [105].

Regarding H concentration, for Ni-based materials, since H diffusivity is low, the permeation is diffusion-limited on both sides of the sample. Using the analytical model described in the previous section and Equation 1, H concentration was calculated. The average solute concentration was between 2 and 2.5 wppm.

Fig. 13a depicts the load-elongation curves and 13b the normalized crack length over time of the pre-straining experiments. On the one hand, in the sample pre-strained before yield, the effect of H was similar to the previous cases exhibiting a reduction in elongation and an increase in the crack propagation rate. On other hand, the sample pre-strained beyond yield was somehow less sensitive to HE. In this case, the crack propagation rate was decreased, and the fracture surface consisted mostly of dimples, typical of ductile fracture. A possible explanation is that there could have been strain hardening in the uncharged sides of the sample, lowering the crack propagation rate.

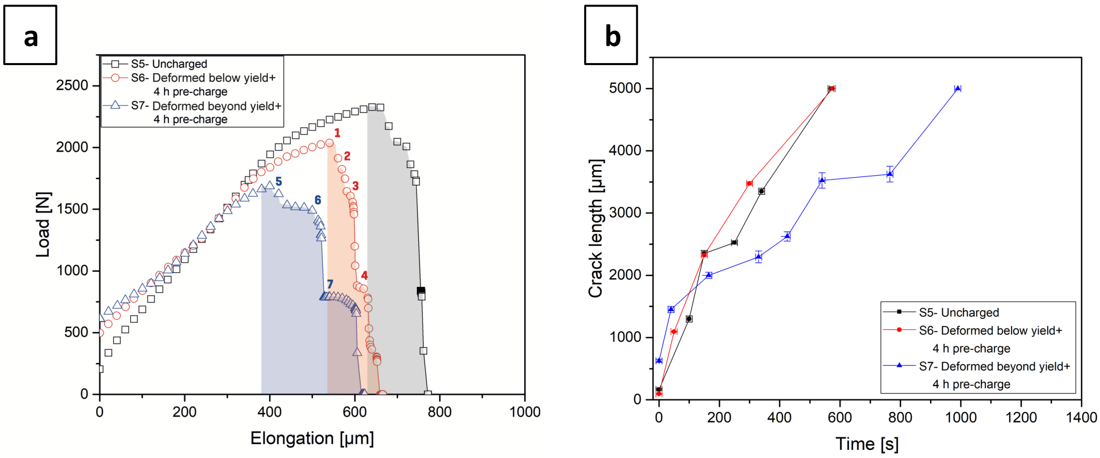

Figure 13. (a) Load-elongation curves and (b) crack propagation rates of pre-strained and H-charged Alloy 718 samples

3.3. Effect of hydrogen on a complex phase steel

As already mentioned, the combination of high-strength and low-weight, makes the advanced high-strength steels (AHSS) excellent candidates for the automotive industry [12], [106]. They are also used in chemical and refinery industries, in power plants, marine structures, gas transportation pipelines and as aircraft components. Despite their excellent mechanical properties, they are susceptible to HE and can lose their ductility through H absorption. Even though AHSS are usually electroplated, if the sacrificial coating corrodes in service, the exposed areas act as cathodic sites, resulting in H absorption into the material. Complex phase (CP) steel belongs to the group of AHSS and its main microstructural phases are martensite, tempered martensite, bainite with a small content of retained austenite. Fig. 10 shows the microstructure of the material [96]. The grain size is approximately 3 µm.

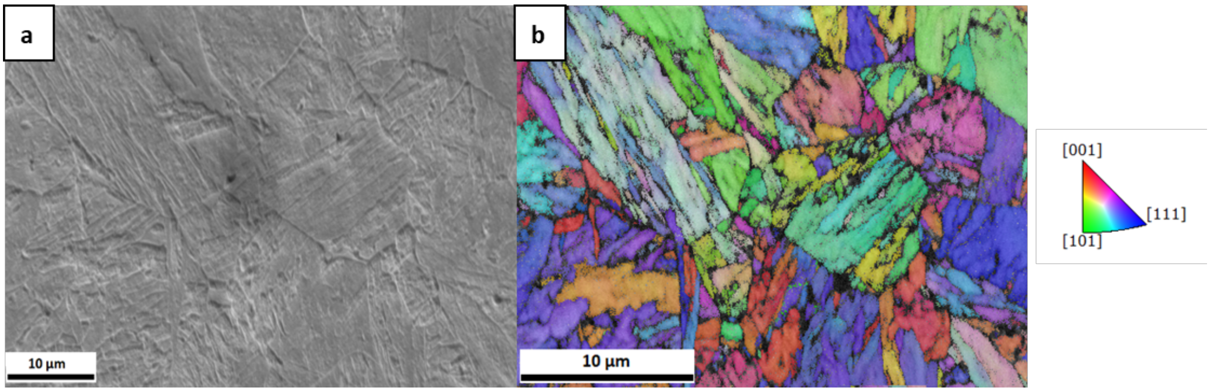

Figure 14. (a) Secondary electron image. (b) Inverse pole figure in the normal direction of CP steel

First of all, the strain rate sensitivity of the material was analyzed. This was done by analyzing stress-strain curves resulting from different strain rates of tensile tests of uncharged specimens and by nanoindentation strain-rate jump tests. Moreover, nanoindentation was also used to determine the modulus and hardness of the material.

The strain rate sensitivity index was calculated from the slope of the plot $\ln\sigma$ vs. $\ln\varepsilon$ giving a value of almost 0, indicating that the material exhibits no significant strain rate sensitivity in the investigated regime. This was further verified with the nanoindentation strain-rate jump tests results. This is important to note as the results will depend only on H effects and not on the effect of different loading conditions.

The effect of H was studied with the in-situ plasma charging method described in the first section [80], which combines in-situ H-charging, mechanical testing and high-resolution observation in an

SEM. The influences of different H charging conditions (different concentrations, charging and discharging and pre-charging times) were examined.

Regarding the effect of pre-charging time, tests were performed with 3 and 6 h of pre-charge, both followed by continuous charge during the tensile test, and compared with an uncharged specimen. From the analysis of the load-elongation curves, it was observed that the initial part of the curve was unaffected but with increasing H charging time, the elongation to failure decreased and there was a more pronounced load drop when cracks where initiated, as shown in Fig. 11 [96].

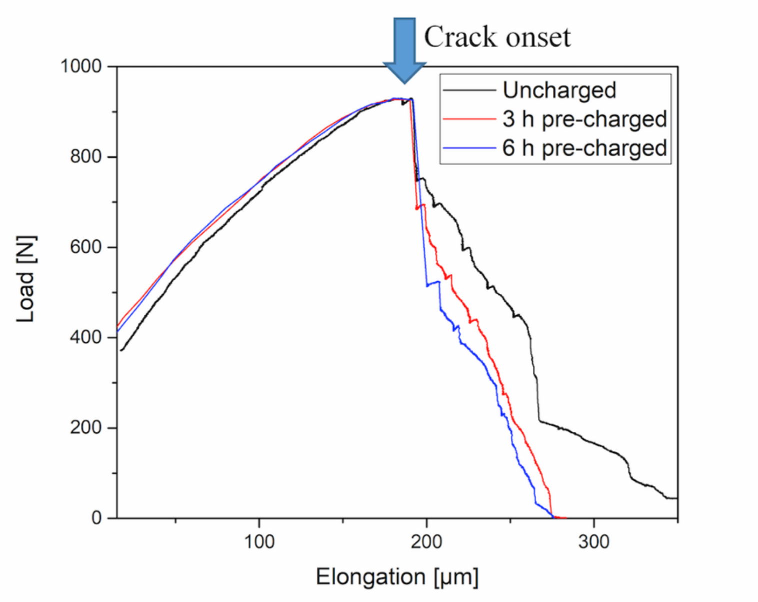

Figure 15. Load-elongation curves of uncharged and charged CP specimens

As in the previous section, crack propagation rate was calculated from the in-situ images. It can be seen in Fig. 12 [96] that with increasing charging time, final fracture was 1.27 and 1.45 times faster in the 3 and 6 h pre-charged samples than the uncharged one.

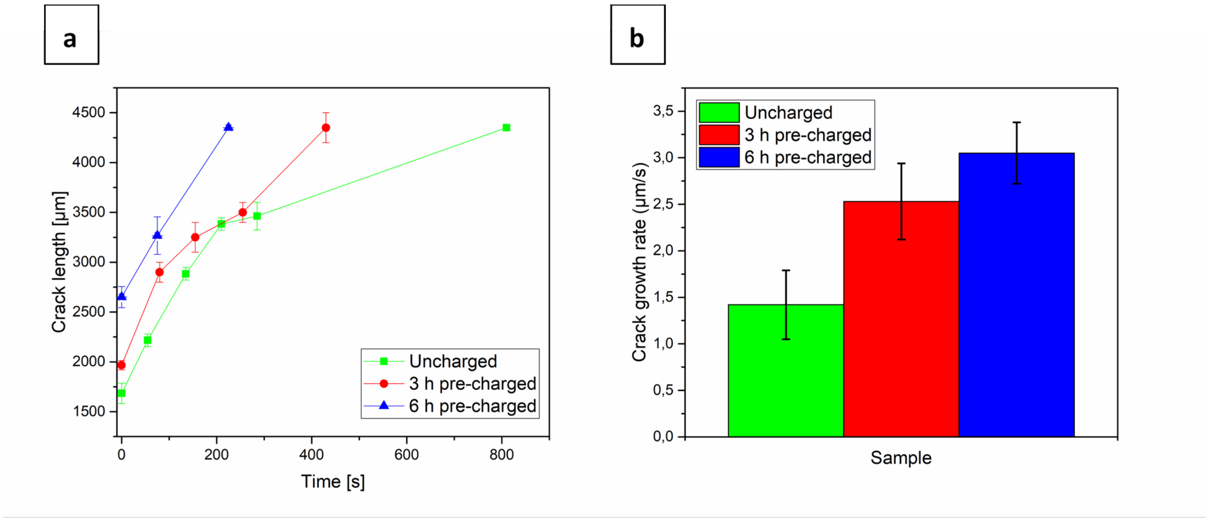

Figure 16. (a) Normalized crack evolution. (b) Crack growth rate

EBSD analysis was also performed on these samples. From misorientation analysis, it was seen that in the sample with longer charging time, there was a localized plastic deformation in areas next to secondary cracks, meaning that H could promote a greater dislocation activity in some localized regions.

With testing a charged and discharged sample, the reversibility of HE was proved. There was no effect in the stress-strain characteristics and the fracture surface exhibited a typical ductile microvoid coalescence failure. This also verifies that HE is produces by diffusible H, which can diffuse out of the specimens at room temperature. Considering that in this material H is trapped mainly at dislocations and martensitic lath boundaries, which are not deep traps, all the H can effuse during discharging.

From the SEM fracture surface images, the dimple size of all samples of each case study was estimated. It was found that all charged samples had smaller dimple size than the uncharged ones. A reduction in the dimple size can be attributed to the effect of H on fracture behavior, representing an increase in dimple nucleation.

For the H concentration estimation, the analytical model from the first section was implemented, in this case the material follows the behavior from Equation 2, and the concentration was also calculated using a simulated diffusion model. The recombination coefficient k_f was taken from three different sources, Shu et al. [98], Zhou et al. [99] and Baskes [100]. The analytical model gave a lattice concentration in the order of 10^{-5}-10^{-4} wppm. The simulation, on the other hand, takes into account not also the H stored in interstitial lattice positions, but also H in traps.

Fig. 13 depicts the simulated H concentration through the thickness of the sample [96]. It can be seen that the lattice concentration is in the same range than the one calculated with the simple model. Nevertheless, when trapping is included, the concentration is around a factor of 350 higher. However, the maximum concentration is still rather low and it has been demonstrated that a H concentration above 2 wppm leads to a pronounced HE [107]. It is also shown that there is a H concentration gradient with the lowest value at the top observed surface. However, an advantage is that after approximately only 500 s, a steady state concentration is reached.

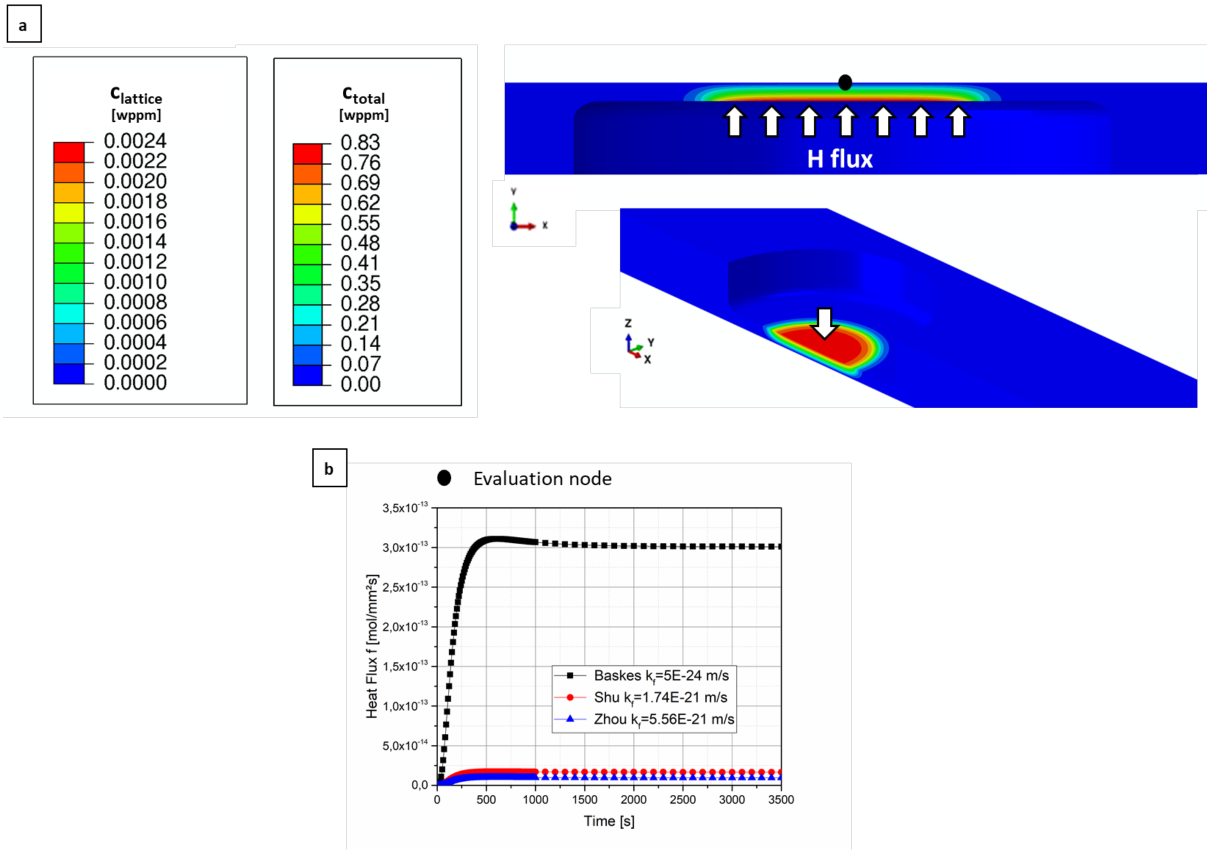

Figure 17. (a) H concentration distribution through the thickness of the samples, the arrows indicate H charging direction (b) H flux over time in the evaluation node marked on the top surface

Even though the total H concentration was low, slight modifications in fracture characteristics were observed and there are some alternatives to generally increase the concentration in the microstructure, such as impermeable nm thick coatings, transparent to the electron beam, reducing the sample's temperature, among others. Comparing these results with the H absorbed in specific applications, for example during the body in white painting process, where steels absorb approximately 0.4 wppm of H [88], it can be concluded that CP steel is a suitable material for that application.

In comparison with more conventional charging methods, where having in-situ observation can be very challenging, this methodology allows not only direct observation, but it is also combined with in-situ H charging. For fast diffusion materials, such as the studied CP steel, this is the only way to address H effects.

3.4. Effect of hydrogen on a tungsten-based alloy

The tungsten heavy alloy is a two-phase composite consisting of W grains in a matrix of Ni-Fe. The so called HPM 1850 consists of 97 wt.% W, 2 wt.% Ni and 1 wt.% Fe and is fabricated by liquid phase sintering. Due to its unique combination of strength, density, ductility, machinability and corrosion resistance, it is a potential material for divertor target in fusion devices [108], [109]. Despite its corrosion resistance, it has been shown that the alloy can be embrittled by H [16]. Fig. 14 shows the microstructure of the material. The grain size is around 56 µm.

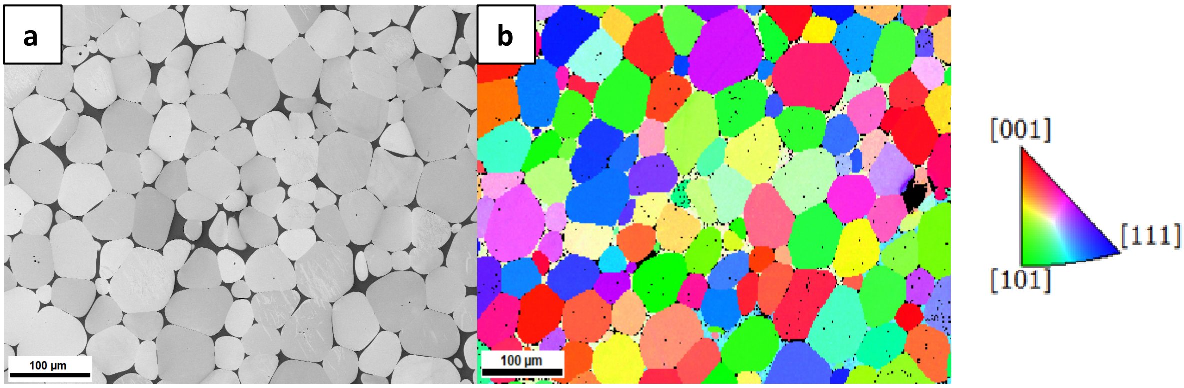

Figure 18. (a) Backscattered electron image and (b) Inverse pole figure in the normal direction of HPM 1850

In order to investigate H effects on this material, the in-situ method was applied, and a sample was pre-charged followed by continuous charging while testing and compared with an uncharged specimen. The maximum H lattice concentration was also calculated with the simple analytical model, giving a maximum concentration of around 2.34 wppm.

Fig. 15 depicts the stress-strain curves of both samples. While the elongation to failure of the uncharged specimen was around 10.5%, in the presence of H this was drastically reduced to 2%.

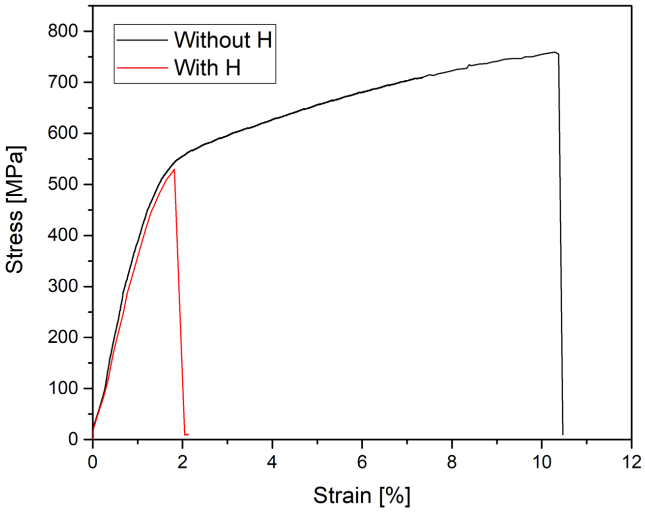

Figure 19. Stress-strain curves of uncharged and charged samples of HPM 1850

The fracture surfaces of the specimens were analyzed after the tests and are shown in Fig. 16. Comparing both images, there is not a clear difference between them. In both cases they are composed of brittle fractured W grains with dimples in-between, which correspond to the ductile matrix. Anyways, H does not always modify the fracture surface and since in the uncharged specimen there is already a high amount of brittle fracture, it is difficult to distinguish whether or not this is altered.

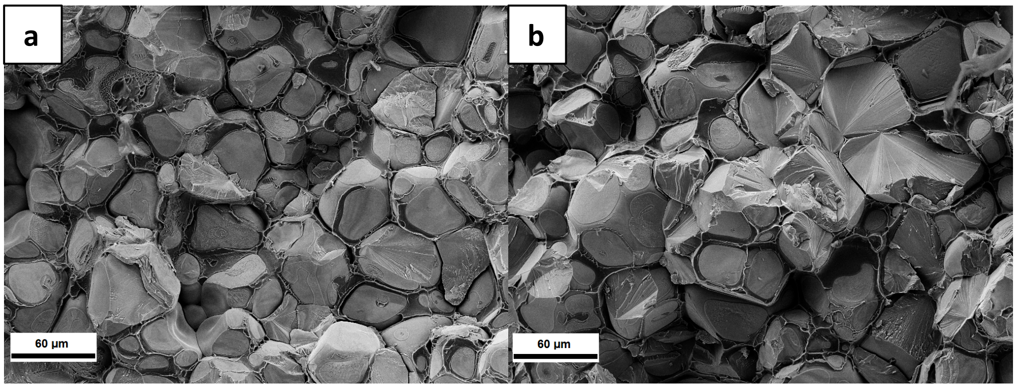

Figure 20. Fracture surfaces of (a) uncharged and (b) charged HPM 1850 samples

To gain a better understanding of H effect, the crack propagation path was also analyzed, and the amount of transgranular/intergranular failed grains calculated. It was observed that in the presence of H, the crack path changed from mostly transgranular to intergranular failure. These images are shown in Fig. 17.

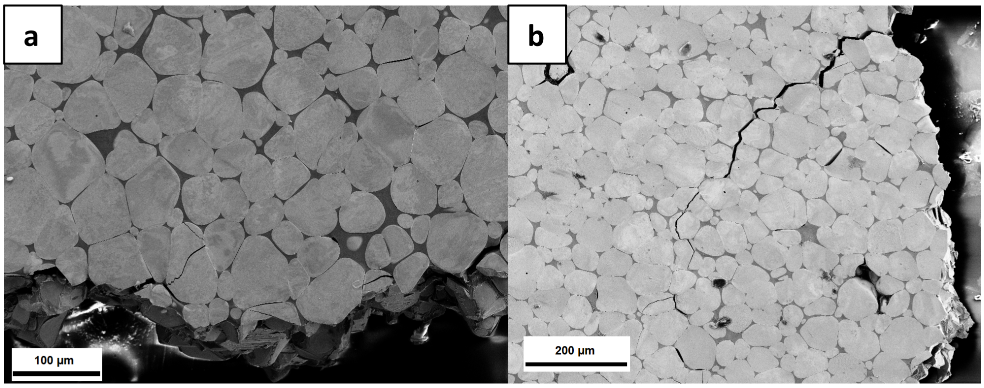

Figure 21. Crack propagation path of (a) uncharged and (b) charged HPM 1850 specimens

3.5. Prospects of understanding hydrogen effect on material with novel in-situ and in-operando methods

Recently developed in-situ and in-operando H charging methods were reviewed. They can be potentially implemented to study H-material interactions in a wide range of materials used in different H-related applications. Fig. 18 depicts a scheme of the materials typically used in different energy sources applications, which have to perform under H environment [110]. These energy sources are subsea oil and gas, nuclear fusion and fuel cells. Each of them has different material properties requirements and for all of these materials, the different in-situ methods can be applied to investigate mechanical properties, H-absorption characteristics and HE susceptibility.

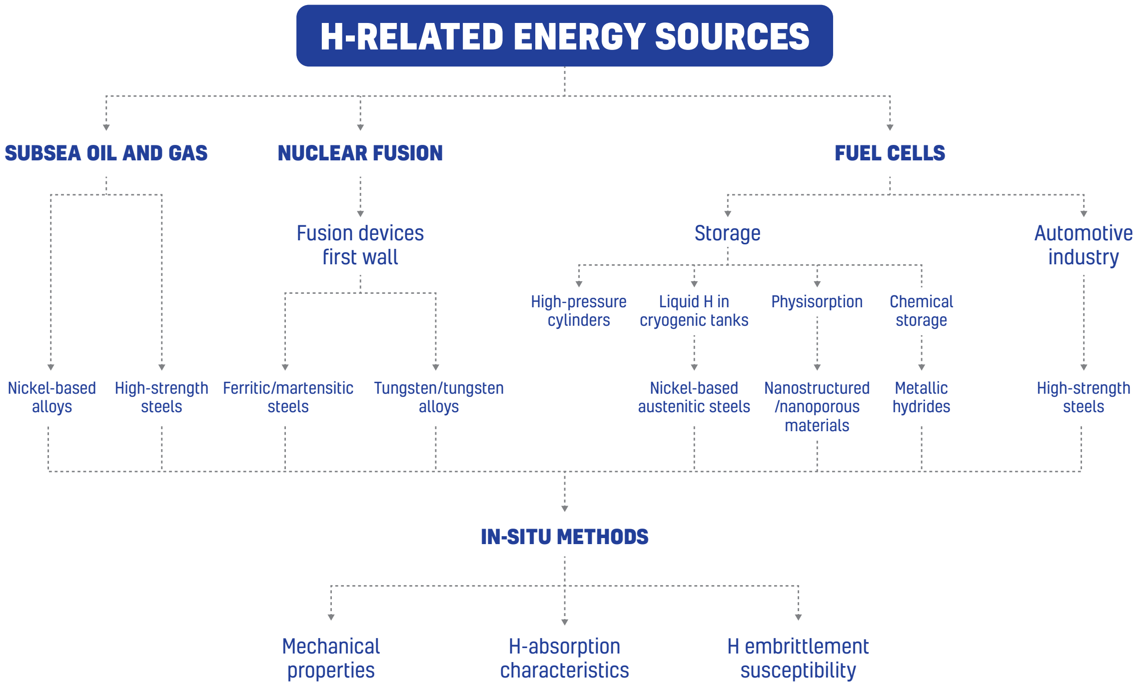

Figure 22. Applicability of in-situ methods to materials used in H-related applications

Fig. 19 depicts some the in-situ techniques. Fig. 19a and b consist of in-situ electrochemical charging with nanoindentation testing [82], [83]. This technique allows the possibility to perform multiple tests within a single grain and even though the volume of deformation is small, it is large enough to activate multiple slip systems under the indenter. With nanoindentation it is also possible to evaluate the effect of H on the hardness and Young's modulus of materials. Even though these approaches combine in-situ H charging and mechanical testing, having in-situ observation can be very challenging. The technique from Fig. 19c was developed to perform both microstructural and mechanical analysis while electrochemical H charging [92]. Fig. 19d depicts in-situ micro-cantilever bending tests with nanoindentation in an ESEM [73], [91]. This method also allows in-situ H charging, mechanical testing and observation but it has the disadvantage that it is only applicable to materials that produce atomic H from the reaction with water vapor. Fig. 19e and f show two methods that use low pressure H plasma as the charging source. In the first method, a plasma cleaner is connected to an ESEM chamber equipped with a tensile module [81]. In-situ imaging is, nevertheless, not possible while H-charging due to high H flammability. On the other hand, in the technique depicted in Fig. 19f, H-plasma is ignited through a radio frequency discharge and in-situ imaging is possible in this case while charging and tensile testing.

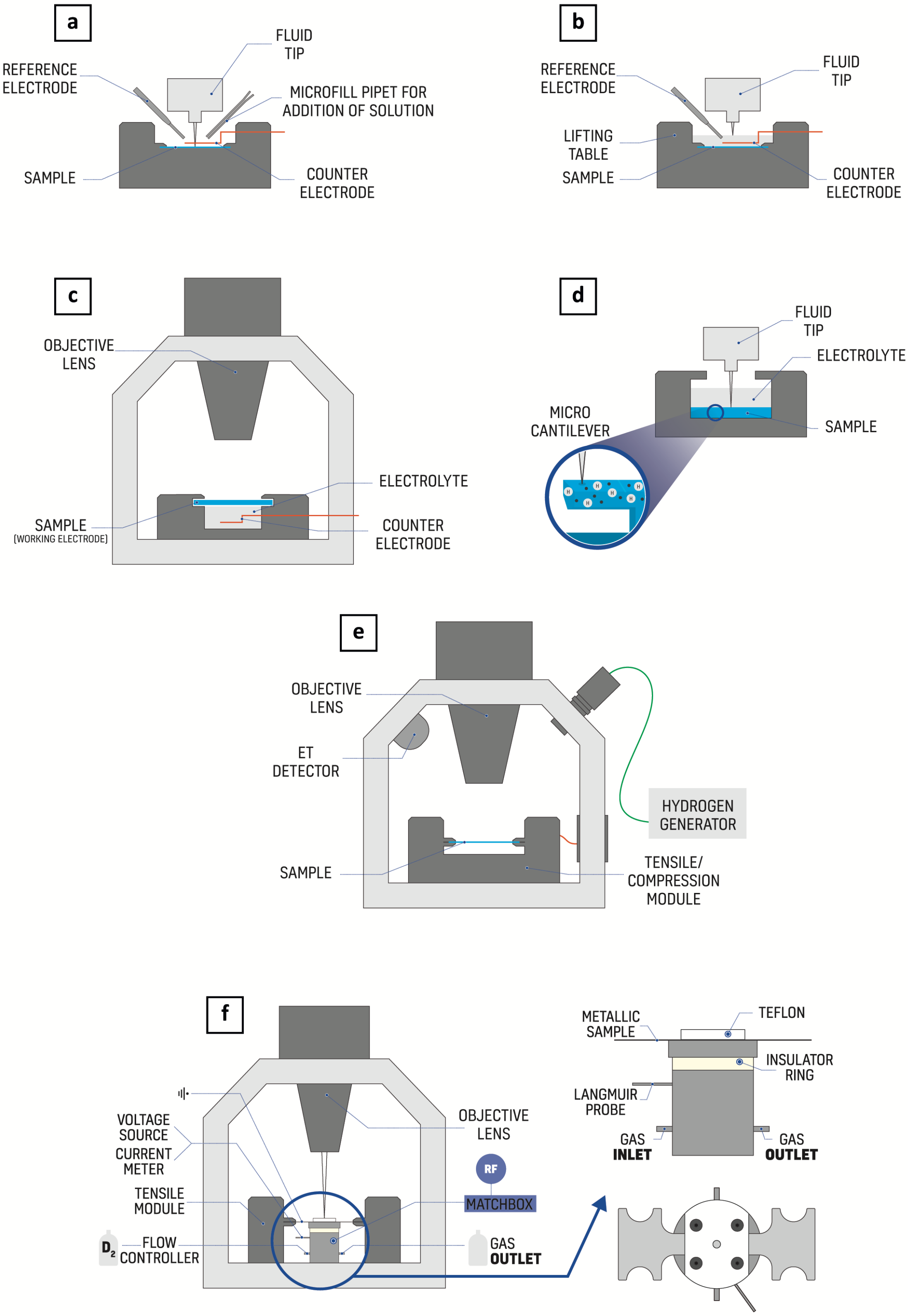

Figure 23. Schemes on in-situ H methods. (a) Nanoindentation combined with electrochemical charging. (b) Modified version of electrochemical nanoindentation test. (c) Electrochemical nanoindentation inside an

SEM. (d) Microcantilever bending test inside an ESEM. (e) Tensile test combined with H-plasma inside an ESEM. (f) Tensile test with a miniaturized plasma cell inside an SEM

All of the previous mentioned methods can be applied to investigate H effect on materials used in subsea oil and gas applications, in nuclear fusion and in fuel cell technology (including storage and the automotive industry), as shown in Fig. 18.

Regarding subsea oil and gas, Ni-based alloys and high-strength steels are the most used materials. They have to face high temperatures and pressures combined with corrosive environments. Even though these materials have corrosion resistance, they are susceptible to HE [22], [43], [104], [111], [112]. The described methods should be used to address H effects on the microstructure and modify and improve the alloys accordingly.

As nuclear fusion concerns, W and W alloys are the candidate materials for the first wall of fusion devices. As plasma facing materials, they have to withstand extreme heat and radiation damage [14]. To investigate the suitability of this alloys for this application, the methods with plasma-charging from references [80], [81] in particular, can be used to simulate close to real conditions.

For fuel cell technology, H storage represents one of the main technological challenges. The chemical composition, structure and thermodynamic and kinetic properties of the selected materials have to be investigated and improved to maximize the storage efficiency. For storage of liquid H in cryogenic tanks, Ni-based austenitic steels are good candidates for structural materials. Nevertheless, they can be susceptible to HE, specially if α'-martensite is formed during deformation in metastable alloys [18], [76], [113], [114]. They mentioned methods can be used to examinate H effect on the deformation processes, which cannot be investigated with post-mortem analysis. For chemical storage, metallic hydrides are the material of choice. The in-situ and in-operando methods can give information about H-absorption characteristics and hydride formation and their relationship with different microstructural features.

Fuel cell technology is currently being implemented in the automotive industry and, therefore, the effect of H on used materials needs to be addressed. High-strength steels are excellent candidates for this application but they are sensitive to HE and can lose their properties in the presence of H [27]. HE susceptibility on high-strength steels is mainly studied with ex-situ H-charging [17], [39], [86], [88] with the risk of H outgassing, especially in ferritic grades with high H diffusivity. This can lead to an alteration of the results. For these materials, only in-situ approaches can be used to investigate the effect of H.

As described, each application has different requirements and function under different conditions. The described techniques are essential to understand the effect of H on the materials that perform under H atmospheres. Moreover, small scale testing offers a wide range of possibilities to study deformation mechanisms and valuable information can be obtained with these techniques.

4. Conclusions

The main objective pursued during this work was the development and implementation of a new methodology for studying H-material interaction. This method is based on in-situ charging materials with H plasma inside an SEM, while performing a tensile test. It provides well-defined material, mechanical and environmental factors, which is essential in the investigation of H effects. Even though there is a gradient in the H concentration since the charging is conducted from one side of the sample, there is a constant supply of H, which leads to a dynamic equilibrium of concentration.

Compared with conventional approaches, where having direct observation combined with in-situ H charging can be very challenging, this method represents a valuable tool, especially considering materials with high H diffusivity. Moreover, H concentration in the material can be calculated with a simple analytical model or with a more sophisticated simulation model.

To validate the method, the effect of H on three materials was investigated. In the solution annealed Alloy 718, H increased the crack propagation rate and decreased the ductility of the studied samples. Moreover, fracture surfaces changed from ductile microvoid coalescence to brittle intergranular failure and quasi-cleave with river marking features.

Regarding the CP steel, the H concentration in the material was rather low, and slightly below the critical value to produce embrittlement. Anyways, slight modifications in fracture characteristics and crack propagation rates were evident.

In regard to the tungsten heavy alloy, it was shown that the ductility was greatly affected in the presence of H, and even though the fracture morphology did not exhibit any drastic changes, the investigation of the crack propagation path showed that the failure changed from mostly transgranular to intergranular.

All of the previous results correspond to a certain range of H concentrations. In order to determine whether the materials are suitable for the required application, the H concentration, under which they will have to perform, needs also to be taken into account.

In addition, the current status of in-situ and in-operando methods were investigated and reviewed. Their applicability to study H-material interaction in H-related energy sources was demonstrated. All of these methods can provide valuable information previously not accessible and are key elements towards a green world.

The scientific research conducted within this work represents an important step in the H community since a unique versatile methodology was developed, which can be implemented in any laboratory and is applicable to any metallic sample.

5. References

[1] “International Energy Agency.” https://www.iea.org/data-and-statistics?country=WORLD&fuel=Energy supply&indicator=TPESbySource (accessed Mar. 19, 2021).

[2] M. Z. Jacobson, W. G. Colella, and D. M. Golden, “Atmospheric science: Cleaning the air and improving health with hydrogen fuel-cell vehicles,” *Science (80-.).*, vol. 308, no. 5730, pp. 1901–1905, 2005, doi: 10.1126/science.1109157.

[3] E. T. Sayed *et al.*, “Direct urea fuel cells: Challenges and opportunities,” *J. Power Sources*, vol. 417, no. January, pp. 159–175, 2019, doi: 10.1016/j.jpowsour.2018.12.024.

[4] R. O’Hayre, S.-W. Cha, W. G. Colella, and F. B. Prinz, *Fuel Cell Fundamentals*, Third Edit. New Jersey: Wiley, 2016.

[5] A. G. Olabi, T. Wilberforce, and M. A. Abdelkareem, “Fuel cell application in the automotive industry and future perspective,” *Energy*, vol. 214, p. 118955, 2021, doi: 10.1016/j.energy.2020.118955.

[6] S. S. Hsieh, B. S. Her, and Y. J. Huang, “Effect of pressure drop in different flow fields on water accumulation and current distribution for a micro PEM fuel cell,” *Energy Convers. Manag.*, vol. 52, no. 2, pp. 975–982, 2011, doi: 10.1016/j.enconman.2010.08.025.

[7] S. Fukuyama, M. Imade, and K. Yokogawa, “Development of new material testing apparatus in high-pressure hydrogen and evaluation of hydrogen gas embrittlement of metals,” 2007, doi: https://doi.org/10.1115/PVP2007-26820.

[8] Jari, “Technical standards for components (valve and PRD) for compressed-hydrogen vehicle fuel device,” 2004.

[9] L. Duprez, K. Verbeken, and M. Verhaege, “Effect of hydrogen on the mechanical properties of multiphase high-strength steels,” in *International Hydrogen Conference: Effects of hydrogen on materials*, 2008.

[10] J. Sanchez, S. F. Lee, M. A. Martin-Rengel, J. Fullea, C. Andrade, and J. Ruiz-Hervías, “Measurement of hydrogen and embrittlement of high strength steels,” *Eng. Fail. Anal.*, vol. 59, pp. 467–477, 2016, doi: 10.1016/j.engfailanal.2015.11.001.

[11] M. Loidl, O. Kolk, S. Veith, and T. Göbel, “Characterization of hydrogen embrittlement in automotive advanced high strength steels,” *Materwiss. Werksttech.*, vol. 42, no. 12, pp. 1105–1110, 2011, doi: 10.1002/mawe.201100917.

[12] C. Bergmann *et al.*, “Hydrogen embrittlement resistance evaluation of advanced high strength steels in automotive applications,” *SteelyHydrogen*, no. 1, p. A01, 2018, [Online].

Available: http://steelyhydrogen2018proc.be/articles/pdf/1.

[13] E. J. Ben Anthony, *Handbook of climate change mitigation*, vol. 4. 2016.

[14] D. M. Duffy, “Modeling plasma facing materials for fusion power,” *Mater. Today*, vol. 12, no. 11, pp. 38–44, 2009, doi: 10.1016/S1369-7021(09)70297-4.

[15] J. Linke *et al.*, “Challenges for plasma-facing components in nuclear fusion,” *Matter Radiat. Extrem.*, vol. 4, no. 5, 2019, doi: 10.1063/1.5090100.

[16] H. K. Yoon, S. H. Lee, S. J. L. Kang, and D. N. Yoon, “Effect of vacuum-treatment on mechanical properties of W-Ni-Fe heavy alloy,” *J. Mater. Sci.*, vol. 18, no. 5, pp. 1374–1380, 1983, doi: 10.1007/BF01111957.

[17] T. Depover, D. Pérez Escobar, E. Wallaert, Z. Zermout, and K. Verbeken, “Effect of hydrogen charging on the mechanical properties of advanced high strength steels,” *Int. J. Hydrogen Energy*, vol. 39, no. 9, pp. 4647–4656, 2014, doi: 10.1016/j.ijhydene.2013.12.190.

[18] T. Michler, C. San Marchi, J. Naumann, S. Weber, and M. Martin, “Hydrogen environment embrittlement of stable austenitic steels,” *Int. J. Hydrogen Energy*, vol. 37, no. 21, pp. 16231–16246, 2012, doi: 10.1016/j.ijhydene.2012.08.071.

[19] M. Koyama, C. C. Tasan, E. Akiyama, K. Tsuzaki, and D. Raabe, “Hydrogen-assisted decohesion and localized plasticity in dual-phase steel,” *Acta Mater.*, vol. 70, pp. 174–187, 2014, doi: 10.1016/j.actamat.2014.01.048.

[20] T. Kanezaki, C. Narazaki, Y. Mine, S. Matsuoka, and Y. Murakami, “Effects of hydrogen on fatigue crack growth behavior of austenitic stainless steels,” *Int. J. Hydrogen Energy*, vol. 33, no. 10, pp. 2604–2619, 2008, doi: 10.1016/j.ijhydene.2008.02.067.

[21] Z. Zhang, G. Obasis, R. Morana, and M. Preuss, “Hydrogen assisted crack initiation and propagation in a nickel-based superalloy,” *Acta Mater.*, vol. 113, pp. 272–283, 2016, doi: 10.1016/j.actamat.2016.05.003.

[22] Z. Tarzimoghadam, D. Ponge, J. Klöwer, and D. Raabe, “Hydrogen-assisted failure in Ni-based superalloy 718 studied under in situ hydrogen charging: The role of localized deformation in crack propagation,” *Acta Mater.*, vol. 128, pp. 365–374, 2017, doi: 10.1016/j.actamat.2017.02.059.

[23] J. He, S. Fukuyama, K. Yokogawa, and A. Kimura, “Effect of hydrogen on deformation structure of Inconel 718,” *Materials Transactions, JIM*, vol. 35, no. 10. pp. 689–694, 1994, doi: 10.2320/matertrans1989.35.689.

[24] M. F. Maday and L. Pilloni, “Hydrogen effects on the tensile and fatigue properties of Eurofer’97,” *Fusion Eng. Des.*, vol. 75–79, no. SUPPL., pp. 957–961, 2005, doi: 10.1016/j.fusengdes.2005.06.024.

[25] S. Lynch, “Hydrogen embrittlement phenomena and mechanisms,” *Corros. Rev.*, vol. 30, no. 3–4, pp. 105–123, 2012, doi: 10.1515/corrrev-2012-0502.

[26] J. Cwiek, “Prevention to hydrogen degradation of steel,” *Solid State Phenom.*, vol. 183, no. 1, pp. 31–36, 2012, doi: 10.4028/www.scientific.net/SSP.183.31.

[27] M. R. Louthan, “Hydrogen embrittlement of metals: A primer for the failure analyst,” *J. Fail. Anal. Prev.*, vol. 8, no. 3 SPEC. ISS., pp. 289–307, 2008, doi: 10.1007/s11668-008-9133-x.

[28] D. Figueroa and M. J. Robinson, “The effects of sacrificial coatings on hydrogen embrittlement and re-embrittlement of ultra high strength steels,” *Corros. Sci.*, vol. 50, no. 4, pp. 1066–1079, 2008, doi: 10.1016/j.corsci.2007.11.023.

[29] W. H. Johnson, “On some remarkable changes produced in iron and steel by the action of hydrogen and acids,” *Nature*, vol. 11, no. 281, p. 393, 1875, doi: 10.1038/011393a0.

[30] Y. Momotani, A. Shibata, D. Terada, and N. Tsuji, “Hydrogen Embrittlement Behavior at Different Strain Rates in Low-carbon Martensitic Steel,” *Mater. Today Proc.*, vol. 2, no. December, pp. S735–S738, 2015, doi: 10.1016/j.matpr.2015.07.387.

[31] J. Rehrl, K. Mraczek, A. Pichler, and E. Werner, “Mechanical properties and fracture behavior of hydrogen charged AHSS/UHSS grades at high- and low strain rate tests,” *Mater. Sci. Eng. A*, vol. 590, pp. 360–367, 2014, doi: 10.1016/j.msea.2013.10.044.

[32] J. Venezuela, Q. Liu, M. Zhang, Q. Zhou, and A. Atrens, “A review of hydrogen embrittlement of martensitic advanced high-strength steels,” *Corros. Rev.*, vol. 34, no. 3, pp. 153–186, 2016, doi: 10.1515/corrrev-2016-0006.

[33] F. Galliano, E. Andrieu, C. Blanc, J. M. Cloue, D. Connetable, and G. Odemer, “Effect of trapping and temperature on the hydrogen embrittlement susceptibility of alloy 718,” *Mater. Sci. Eng. A*, vol. 611, pp. 370–382, 2014, doi: 10.1016/j.msea.2014.06.015.

[34] G. Han, S. He, S. Fukuyama, and K. Yokogawa, “Effect of Nickel Equivalent on Hydrogen Environment Embrittlement of Austenitc Stainless Steels at Low Temperatures,” *Acta Mater.*, vol. 46, no. 13, pp. 4599–4570, 1998.

[35] S. P. Lynch, “Environmentally assisted cracking: Overview of evidence for an adsorption-induced localised-slip process,” *Acta Metall.*, vol. 36, no. 10, pp. 2639–2661, 1988, doi: 10.1016/0001-6160(88)90113-7.

[36] R. G. Davies, “Hydrogen Embrittlement of Dual-Phase Steels.,” *Metall. Trans. A, Phys. Metall. Mater. Sci.*, vol. 12 A, no. 9, pp. 1667–1672, 1981, doi: 10.1007/BF02643572.

[37] P. D. Hicks and C. J. Altstetter, “Hydrogen-enhanced cracking of superalloys,” *Metall. Trans. A*, vol. 23, no. 1, pp. 237–249, 1992, doi: 10.1007/BF02660868.

[38] N. Eliaz, A. Shachar, B. Tal, and D. Eliezer, “Characteristics of hydrogen embrittlement, stress

corrosion cracking and tempered martensite embrittlement in high-strength steels," *Eng. Fail. Anal.*, vol. 9, no. 2, pp. 167–184, 2002, doi: 10.1016/S1350-6307(01)00009-7.

[39] D. Hardie, E. A. Charles, and A. H. Lopez, "Hydrogen embrittlement of high strength pipeline steels," *Corros. Sci.*, vol. 48, no. 12, pp. 4378–4385, 2006, doi: 10.1016/j.corsci.2006.02.011.

[40] M. Wang, E. Akiyama, and K. Tsuzaki, "Effect of hydrogen on the fracture behavior of high strength steel during slow strain rate test," *Corros. Sci.*, vol. 49, no. 11, pp. 4081–4097, 2007, doi: 10.1016/j.corsci.2007.03.038.

[41] A. Barnoush and H. Vehoff, "Hydrogen embrittlement of aluminum in aqueous environments examined by in situ electrochemical nanoindentation," *Scr. Mater.*, vol. 58, no. 9, pp. 747–750, 2008, doi: 10.1016/j.scriptamat.2007.12.019.

[42] J. Sanchez, J. Fullea, C. Andrade, and P. De Andres, "Hydrogen embrittlement of high strength steels," *Defect Diffus. Forum*, vol. 289–292, pp. 203–209, 2009, doi: 10.4028/www.scientific.net/DDF.289-292.203.

[43] X. Lu, D. Wang, D. Wan, Z. B. Zhang, N. Kheradmand, and A. Barnoush, "Effect of electrochemical charging on the hydrogen embrittlement susceptibility of alloy 718," *Acta Mater.*, vol. 179, no. 7491, pp. 36–48, 2019, doi: 10.1016/j.actamat.2019.08.020.

[44] S. K. Dwivedi and M. Vishwakarma, "Hydrogen embrittlement in different materials: A review," *Int. J. Hydrogen Energy*, vol. 43, no. 46, pp. 21603–21616, 2018, doi: 10.1016/j.ijhydene.2018.09.201.

[45] A. Barnoush and H. Vehoff, "Recent developments in the study of hydrogen embrittlement: Hydrogen effect on dislocation nucleation," *Acta Mater.*, vol. 58, no. 16, pp. 5274–5285, 2010, doi: 10.1016/j.actamat.2010.05.057.

[46] H.K.D.H. Bhadeshia, "Prevention of Hydrogen Embrittlement in Steels," *ISIJ Int.*, vol. 56, no. 1, pp. 24–36, 2016.

[47] J. Woodtli and R. Kieselbach, "Damage due to hydrogen embrittlement and stress corrosion cracking," *Eng. Fail. Anal.*, vol. 7, no. 6, pp. 427–450, 2000, doi: 10.1016/S1350-6307(99)00033-3.

[48] S. V. Brahimi, S. Yue, and K. R. Sriraman, "Alloy and composition dependence of hydrogen embrittlement susceptibility in high-strength steel fasteners," *Philos. Trans. R. Soc. A Math. Phys. Eng. Sci.*, vol. 375, no. 2098, 2017, doi: 10.1098/rsta.2016.0407.

[49] S. E. Brahimi, "Fundamentals of Hydrogen Embrittlement in Steel Fasteners," *IBECA Technol. Corp*, pp. 1–23, 2014.

[50] D. M. Symons, "A comparison of internal hydrogen embrittlement and hydrogen environment embrittlement of X-750," *Eng. Fract. Mech.*, vol. 68, no. 6, pp. 751–771, 2001,

doi: 10.1016/S0013-7944(00)00123-5.

[51] A. H. M. Krom and A. D. Bakker, “Hydrogen trapping models in steel,” *Metall. Mater. Trans. B Process Metall. Mater. Process. Sci.*, vol. 31, no. 6, pp. 1475–1482, 2000, doi: 10.1007/s11663-000-0032-0.

[52] Y. Fukai and H. Sugimoto, “Advances in Physics Diffusion of hydrogen in metals,” *Adv. Phys.*, vol. 34, no. 2, pp. 263–326, 2006.

[53] H. Wipf, “Solubility and-diffusion of hydrogen in pure metals and alloys,” *Phys. Scr. T*, vol. 94, pp. 43–51, 2001, doi: 10.1238/physica.topical.094a00043.

[54] W. Gerberich, “Gaseous hydrogen embrittlement of materials in energy technologies,” R. P. Gangloff and B. P. Somerday, Eds. Cambridge: Woodhead Publishing Limited, 2012, pp. 209–246.

[55] S. Lynch, “Discussion of some recent literature on hydrogen-embrittlement mechanisms: Addressing common misunderstandings,” *Corros. Rev.*, no. ii, 2019, doi: 10.1515/corrrev-2019-0017.

[56] W. W. Gerberich, R. A. Oriani, M. J. Lji, X. Chen, and T. Foecke, “The necessity of both plasticity and brittleness in the fracture thresholds of iron,” *Philos. Mag. A Phys. Condens. Matter, Struct. Defects Mech. Prop.*, vol. 63, no. 2, pp. 363–376, 1991, doi: 10.1080/01418619108204854.

[57] R. A. Oriani and P. H. Josephic, “Equilibrium aspects of hydrogen-induced cracking of steels,” *Acta Metall.*, vol. 22, no. 9, pp. 1065–1074, 1974, doi: 10.1016/0001-6160(74)90061-3.

[58] R. P. Gangloff, “Hydrogen Assisted Cracking of High Strength Alloys,” in *Comprehensive Structural Integrity*, I. Milne, R. O. Ritchie, and B. Karihaloo, Eds. New York: Elsevier, 2003, pp. 31–101.

[59] C. D. Beachem, “A new model for hydrogen-assisted cracking (hydrogen ‘embrittlement’),” *Metall. Trans.*, vol. 3, no. 2, pp. 441–455, 1972, doi: 10.1007/BF02642048.

[60] I. M. Robertson and H. K. Birnbaum, “An HVEM study of hydrogen effects on the deformation and fracture of nickel,” *Acta Metall.*, vol. 34, no. 3, pp. 353–366, 1986, doi: 10.1016/0001-6160(86)90071-4.

[61] I. M. Robertson *et al.*, “Hydrogen Embrittlement Understood,” *Metall. Mater. Trans. B Process Metall. Mater. Process. Sci.*, vol. 46, no. 3, pp. 1085–1103, 2015, doi: 10.1007/s11663-015-0325-y.

[62] H. K. Birnbaum and P. Sofronis, “Hydrogen-enhanced localized plasticity-a mechanism for hydrogen-related fracture,” *Mater. Sci. Eng. A*, vol. 176, no. 1–2, pp. 191–202, 1994, doi: 10.1016/0921-5093(94)90975-X.

[63] T. Tabata and H. K. Birnbaum, "Direct observation of the effect of hydrogen on the behavior of dislocations in iron," *Scr. Metall.*, vol. 17, no. c, pp. 947–950, 1983.

[64] D. F. Teter, I. M. Robertson, and H. K. Birnbaum, "The effects of hydrogen on the deformation and fracture of β-titanium," *Acta Mater.*, vol. 49, no. 20, pp. 4313–4323, 2001, doi: 10.1016/S1359-6454(01)00301-9.

[65] Y. Jagodzinski, H. Hänninen, O. Tarasenko, and S. Smuk, "Interaction of hydrogen with dislocation pile-ups and hydrogen induced softening of pure iron," *Scr. Mater.*, vol. 43, no. 3, pp. 245–251, 2000, doi: 10.1016/S1359-6462(00)00398-5.

[66] G. M. Bond, I. M. Robertson, and H. K. Birnbaum, "On the determination of the hydrogen fugacity in an environmental cell TEM facility," *Scr. Metall.*, vol. 20, pp. 653–658, 1986, [Online]. Available: https://scholar.google.co.id/scholar?hl=id&as_sdt=0%2C5&q=kemasyarakatan+bahasa+teori+firth&btnG=#d=gs_qabs&u=%23p%3DtfGdLLvHmhYJ.

[67] S. P. Lynch, "Metallographic contributions to understanding mechanisms of environmentally assisted cracking," *Metallography*, vol. 23, no. 2, pp. 147–171, 1989, doi: 10.1016/0026-0800(89)90016-5.

[68] S. P. Lynch, "Interpreting hydrogen-induced fracture surfaces in terms of deformation processes: A new approach," *Scr. Mater.*, vol. 65, no. 10, pp. 851–854, 2011, doi: 10.1016/j.scriptamat.2011.06.016.

[69] S. P. Lynch, "Comments on 'A unified model of environment-assisted cracking,'" *Scr. Mater.*, vol. 61, no. 3, pp. 331–334, 2009, doi: 10.1016/j.scriptamat.2009.02.031.

[70] Y. Kim, Y. J. Chao, M. J. Pechersky, and M. J. Morgan, "On the effect of hydrogen on the fracture toughness of steel," *Int. J. Fract.*, vol. 134, no. 3–4, pp. 339–347, 2005, doi: 10.1007/s10704-005-1974-7.

[71] J. Song and W. A. Curtin, "Atomic mechanism and prediction of hydrogen embrittlement in iron," *Nat. Mater.*, vol. 12, no. 2, pp. 145–151, 2013, doi: 10.1038/nmat3479.

[72] B. R. S. Rogne, N. Kheradmand, Y. Deng, and A. Barnoush, "In situ micromechanical testing in environmental scanning electron microscope: A new insight into hydrogen-assisted cracking," *Acta Mater.*, vol. 144, pp. 257–268, 2018, doi: 10.1016/j.actamat.2017.10.037.

[73] Y. Deng, T. Hajilou, D. Wan, N. Kheradmand, and A. Barnoush, "In-situ micro-cantilever bending test in environmental scanning electron microscope: Real time observation of hydrogen enhanced cracking," *Scr. Mater.*, vol. 127, pp. 19–23, 2017, doi: 10.1016/j.scriptamat.2016.08.026.

[74] I. Taji, T. Hajilou, and F. S. A. Barnoush, "In situ electrochemical micro - cantilever bending

test of Ni based superalloys," 2019.

[75] T. Hajilou, Y. Deng, B. R. Rogne, N. Kheradmand, and A. Barnoush, "In situ electrochemical microcantilever bending test: A new insight into hydrogen enhanced cracking," *Scr. Mater.*, vol. 132, pp. 17–21, 2017, doi: 10.1016/j.scriptamat.2017.01.019.

[76] Y. Murakami, T. Kanezaki, Y. Mine, and S. Matsuoka, "Hydrogen embrittlement mechanism in fatigue of austenitic stainless steels," *Metall. Mater. Trans. A Phys. Metall. Mater. Sci.*, vol. 39 A, no. 6, pp. 1327–1339, 2008, doi: 10.1007/s11661-008-9506-5.

[77] H. Uyama, M. Nakashima, K. Morishige, Y. Mine, and Y. Murakami, "Effects of hydrogen charge on microscopic fatigue behaviour of annealed carbon steels," *Fatigue Fract. Eng. Mater. Struct.*, vol. 29, no. 12, pp. 1066–1074, 2006, doi: 10.1111/j.1460-2695.2006.01069.x.

[78] Y. Ogawa, H. Matsunaga, J. Yamabe, M. Yoshikawa, and S. Matsuoka, "Unified evaluation of hydrogen-induced crack growth in fatigue tests and fracture toughness tests of a carbon steel," *Int. J. Fatigue*, vol. 103, pp. 223–233, 2017, doi: 10.1016/j.ijfatigue.2017.06.006.

[79] H. Vehoff and P. Neumann, "Crack propagation and cleavage initiation in Fe-2.6%-Si single crystals under controlled plastic crack tip opening rate in various gaseous environments," *Acta Metall.*, vol. 28, no. 3, pp. 265–272, 1980, doi: 10.1016/0001-6160(80)90161-3.

[80] A. Massone *et al.*, "An SEM compatible plasma cell for in situ studies of hydrogen-material interaction," *Rev. Sci. Instrum.*, vol. 91, no. 4, 2020, doi: 10.1063/1.5142043.

[81] D. Wan, Y. Deng, and A. Barnoush, "Hydrogen embrittlement effect observed by in-situ hydrogen plasma charging on a ferritic alloy," *Scr. Mater.*, vol. 151, no. April, pp. 24–27, 2018, doi: 10.1016/j.scriptamat.2018.03.038.

[82] A. Barnoush and H. Vehoff, "In situ electrochemical nanoindentation: A technique for local examination of hydrogen embrittlement," *Corros. Sci.*, vol. 50, no. 1, pp. 259–267, 2008, doi: 10.1016/j.corsci.2007.05.026.

[83] A. S. Ebner, S. Brinckmann, E. Plesiutschnig, H. Clemens, R. Pippan, and V. Maier-Kiener, "A Modified Electrochemical Nanoindentation Setup for Probing Hydrogen-Material Interaction Demonstrated on a Nickel-Based Alloy," *Jom*, vol. 72, no. 5, pp. 2020–2029, 2020, doi: 10.1007/s11837-020-04104-9.

[84] M. J. Duarte, X. Fang, J. Rao, W. Krieger, S. Brinckmann, and G. Dehm, "In situ nanoindentation during electrochemical hydrogen charging: a comparison between front-side and a novel back-side charging approach," *J. Mater. Sci.*, 2021, doi: 10.1007/s10853-020-05749-2.

[85] A. Barnoush and H. Vehoff, "Electrochemical nanoindentation: A new approach to probe hydrogen/deformation interaction," *Scr. Mater.*, vol. 55, no. 2, pp. 195–198, 2006, doi:

10.1016/j.scriptamat.2006.03.041.

[86] X. Li, Y. Wang, P. Zhang, B. Li, X. Song, and J. Chen, “Effect of pre-strain on hydrogen embrittlement of high strength steels,” *Mater. Sci. Eng. A*, vol. 616, pp. 116–122, 2014, doi: 10.1016/j.msea.2014.07.085.

[87] T. Zakroczymski, A. Glowacka, and W. Swiatnicki, “Effect of hydrogen concentration on the embrittlement of a duplex stainless steel,” *Corros. Sci.*, vol. 47, no. 6, pp. 1403–1414, 2005, doi: 10.1016/j.corsci.2004.07.036.

[88] G. Lovicu *et al.*, “Hydrogen embrittlement of automotive advanced high-strength steels,” *Metall. Mater. Trans. A Phys. Metall. Mater. Sci.*, vol. 43, no. 11, pp. 4075–4087, 2012, doi: 10.1007/s11661-012-1280-8.

[89] T. Depover, T. Hajilou, D. Wan, D. Wang, A. Barnoush, and K. Verbeken, “Assessment of the potential of hydrogen plasma charging as compared to conventional electrochemical hydrogen charging on dual phase steel,” *Mater. Sci. Eng. A*, vol. 754, no. March, pp. 613–621, 2019, doi: 10.1016/j.msea.2019.03.097.

[90] I. M. Robertson, “The effect of hydrogen on dislocation dynamics,” *Eng. Fract. Mech.*, vol. 68, no. 6, pp. 671–692, 2001, doi: 10.1016/S0013-7944(01)00011-X.

[91] Y. Deng and A. Barnoush, “Hydrogen embrittlement revealed via novel in situ fracture experiments using notched micro-cantilever specimens,” *Acta Mater.*, vol. 142, pp. 236–247, 2018, doi: 10.1016/j.actamat.2017.09.057.

[92] J. Kim and C. C. Tasan, “Microstructural and micro-mechanical characterization during hydrogen charging: An in situ scanning electron microscopy study,” *Int. J. Hydrogen Energy*, vol. 44, no. 12, pp. 6333–6343, 2019, doi: 10.1016/j.ijhydene.2018.10.128.

[93] D. Wang, X. Lu, Y. Deng, X. Guo, and A. Barnoush, “Effect of hydrogen on nanomechanical properties in Fe-22Mn-0.6C TWIP steel revealed by in-situ electrochemical nanoindentation,” *Acta Mater.*, vol. 166, pp. 618–629, 2019, doi: 10.1016/j.actamat.2018.12.055.

[94] A. Barnoush, C. Bies, and H. Vehoff, “In situ electrochemical nanoindentation of FeAl (100) single crystal: Hydrogen effect on dislocation nucleation,” *J. Mater. Res.*, vol. 24, no. 3, pp. 1105–1113, 2009, doi: 10.1557/jmr.2009.0084.

[95] D. Wan, Y. Deng, J. I. H. Meling, A. Alvaro, and A. Barnoush, “Hydrogen-enhanced fatigue crack growth in a single-edge notched tensile specimen under in-situ hydrogen charging inside an environmental scanning electron microscope,” *Acta Mater.*, vol. 170, pp. 87–99, 2019, doi: 10.1016/j.actamat.2019.03.032.

[96] A. Massone *et al.*, “Addressing H-Material Interaction in Fast Diffusion Materials—a Feasibility Study on a Complex Phase Steel,” *Materials (Basel).*, vol. 13, no. 20, p. 4677, Oct.

2020, doi: 10.3390/ma13204677.

[97] A. Mutzke *et al.*, “SDTrimSP.” Max-Planck-Institut für Plasmaphysik, Garching, 2019.

[98] W. M. Shu, Y. Hayashi, and K. Okuno, “Regime diagram of plasma-driven hydrogen transport through metals,” *Philos. Mag. B Phys. Condens. Matter; Stat. Mech. Electron. Opt. Magn. Prop.*, vol. 72, no. 3, pp. 301–309, 1995, doi: 10.1080/13642819508239085.

[99] H. Zhou, Y. Hirooka, N. Ashikawa, T. Muroga, and A. Sagara, “Gas- and plasma-driven hydrogen permeation through a reduced activation ferritic steel alloy F82H,” *J. Nucl. Mater.*, vol. 455, no. 1–3, pp. 470–474, 2014, doi: 10.1016/j.jnucmat.2014.07.061.

[100] M. I. Baskes, “A calculation of the surface recombination rate constant for hydrogen isotopes on metals,” *J. Nucl. Mater.*, vol. 92, no. 2–3, pp. 318–324, 1980, doi: 10.1016/0022-3115(80)90117-8.

[101] G. Stenerud, S. Wenner, J. S. Olsen, and R. Johnsen, “Effect of different microstructural features on the hydrogen embrittlement susceptibility of alloy 718,” *Int. J. Hydrogen Energy*, vol. 43, no. 13, pp. 6765–6776, 2018, doi: 10.1016/j.ijhydene.2018.02.088.

[102] Z. Zhang, G. Obasi, R. Morana, and M. Preuss, “In-situ observation of hydrogen induced crack initiation in a nickel-based superalloy,” *Scr. Mater.*, vol. 140, pp. 40–44, 2017, doi: 10.1016/j.scriptamat.2017.07.006.

[103] Z. Tarzimoghadam *et al.*, “Multi-scale and spatially resolved hydrogen mapping in a Ni-Nb model alloy reveals the role of the δ phase in hydrogen embrittlement of alloy 718,” *Acta Mater.*, vol. 109, pp. 69–81, 2016, doi: 10.1016/j.actamat.2016.02.053.

[104] X. Lu, Y. Ma, and D. Wang, “On the hydrogen embrittlement behavior of nickel-based alloys: Alloys 718 and 725,” *Mater. Sci. Eng. A*, vol. 792, no. June, 2020, doi: 10.1016/j.msea.2020.139785.

[105] L. Fournier, D. Delafosse, and T. Magnin, “Cathodic hydrogen embrittlement in alloy 718,” *Mater. Sci. Eng. A*, vol. 269, no. 1–2, pp. 111–119, 1999, doi: 10.1016/S0921-5093(99)00167-7.

[106] D. K. Matlock, J. G. Speer, E. De Moor, and P. J. Gibbs, “Recent developments in advanced high strength steels for automotive applications: An overview,” *Jestech*, vol. 15, no. 1, pp. 1–12, 2012.

[107] A. Drexler *et al.*, “On the local evaluation of the hydrogen susceptibility of cold-formed and heat treated advanced high strength steel (AHSS) sheets,” *Mater. Sci. Eng. A*, vol. 800, no. June 2020, p. 140276, 2021, doi: 10.1016/j.msea.2020.140276.

[108] M. Li, D. Ruprecht, G. Kracker, T. Höschen, and R. Neu, “Impact of heat treatment on tensile properties of 97W–2Ni–1Fe heavy alloy,” *J. Nucl. Mater.*, vol. 512, pp. 1–7, 2018, doi:

10.1016/j.jnucmat.2018.09.055.

[109] H. Maier *et al.*, “Deuterium retention in tungsten based materials for fusion applications,” *Nucl. Mater. Energy*, vol. 18, no. July 2018, pp. 245–249, 2019, doi: 10.1016/j.nme.2018.12.032.

[110] A. Massone and D. Kiener, “Prospects of enhancing the understanding of material-hydrogen interaction by novel in-situ and in-operando methods,” *Renew. Sustain. Energy Rev.*, 2021.

[111] L. Liu, C. Zhai, C. Lu, W. Ding, A. Hirose, and K. F. Kobayashi, “Study of the effect of δ phase on hydrogen embrittlement of Inconel 718 by notch tensile tests,” *Corros. Sci.*, vol. 47, no. 2, pp. 355–367, 2005, doi: 10.1016/j.corsci.2004.06.008.

[112] V. Demetriou, J. D. Robson, M. Preuss, and R. Morana, “Study of the effect of hydrogen charging on the tensile properties and microstructure of four variant heat treatments of nickel alloy 718,” *Int. J. Hydrogen Energy*, vol. 42, no. 37, pp. 23856–23870, 2017, doi: 10.1016/j.ijhydene.2017.02.149.

[113] T. Michler, A. A. Yukhimchuk, and J. Naumann, “Hydrogen environment embrittlement testing at low temperatures and high pressures,” *Corros. Sci.*, vol. 50, no. 12, pp. 3519–3526, 2008, doi: 10.1016/j.corsci.2008.09.025.

[114] M. Koyama *et al.*, “Hydrogen desorption and cracking associated with martensitic transformation in Fe-Cr-Ni-Based austenitic steels with different carbon contents,” *Int. J. Hydrogen Energy*, vol. 42, no. 42, pp. 26423–26435, 2017, doi: 10.1016/j.ijhydene.2017.08.209.

[115] M. Kaur and K. Pal, “Review on hydrogen storage materials and methods from an electrochemical viewpoint,” *J. Energy Storage*, vol. 23, no. March, pp. 234–249, 2019, doi: 10.1016/j.est.2019.03.020.

[116] P. P. Edwards, V. L. Kuznetsov, and W. I. F. David, “Hydrogen energy,” *Philos. Trans. R. Soc. A Math. Phys. Eng. Sci.*, vol. 365, no. 1853, pp. 1043–1056, 2007, doi: 10.1098/rsta.2006.1965.

[117] F. Khalid, I. Dincer, and M. A. Rosen, “Analysis and assessment of an integrated hydrogen energy system,” *Int. J. Hydrogen Energy*, vol. 41, no. 19, pp. 7960–7967, 2016, doi: 10.1016/j.ijhydene.2015.12.221.

[118] G. W. Crabtree, M. S. Dresselhaus, and M. V. Buchanan, “The hydrogen economy,” *Phys. Today*, vol. 57, no. 12, pp. 39–44, 2004, doi: 10.1063/1.1878333.

[119] A. Züttel, “Materials for hydrogen storage,” *Mater. Today*, vol. 6, no. 9, pp. 24–33, 2003, doi: 10.1016/S1369-7021(03)00922-2.

[120] P. Millet, *Hydrogen storage in hydride-forming materials*. Woodhead Publishing Limited, 2014.

[121] G. R. Odette and S. J. Zinkle, *Structural alloys for nuclear energy applications*. Elsevier, 2019.

[122] J. M. Bell, Y. D. Chin, and S. Hanrahan, “State-of-the-art of ultra deepwater production technologies,” *Proc. Annu. Offshore Technol. Conf.*, vol. 2005-May, pp. 1875–1887, 2005, doi: 10.4043/17615-ms.

[123] M. Iannuzzi, A. Barnoush, and R. Johnsen, “Materials and corrosion trends in offshore and subsea oil and gas production,” *npj Mater. Degrad.*, vol. 1, no. 1, 2017, doi: 10.1038/s41529-017-0003-4.

[124] T. E. Perez, “Corrosion in the oil and gas industry: An increasing challenge for materials,” *Jom*, vol. 65, no. 8, pp. 1033–1042, 2013, doi: 10.1007/s11837-013-0675-3.

[125] M. D. Uchic, D. M. Dimiduk, J. N. Florando, and W. D. Nix, “Sample dimensions influence strength and crystal plasticity,” *Science (80-.).*, vol. 305, no. 5686, pp. 986–989, 2004, doi: 10.1126/science.1098993.

[126] S. Korte and W. J. Clegg, “Studying plasticity in hard and soft Nb-Co intermetallics,” *Adv. Eng. Mater.*, vol. 14, no. 11, pp. 991–997, 2012, doi: 10.1002/adem.201200175.

[127] F. Östlund *et al.*, “Ductile-brittle transition in micropillar compression of GaAs at room temperature,” *Philos. Mag.*, vol. 91, no. 7–9, pp. 1190–1199, 2011, doi: 10.1080/14786435.2010.509286.

[128] S. Korte, J. S. Barnard, R. J. Stearn, and W. J. Clegg, “Deformation of silicon - Insights from microcompression testing at 25-500 °c,” *Int. J. Plast.*, vol. 27, no. 11, pp. 1853–1866, 2011, doi: 10.1016/j.ijplas.2011.05.009.

[129] D. Kiener, P. Hosemann, S. A. Maloy, and A. M. Minor, “In situ nanocompression testing of irradiated copper,” *Nat. Mater.*, vol. 10, no. 8, pp. 608–613, 2011, doi: 10.1038/nmat3055.

[130] T. S. Jun, Z. Zhang, G. Sernicola, F. P. E. Dunne, and T. B. Britton, “Local strain rate sensitivity of single α phase within a dual-phase Ti alloy,” *Acta Mater.*, vol. 107, pp. 298–309, 2016, doi: 10.1016/j.actamat.2016.01.057.

[131] T. B. Britton, H. Liang, F. P. E. Dunne, and A. J. Wilkinson, “The effect of crystal orientation on the indentation response of commercially pure titanium: Experiments and simulations,” *Proc. R. Soc. A Math. Phys. Eng. Sci.*, vol. 466, no. 2115, pp. 695–719, 2010, doi: 10.1098/rspa.2009.0455.

[132] Y. Liu *et al.*, “Experimentally quantifying critical stresses associated with basal slip and twinning in magnesium using micropillars,” *Acta Mater.*, vol. 135, pp. 411–421, 2017, doi: 10.1016/j.actamat.2017.06.008.

[133] T. Glechner *et al.*, “Assessment of ductile character in superhard Ta-C-N thin films,” *Acta Mater.*, vol. 179, pp. 17–25, 2019, doi: 10.1016/j.actamat.2019.08.015.

[134] V. Maier-Kiener, B. Schuh, E. P. George, H. Clemens, and A. Hohenwarter, "Nanoindentation testing as a powerful screening tool for assessing phase stability of nanocrystalline high-entropy alloys," *Mater. Des.*, vol. 115, pp. 479–485, 2017, doi: 10.1016/j.matdes.2016.11.055.

[135] A. Leitner, V. Maier-Kiener, and D. Kiener, "Essential refinements of spherical nanoindentation protocols for the reliable determination of mechanical flow curves," *Mater. Des.*, vol. 146, pp. 69–80, 2018, doi: 10.1016/j.matdes.2018.03.003.

[136] M. Burtscher, M. Alfreider, K. Schmuck, H. Clemens, S. Mayer, and D. Kiener, "In situ fracture observations of distinct interface types within a fully lamellar intermetallic TiAl alloy," 2020, doi: 10.1557/jmr.2020.306.

[137] H. Vehoff and W. Rothe, *GASEOUS HYDROGEN EMBRITTLEMENT IN FeSi- AND Ni-SINGLE CRYSTALS.*, no. 30. Pergamon Books Ltd, 1986.

[138] T. Schober and C. Dieker, "Observation of local hydrogen on nickel surfaces," *Metall. Trans. A*, vol. 14, no. 11, pp. 2440–2442, 1983, doi: 10.1007/BF02663321.

[139] M. Koyama, D. Yamasaki, T. Nagashima, C. C. Tasan, and K. Tsuzaki, "In situ observations of silver-decoration evolution under hydrogen permeation: Effects of grain boundary misorientation on hydrogen flux in pure iron," *Scr. Mater.*, vol. 129, pp. 48–51, 2017, doi: 10.1016/j.scriptamat.2016.10.027.

[140] A. Lasia and D. Grégoire, "General Model of Electrochemical Hydrogen Absorption into Metals," *J. Electrochem. Soc.*, vol. 142, no. 10, pp. 3393–3399, 1995, doi: 10.1149/1.2050267.

[141] W. Shu, K. Okuno, and Y. Hayashi, "Ion-driven permeation of deuterium in metals," *Jaeri-M*, vol. 43, 1993.

[142] J. Y. Lee and S. M. Lee, "Hydrogen trapping phenomena in metals with B.C.C. and F.C.C. crystals structures by the desorption thermal analysis technique," *Surf. Coatings Technol.*, vol. 28, no. 3–4, pp. 301–314, 1986, doi: 10.1016/0257-8972(86)90087-3.

[143] B. L. Doyle and D. K. Brice, "Steady state hydrogen transport in solids," *Radiat. Eff.*, vol. 89, no. 1–2, pp. 21–48, 1985, doi: 10.1080/00337578508220694.

[144] M. Asadipoor, J. Kadkhodapour, A. Pourkamali Anaraki, S. M. H. Sharifi, A. C. Darabi, and A. Barnoush, "Experimental and Numerical Investigation of Hydrogen Embrittlement Effect on Microdamage Evolution of Advanced High-Strength Dual-Phase Steel," *Met. Mater. Int.*, no. 0123456789, 2020, doi: 10.1007/s12540-020-00681-1.

[145] M. Wang, E. Akiyama, and K. Tsuzaki, "Determination of the critical hydrogen concentration for delayed fracture of high strength steel by constant load test and numerical calculation," *Corros. Sci.*, vol. 48, no. 8, pp. 2189–2202, 2006, doi: 10.1016/j.corsci.2005.07.010.

[146] H. S. Klapper, J. Klöwer, and O. Gosheva, “Hydrogen embrittlement: The game changing factor in the applicability of nickel alloys in oilfield technology,” *Philos. Trans. R. Soc. A Math. Phys. Eng. Sci.*, vol. 375, no. 2098, 2017, doi: 10.1098/rsta.2016.0415.

[147] H. Yamada, “Fusion Energy,” in *Handbook of Climate Change Mitigation*, W. Y. Chen, J. Seiner, T. Suzuki, and M. Lackner, Eds. New York: Springer US, 2012.

[148] W. Jacob, C. Linsmeier, and M. Rubel, “13th International Workshop on Plasma-Facing Materials and Components for Fusion Applications/1st International Conference on Fusion Energy Materials Science,” *Phys. Scr. T*, vol. T145, 2011, doi: 10.1088/0031-8949/2011/T145/011001.

[149] J. Roth and K. Schmid, “Hydrogen in tungsten as plasma-facing material,” *Phys. Scr. T*, vol. T145, 2011, doi: 10.1088/0031-8949/2011/T145/014031.

[150] A. Manhard, K. Schmid, M. Balden, and W. Jacob, “Influence of the microstructure on the deuterium retention in tungsten,” *J. Nucl. Mater.*, vol. 415, no. 1 SUPPL, pp. S632–S635, 2011, doi: 10.1016/j.jnucmat.2010.10.045.

[151] L. Gao *et al.*, “Deuterium supersaturation in low-energy plasma-loaded tungsten surfaces,” *Nucl. Fusion*, vol. 57, no. 1, p. 16026, 2017, doi: 10.1088/0029-5515/57/1/016026.

[152] Y. Zayachuk, A. Manhard, M. H. J. ’T Hoen, W. Jacob, P. A. Zeijlmans Van Emmichoven, and G. Van Oost, “Depth profiling of the modification induced by high-flux deuterium plasma in tungsten and tungsten-tantalum alloys,” *Nucl. Fusion*, vol. 54, no. 12, 2014, doi: 10.1088/0029-5515/54/12/123013.

[153] J. Bellosta von Colbe *et al.*, “Application of hydrides in hydrogen storage and compression: Achievements, outlook and perspectives,” *Int. J. Hydrogen Energy*, vol. 44, no. 15, pp. 7780–7808, 2019, doi: 10.1016/j.ijhydene.2019.01.104.

[154] L. Zhang, M. Wen, M. Imade, S. Fukuyama, and K. Yokogawa, “Effect of nickel equivalent on hydrogen gas embrittlement of austenitic stainless steels based on type 316 at low temperatures,” *Acta Mater.*, vol. 56, no. 14, pp. 3414–3421, 2008, doi: 10.1016/j.actamat.2008.03.022.

[155] J. Talonen and H. Hänninen, “Formation of shear bands and strain-induced martensite during plastic deformation of metastable austenitic stainless steels,” *Acta Mater.*, vol. 55, no. 18, pp. 6108–6118, 2007, doi: 10.1016/j.actamat.2007.07.015.

[156] R. M. Vennet and G. S. Ansell, “The effect of high-pressure hydrogen upon tensile properties and fracture behavior of 304L stainless steel,” *Trans. ASM*, vol. 60, pp. 242–251, 1967.

[157] R. B. Benson, R. K. Dann, and L. W. Roberts, “Hydrogen embrittlement of stainless steel,” *Trans. AIME*, vol. 242, pp. 2199–2205, 1968.

[158] R. C. Weast, M. J. Astle, and W. H. Beyer, *CRC handbook of chemistry and physics*, 64th ed. Boca Raton, Florida: CRC Press, 1983.

[159] M. L. Trudeau, “Advanced Materials for Energy Storage,” *MRS Bull.*, vol. 24, no. 11, pp. 23–26, Nov. 1999, doi: 10.1557/S0883769400053410.

[160] H. Yu, C. Hebling, and S. Revathi, “Fuel Cells: Microsystems,” *Ref. Modul. Mater. Sci. Mater. Eng.*, no. September 2015, pp. 1–15, 2016, doi: 10.1016/b978-0-12-803581-8.01727-6.

[161] I. Krylova, “Painting by electrodeposition on the eve of the 21st century,” *Prog. Org. Coatings*, vol. 42, no. 3–4, pp. 119–131, 2001, doi: 10.1016/S0300-9440(01)00146-1.

[162] Y. Liu, M. Wang, and G. Liu, “Effect of hydrogen on ductility of high strength 3Ni-Cr-Mo-V steels,” *Mater. Sci. Eng. A*, vol. 594, pp. 40–47, 2014, doi: 10.1016/j.msea.2013.11.058.

[163] T. B. Hilditch, S. B. Lee, J. G. Speer, and D. K. Matlock, “Response to hydrogen charging in high strength automotive sheet steel products,” *SAE Tech. Pap.*, no. 724, 2003, doi: 10.4271/2003-01-0525.

6. List of appended publications

Publication A

A. Massone, A. Manhard, W. Jacob, A. Drexler, W. Ecker, A. Hohenwarter, S. Wurster, D. Kiener
"*An SEM compatible plasma cell for in situ studies of hydrogen-material interaction"*
Review of Scientific Instruments 91 (2020) 043705, doi: https://doi.org/10.1063/1.5142043

Publication B

A. Massone, A. Manhard, A. Drexler, C. Posch, W. Ecker, V. Maier-Kiener, D. Kiener
"Addressing H-material interaction in fast diffusion materials- A feasibility study on a complex phase steel"
Materials 13 (2020) 4677, doi: https://doi.org/10.3390/ma13204677

Publication C

A. Massone, D. Kiener
"Prospects of enhancing the understanding of material-hydrogen interaction by novel in-situ and in-operando methods"
Submitted to Renewable and Sustainable Energy Reviews (2021)

Remark

In the appended papers, I, Agustina Massone, performed all experiments, data analyses and was primary author with the following exceptions:

- Armin Manhard and Wolfgang Jacob supported the construction of the experimental setup for Publication A.
- Andreas Drexler and Christian Posch performed the simulation analysis in Publications A and B.
- Verena Maier-Kiener performed the nanoindentation tests in Publication B.
- My supervisor Daniel Kiener is acknowledged for his expert guidance and contribution to all papers by providing basic ideas for publications along with helpful discussions and support during their preparation.

A. An SEM compatible plasma cell for in situ studies of hydrogen-material interaction

A. Massone [1,2], A. Manhard [3], W. Jacob [3], A. Drexler [1], W. Ecker [1], A. Hohenwarter [2], S. Wurster [4], D. Kiener [2]

1. Materials Center Leoben Forschungs GmbH, 8700 Leoben, Austria
2. Department Materials Science, Chair of Materials Physics, Montanuniversität Leoben, 8700 Leoben, Austria
3. Max-Planck-Institut für Plasmaphysik, Boltzmannstr. 2, D-85748 Garching, Germany
4. Erich Schmid Institute of Materials Science, 8700 Leoben, Austria

Abstract

An in situ hydrogen (H) plasma charging and in situ observation method was developed to continuously charge materials, while tensile testing them inside a scanning electron microscope (SEM). The present work will introduce and validate the setup and showcase an application allowing high-resolution observation of H-material interactions in a Ni-based alloy, Alloy 718. The effect of charging time and pre-straining was investigated. Fracture surface observation showed the expected ductile microvoid coalescence behavior in the uncharged samples, while the charged ones displayed brittle intergranular and quasi-cleavage failure. With the in situ images, it was possible to monitor the sample deformation and correlate the different crack propagation rates with the load-elongation curves. H-charging reduced the material ductility, while increasing pre-strain decreased hydrogen embrittlement susceptibility due to the possible suppression of mechanical twinning during the tensile test and, therefore, a reduction in H concentration at grain and twin boundaries. All the presented results demonstrated the validity of the method and the possibility of in situ continuously charging of materials with H without presenting any technical risk for the SEM.

A. 1. Introduction

Considering an increasing depletion of fossil fuels and the necessity to implement alternative sources of energy to mitigate the serious climate changes, hydrogen (H) is believed to be a promising future fuel for energy storage [1]. With this aim, materials have to be developed to transport and store H, and the most critical factor for safe use is a loss in ductility due to hydrogen embrittlement (HE). Nowadays, the use of high-strength structural materials for lightweight applications becomes a necessity. Although it is possible to develop materials with high tensile strength and high fracture toughness, many of them can be affected by H [2], leading to a severe degradation of their outstanding properties if exposed to H environments. Moreover, materials such as Ni-based superalloys, which are mainly used in the gas and oil industry, have to withstand extreme conditions avoiding stress corrosion and hydrogen embrittlement failure [3].

HE is a severe type of failure that affects a large number of metals and alloys. The first detrimental effects of H were reported in the 1870s Johnson [4]. He observed that the toughness of iron was reduced when immersed in acid and that this effect was reversible on a macroscopic point of view, concluding that H was responsible for this phenomenon. Since Johnson's first reports, many scientists have studied the nature, causes and control of H-related degradation of metals on a microscopic scale [5-18]. This has led to numerous controversial findings and interpretations on the HE mechanisms [5-7, 18].

There are two main approaches in literature to study the HE effects. One is focused on the analysis of post-mortem morphological features. From these studies, two mechanisms were proposed. The hydrogen enhanced decohesion mechanism (HEDE), first suggested by Gerberich and Oriani [5, 12], postulates that H diffuses to crack fronts, and the local accumulation of H reduces the cohesion between atoms. This reduction in cohesion in Ni and the effect of some co-segregation elements was recently studied by He et al. [19]. Thus, in the presence of H, the local maximum tensile stresses, controlled by the externally applied load and the crack front geometry, can exceed the maximum lattice cohesive force, giving rise to failure. Following this approach, Lynch proposed the adsorption induced dislocation emission (AIDE) mechanism [6, 20, 21], which states that H promotes dislocation emission from crack tips as a result of the weakening of interatomic bonds, implying that a greater proportion of dislocation activity results in faster crack growth.

The second approach for studying HE effects focuses on in-situ experiments. Robertson, Birnbaum and Sofronis [7, 22-24] proposed the hydrogen enhanced localized plasticity (HELP) mechanism based on in-situ environmental transmission electron microscopy (TEM) results. They suggested that H increases the rate of dislocation generation and velocity. Furthermore, H lowers the interaction between dislocations and elastic obstacles, leading to a reduction in shear stress for dislocation motion and promoting localized deformation.

One important aspect in the study of HE is the H source. From the charging point of view, H can either be pre-charged into the material or introduced *in-situ*. In the first case, considering that H exhibits fast diffusion in some materials [25], there is a significant probability that outgassing occurs. In-situ charging experiments prevent this issue by continuously supplying H. Among these, the most popular ones are performed either with H gas at high pressure [8] or by electrochemical cathodic charging [9, 10]. However, in these cases, a high-resolution observation during deformation is difficult. *In-situ* observation during H charging is limited by the difficulty of operating a H source in a high vacuum environment. Environmental SEM and TEM have been used to test H effects in an H environment with nanomechanical testing [26, 27], allowing an observation of the defect behaviour, but with a limited field of view and potential sample size effects [28].

A third charging possibility, rarely developed though, is plasma charging. Plasmas are generated by supplying energy to a neutral gas causing the formation of charge carriers. There are various ways to supply the necessary energy for plasma generation. The most commonly used method of generating and sustaining a low-temperature laboratory plasma is by applying an electric field to a neutral gas [29]. Any volume of neutral gas always contains a few electrons and ions and when the electric field is applied, these free charged particles are accelerated and collide with atoms and molecules in the gas, thereby creating new charged particles. Thus, an avalanche of charged particles is generated, which is eventually balanced by charge carrier losses to arrive at a steady-state plasma.

Wang et al. [30, 31] used low-pressure H plasma in an environmental SEM to study HE of a ferritic alloy with in-situ mechanical testing by connecting a plasma cleaner to the SEM chamber. Unfortunately, they found *in-situ* observation by normal SEM mode to be limited and were not able to perform *in-situ* imaging with high-voltage. The challenge in this case lies on the difficulty of having an *in-situ* observation in the H environment due to the high H flammability. Consequently, their investigations were only feasible when the chamber was again evacuated to the high-vacuum state after charging.

A. 2. Experimental method

To overcome these issues and establish more defined ways to study H-material interactions, a new *in-situ* H charging method with plasma charging has been developed to allow *in-situ* H charging inside an SEM while performing a macroscopic deformation test. Therefore, a miniaturized plasma cell using Radio Frequency (RF) power was built. This configuration consists of two electrodes confined in a vacuum vessel. One of the electrodes is grounded while the other one is powered by a high frequency (13.56 MHz) power source, and an exchangeable working gas is fed into the system through an inlet. In this study, deuterium gas was chosen so that in the future the retained H content can be determined by nuclear reaction analysis or by thermal desorption. Furthermore, a matchbox is necessary to match the impedances of the RF generator and the plasma to optimize power absorption [32].

Fig. 1-a shows a scheme of the *in-situ* setup in the SEM. A stainless steel cup of 25 mm diameter, 20 mm height and an aperture of 2 mm is used as the vessel and powered electrode, while the

grounded sample acts as counter electrode. Tensile specimens were fabricated by electrical discharge machining with the geometry of 32 mm length, 5 mm width and thicknesses ranging between 0.65 and 1.40 mm. Since the aperture of the powered vessel cup is 2 mm diameter, only the centre region of the samples was charged with H. This allows H charging of a localized region of the sample where the *in situ* observation will be performed. To provide a faster H diffusion through the thickness of the material, a reduction in the thickness to approximately 0.2 mm was made in the charged area (see Fig. 1-b). Furthermore, since the charging is conducted only from the bottom of the samples, a contamination free top surface for SEM observation is provided. An Indium wire gasket was used to seal the sample to the cell, and a Teflon disk with an aperture in the centre of the sample was used to attach the sample to the Indium seal. This arrangement keeps the cell not only sealed, but also allows a friction-less displacement of the sample during the mechanical test as well as the surface observation through the electron beam.

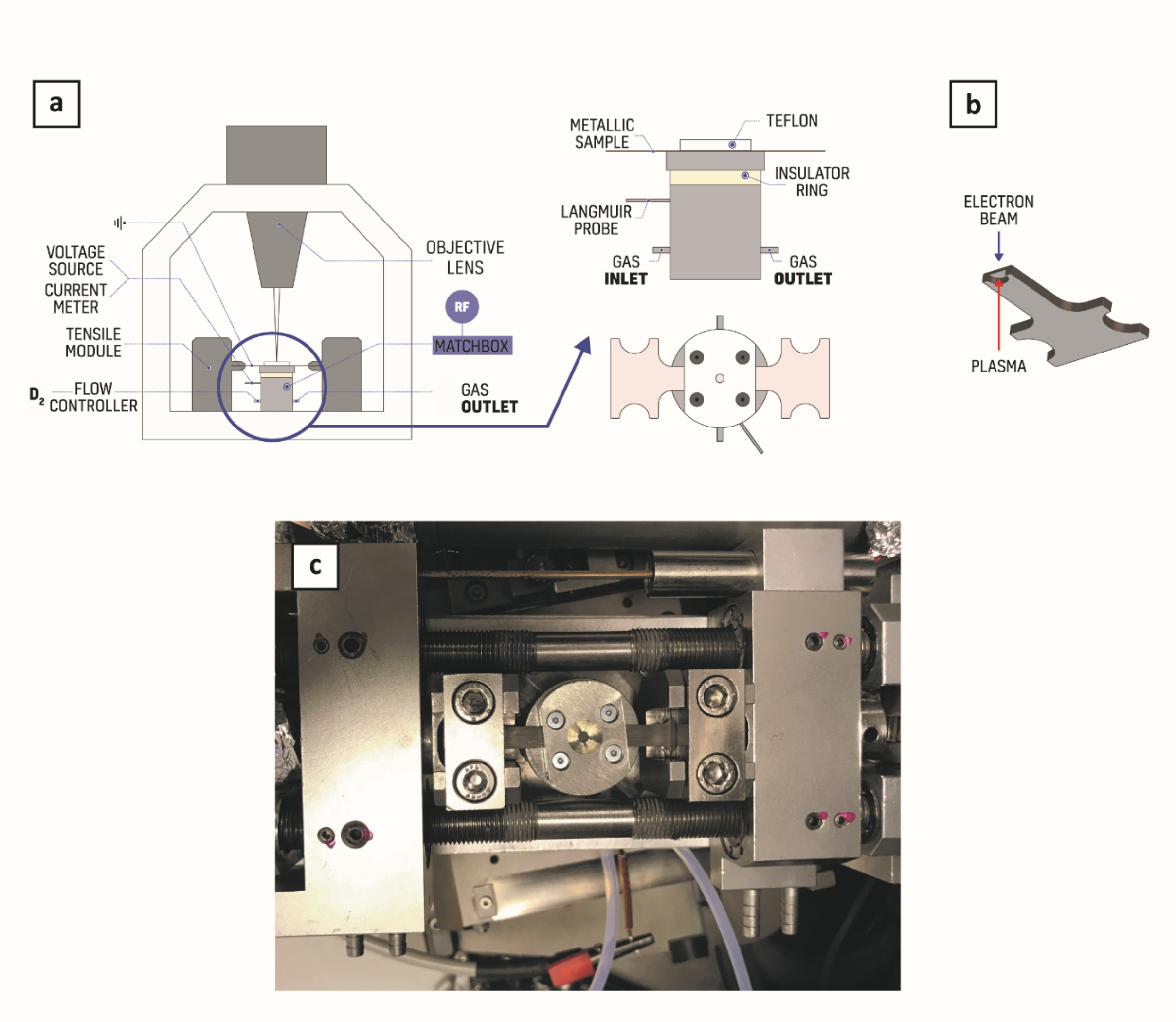

Figure 1. (a) Scheme of miniaturized plasma cell implemented in the SEM. (b) Cross section of tensile sample with indicated charging and observation directions. (c) Top view of the plasma device with the tensile stage inside the SEM

As the sample geometry deviates from standardized geometries, a fully three-dimensional mechanical finite element (FE) simulation was conducted to account for the heterogeneity of stress distribution across the thinned centre region of the samples, as shown in Fig. 2. The thickness of the centred region was 200 µm in the model. The FE modelling has been performed with the commercial software package Abaqus [33]. The sample geometry is meshed using tetrahedral continuum elements with quadratic shape functions. An average element size of 0.05 mm was used in the thinned area of the sample. In the rest of the model, the element size length was 0.2 mm. The applied material model describes the elasto-plastic behaviour of the solution-annealed Alloy 718 by means of a von Mises yield function with isotropic hardening. The hardening function is based on a data field approach considering the measured true stress-true strain dependency. The Young's modulus was assumed to be 210 GPa and the Poisson's ratio was 0.3.

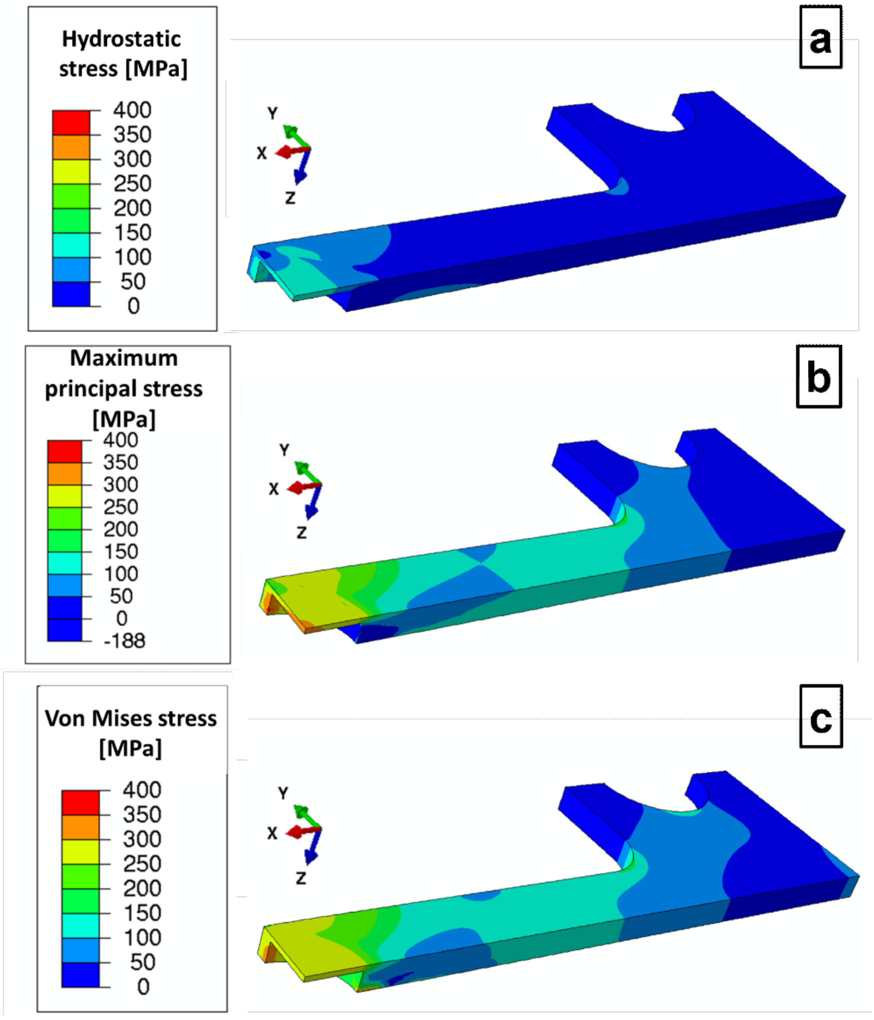

Figure 2. Stresses distribution in cross section of the sample. (a) Hydrostatic stress (MPa). (b) Maximum principal stress (MPa). (c) Von Mises stress (MPa). The pictures were taken for a plastic strain of 1% in the middle of the thinned area where the plasma charges the sample from below

The tests were performed in an SEM Stereoscan 440 operated at an acceleration voltage of 10 kV for imaging. A Kammrath & Weiss tensile stage, equipped with a 10 kN load cell and an inductive displacement sensor was used for the mechanical tests. The accuracy of the load cell is in the order of ~1 N, and the accuracy of the displacement sensor is ~0.5 µm. For all tests, a displacement rate of 0.2 µm/s was set. Teflon tubes were used for gas inlet and outlet inside the SEM chamber and the gas flow was controlled with a Bronkhorst Mass Flow Controller In-Flow. A CESAR RF power generator with an impedance matching box served to supply energy to the deuterium gas to produce plasma. For delivering the energy to the plasma cell, a 50 Ω coaxial cable was selected.

To investigate the plasma parameters, Langmuir probe measurements were conducted in a first prototype of the plasma cell built at the Max-Planck-Institut für Plasmaphysik, in Garching. The Langmuir probe consisted of a tungsten wire of 5 mm length and 0.15 mm diameter. The gas flow used was 0.75 sccm (standard cubic centimetres per minute) with power ranging from 0.8 to 1.4 W. The resulting DC bias voltage was 100 V. The current (I) drained by the probe for each bias voltage (U) supplied was measured as shown in Fig. 3.

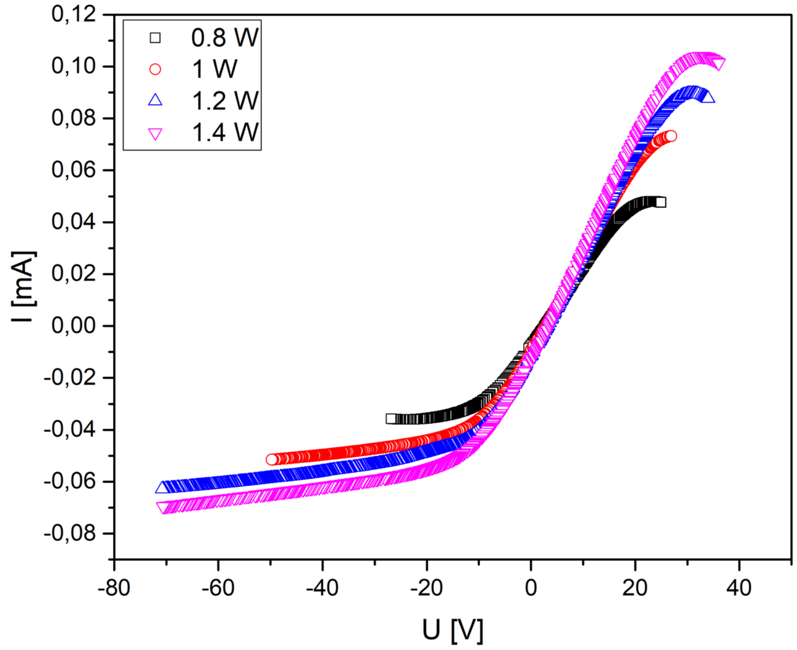

Figure 3. Langmuir Probe curves of the plasma cell prototype for a gas flow of 0.75 sccm and power ranging from 0.8 to 1.4 W. With these curves, electron temperature (~ 1 eV) and ion flux (~10^{20} m^{-2} s^{-1}) were calculated

The following equations [34, 35] were used to analyse the curves:

$$I = 0.61 n_e e S \sqrt{\frac{T_e}{m_i}\left(1 - exp\left(-\frac{e(\varphi_{fl}-U)}{T_e}\right)\right)} \quad (1)$$

$$n_e = 1.42 * \frac{Is\sqrt{m_i}}{S\sqrt{V_p - U}} \quad (2)$$

$$\eta = 3 * 0.61\sqrt{\frac{T_e}{m_i}} n_e \quad (3)$$

where n_e = electron density, e = elementary charge, S = probe surface = $l\pi d$, T_e = electron temperature, φ_{fl}= floating potential (I=0), U = probe potential, m_i = ion mass = 6 amu (D_3^+ ions), I_s = ion saturation current, V_p = plasma potential and η = ion flux.

The exponential part of the I-U curve (eq. 1), if plotted semi-logarithmically versus the probe potential U, should be a straight line and the slope of the curve is $1/T_e$. To determine the plasma potential, one method is to take the point where I_e starts to deviate from exponential growth, that is where I_e' (U) is maximum or I_e'' (U) is zero [36]. For a gas flow of 0.75 sccm and power between 0.8 and 1.4 W, the resulting electron densities (eq. 2) were in the range of 10^{16} m^{-3}, electron temperatures around 1 eV and ion fluxes (eq. 3) in the range of 10^{20} m^{-2} s^{-1}.

Material

To demonstrate the versatility of the design, a Ni-based alloy (Alloy 718) in the solution annealed condition, with a grain size of ~100-200 µm, was tested with this novel method. This material was chosen as a model material to be examined, since its microstructure and its susceptibility to H have been reported previously in literature [37-42], permitting comparison to the *in situ* data. The composition of the material is shown in Table I, in conformity to AMS specification.

Table I. *Chemical composition of Alloy 718 [wt. %]*

Ni (+Co)	**Cr**	**Fe**	**Nb (+Ta)**	**Mo**	**Ti**	**Al**	**Co**	**C**	**Mn**	**Si**	**P**	**S**	**B**	**Cu**
50-55	17-21	Balance	4.75-5.50	2.8-3.3	0.65-1.15	0.2-0.8	1 max	0.08 max	0.35 max	0.35 max	0.015 max	0.015 max	0.006 max	0.30 max

With the ion flux η calculated from the Langmuir Probe data and the H diffusion coefficient in Alloy 718 [43], H concentration can be calculated. Assuming D_3^+ ions at 100 V bias (i.e., 33 eV/D) and a pure Ni target for simplicity (the alloy has a similar stopping power); the mean implantation depth r_{mean} was calculated using a Monte-Carlo program, SDTrim.SP 6.0 [44]. The resulting r_{mean} is 1.15 nm. About 41% of the particles are implanted (the remaining 59% are reflected directly and do not contribute to the D concentration).

A simple analytical model [45] was assumed considering the case of diffusion-limited recombination at both sample surfaces. Since H solubility in Alloy 718 is low, solute H has a strong tendency to leave the sample once it reaches the surface. Assuming that recombination of H to H_2 (or D to D_2) is fast (reasonable for a clean surface exposed to plasma) the entire amount of H/D diffusing to the surface of the sample is immediately lost, i.e., the solute H/D concentration at the plasma-exposed surface is 0. Furthermore, the sample thickness (200 µm) is much larger than the implantation range (~1 nm) and any H/D that is implanted starts diffusing. In steady state, there is a constant H/D concentration gradient towards either surfaces, according to Fick's law:

$$j = -D_H * \frac{\partial \rho_H}{\partial x} \qquad (4)$$

where j = diffusion flux, D_H = H diffusion coefficient, ρ_H = H density.

The highest concentration is reached at the implantation range and it decays linearly towards either surface. Since the implanted surface is much closer to the implantation range than the opposite surface (which is observed by the SEM), this gradient is steeper and, accordingly, the diffusive flux towards this surface is larger. In good approximation, nearly all deuterium particles that are implanted diffuse back to the plasma-exposed surface and desorb there. Only a small fraction of the implanted flux (0.001 µm/200 µm= $5*10^{-6}$) diffuses into the bulk and, eventually, to the observed surface.

The following equation can be used to calculate the concentration maximum at the implantation range (the fraction of diffusion into the bulk can safely be neglected):

$$C_{max} = \frac{r_{mean} * (1-R) * \eta}{\rho * D_H} \qquad (5)$$

where C_{max}= maximum H/D concentration, R= reflection coefficient, η = ion flux, ρ= density, D_H= H diffusion coefficient.

This leads to a maximum H solute concentration between ~120-150 ppm. Since the decay towards the back surface is assumed linear, the average solute concentration would be exactly half of that, i.e. ~60-75 ppm.

Testing conditions

Two different batches of samples were tested with different charging conditions. The first set (samples S1 to S4 in Table II) was tested with different charging times, from uncharged conditions to 1 h of pre-charging. The pre-charged samples were also in-situ charged while testing, taking into account that the tests lasted approximately one hour. In the second set (S5 to S7 in Table II), the pre-straining effect was analysed. S5 was used as an uncharged and not pre-strained reference sample. S6 sample was pre-strained for 370 µm (pre yield point, which corresponds to approximately 7.7% strain in the centre of the sample) while S7 for 400 µm (post yield point, corresponding to 8.3% strain in the same region as sample S6). Both samples were held in the strained condition and were pre-charged with hydrogen for 4 h. Afterwards, the tensile test was continued until failure. All tests were conducted under constant strain rate conditions with a constant displacement rate of 0.2 µm/s.

Table II. *Overview of Alloy 718 samples tested*

Sample	Testing condition	Overall thickness (mm)	Reduced thickness (mm)	Failure time (min)
S1	Uncharged	0.65	0.20	72.58
S2	Charged while testing	0.65	0.23	67.5
S3	0.5 h pre-charged+ charged while testing	0.65	0.20	70.25
S4	1 h pre-charged+ charged while testing	0.65	0.23	69.3
S5	Uncharged	1.42	0.15	64.5
S6	Deformed below yield point+ 4 h pre-charged	1.41	0.19	55.4
S7	Deformed beyond yield point+ 4 h pre-charged	1.40	0.15	51.7

After the tensile tests, fracture surfaces of the failed samples were analysed ex-situ with an SEM LEO 1525 using an acceleration voltage of 20 kV.

A. 3. Results

Effect of pre-charging time

Fig. 4 shows the load-elongation curves of samples S1 to S4. The noise in the signal arises from interference between the RF power supply and the electronics of the tensile module, which could not be completely suppressed by shielding of the cables. At the beginning of the deformation experiment, the force value was not zero due to clamping and friction effects, which would also affect the apparent initial loading regime. Notably, for increasing deformations, the loading data converged for all samples and the maximum load value was approximately the same for all the tested samples, which is controlled by the failure of the uncharged thick side parts of the tensile sample (as shown in Fig. 1-c, only the centre-thinned area is charged). Importantly, all the charged specimens failed at lower elongations than the uncharged sample. Focusing only on the shaded areas, the elongation region from where cracks were initiated until final failure can be compared, i.e. the comparison of the crack propagation rather than initiation times. Comparing the shaded areas in the graph, it can be seen that the longer the charging time, the smaller the shaded area, i.e. the greater the decrease in the elongation of the samples.

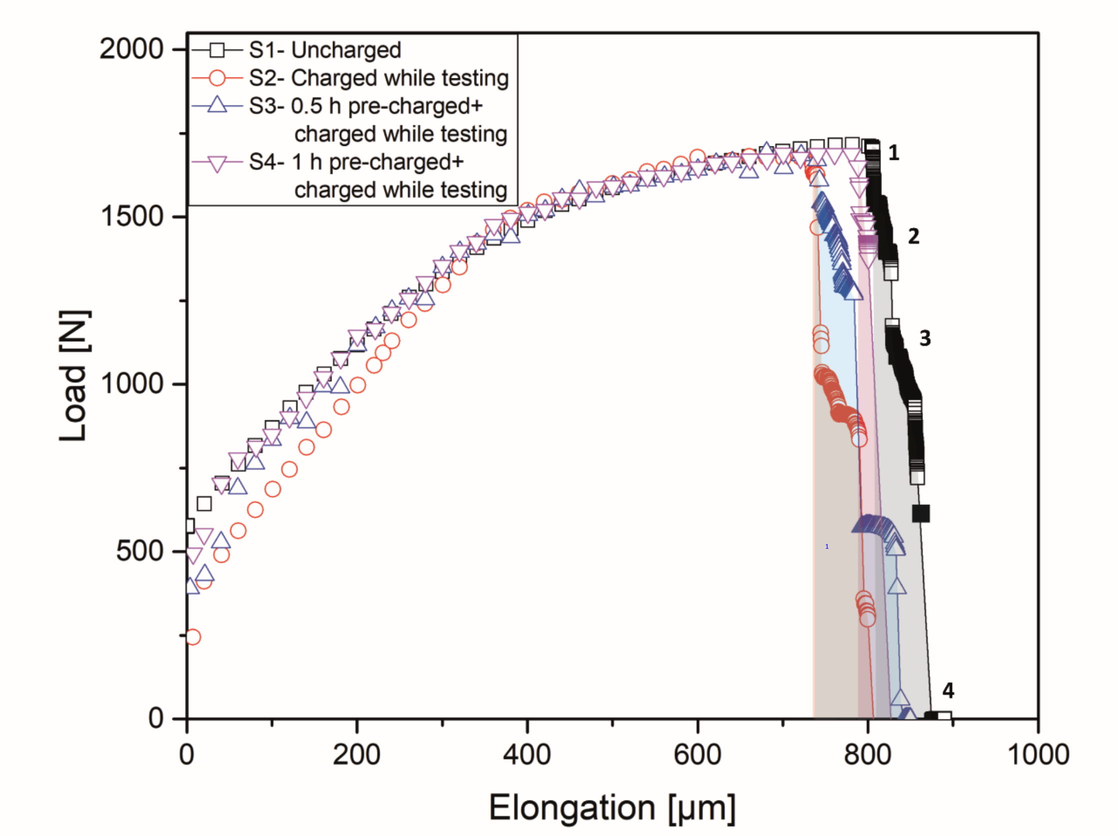

Figure 4. Load-elongation curves of Alloy 718 S1, S2, S3 and S4 samples. Points 1 to 4 in the curve of the uncharged sample S1 correspond to the points where in-situ images were taken. Charged samples S2, S3 and S4 failed at lower elongation than uncharged S1 sample. The shaded areas show that with increasing charging time, the loss of elongation was higher

Fig. 5 shows the *in-situ* images of the centre of sample S1. The first decrease of the load corresponds to the appearance of a crack, while the last image relates to the final failure of the sample.

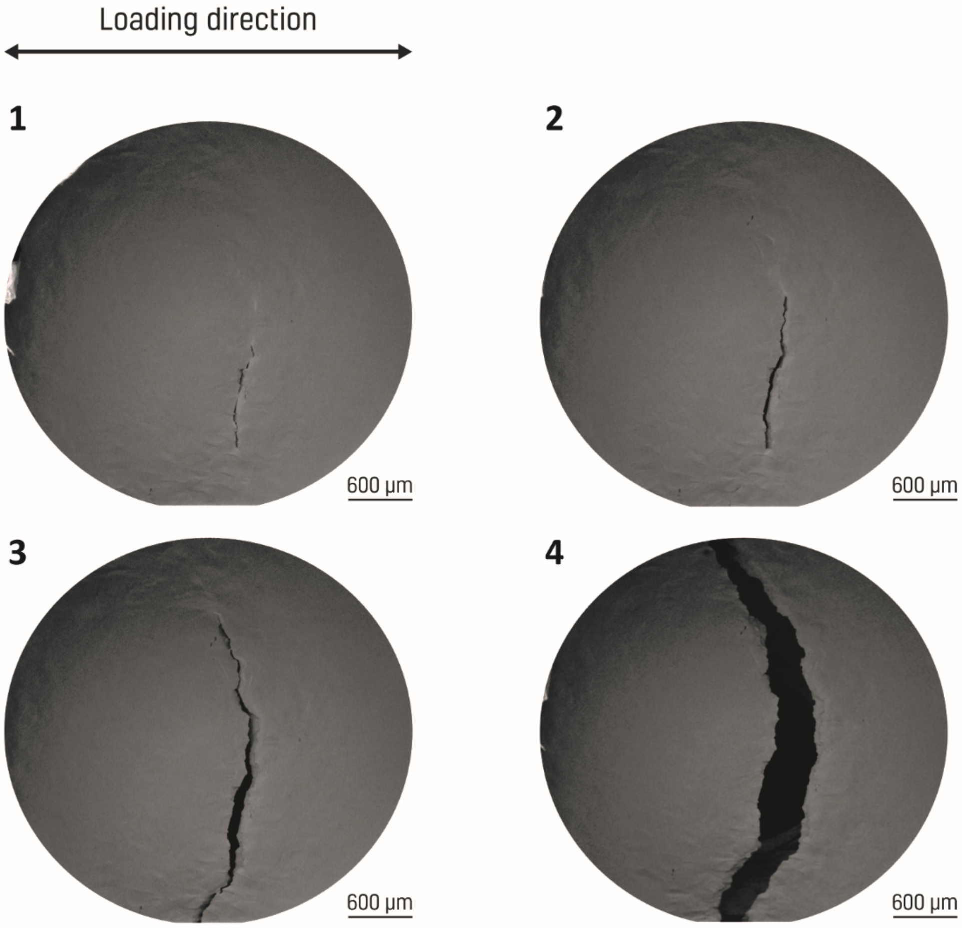

Figure 5. In-situ images of Alloy 718 S1 (uncharged) sample. Points 1 to 4 correspond to the points marked in the load-elongation curve in Fig. 4, where the crack propagation stages can be correlated with the different load and elongation values

From the *in-situ* images, crack propagation can be readily monitored, and the linear intercept crack length was estimated for each sample at different loading steps, as shown in Fig. 6. All the charged samples failed before the uncharged one, but for comparison purposes, the crack initiation times were normalized to 0 s. Comparing the slope of the curves, which correspond to the crack propagation rate, S4 shows the fastest crack propagation rate. In S3, the crack propagation rate was lower than in the uncharged sample. Nevertheless, when the crack reached the uncharged parts of the sample, the propagation rate decreased. In the load-elongation curve in Fig. 4, it can be seen that there is at first a rather steep decrease in the load. Afterwards, there is a stage with more or less constant value, which corresponds to deformation of the uncharged parts of the sample, proving that there was an effect on the sample. Contrary to this, in the uncharged specimen, the crack propagation rate did not decrease when reaching the “thicker” parts of the sample.

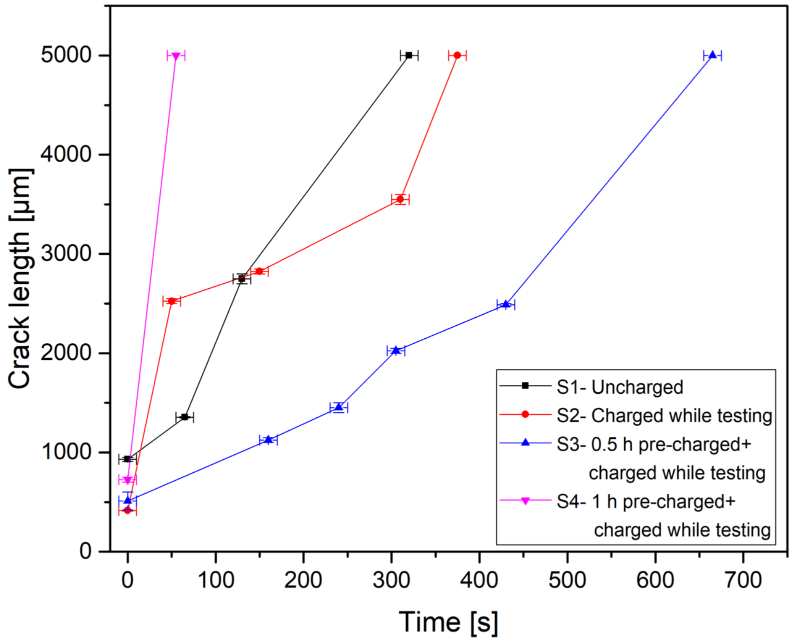

Figure 6. Crack length over time for Alloy 718 S1, S2, S3 and S4 samples with crack initiation times normalized to 0 s. Considering that the slope of the curves represents the crack propagation rate, S4 shows the fastest rate

Fig. 7 shows the post-mortem fracture surfaces of the samples. Since these images were taken with a field emission SEM, the resolution is better than the *in-situ* images of Fig. 5, where a tungsten filament SEM was used. Sample S1 (Fig. 7-a) exhibits a typical ductile fracture surface with larger primary dimples and smaller secondary ones. Fig. 7-b shows the fracture surface of S2, with a completely different character than the uncharged one. This sample exhibits a brittle failure by decohesion along grain boundaries with rather smooth facets. Samples S3 and S4 have several different morphologies, as can be seen in Fig. 7-c and d. There are regions of microvoid coalescence, flat “featureless” regions and regions with striations, the last marked with dashed boxes in the figure.

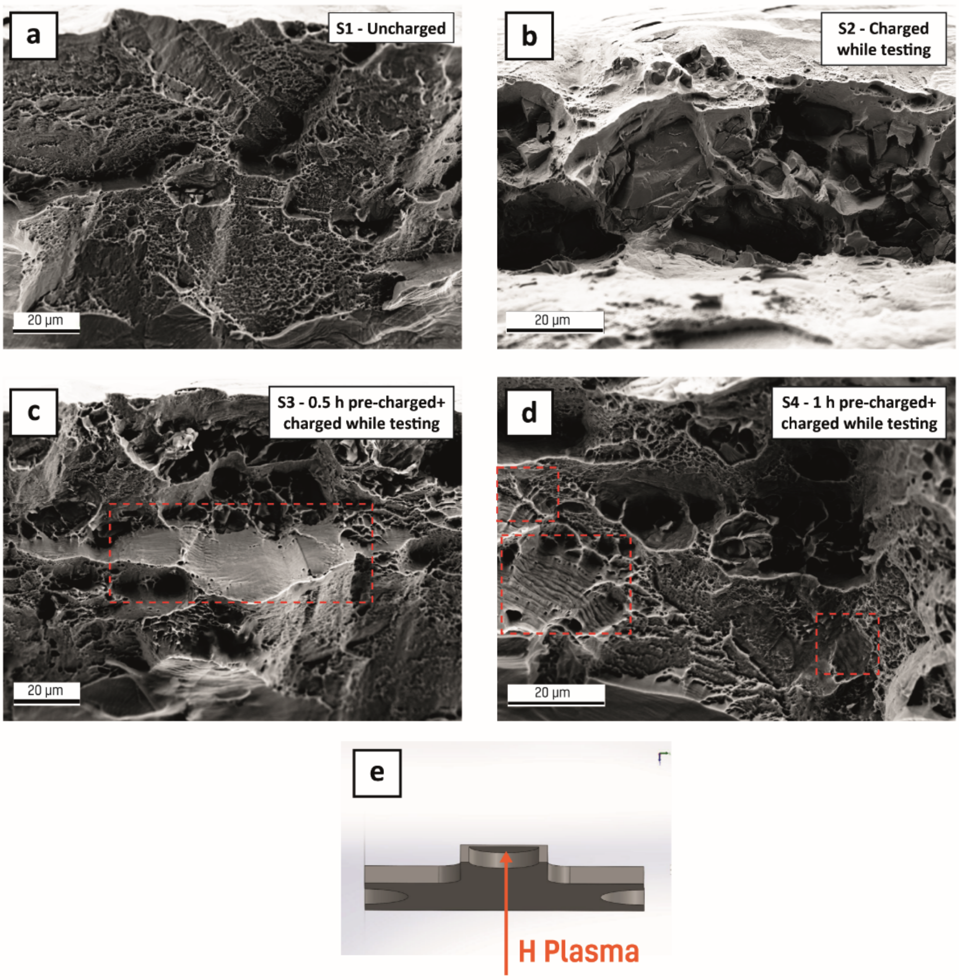

Figure 7. Fracture surfaces of (a) S1, (b) S2, (c) S3 and (d) S4 Alloy 718 samples. (e) View of the cross section of the samples with the direction of plasma charging indicated. S1 (uncharged) sample shows a ductile failure while the charged samples show either intergranular or regions of "quasi-cleavage" (marked with dashed boxes) fracture behaviour

Effect of pre-straining

Fig. 8 shows the load-elongation curves of the second set of samples, where different amounts of pre-strain were applied. Comparing the shaded areas of S5 and S6, it can be seen that, compared to the previous cases, the presence of H reduces the elongation until failure of the sample more significantly. From points 1 to 3 in S6, the crack propagates through the centre region of the sample, which is in contact with H, as it can be seen in the *in-situ* images in Fig. 9. On the other hand, S7 shows a different character. As soon as a crack is initiated, point 5, the propagation was retarded, maintaining an almost constant value of load, until point 6, followed by a decrease in the load to point 7 and another step of constant load before final failure. In this case, the shaded area of the deformed sample was larger than the one of the uncharged S5 sample, i.e. in S7 the crack propagation was retarded to a higher extent than samples S5 and S6.

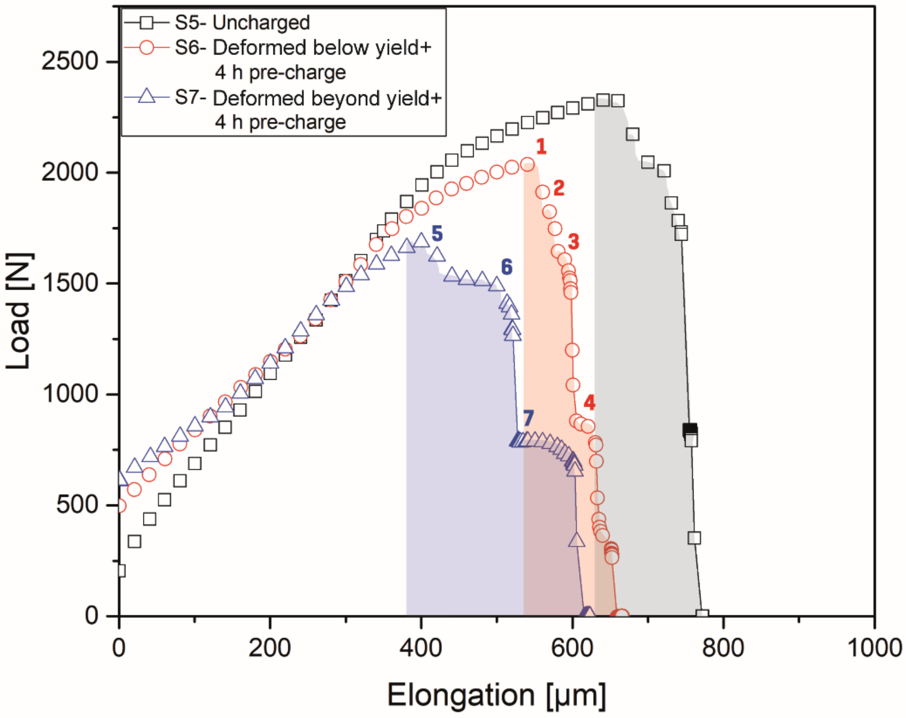

Figure 8. Load-elongation curves of Alloy 718 S5, S6 and S7 samples depicting influence of pre-strain. Points 1 to 4 in the S6 curve correspond to the points where in-situ images were taken and 5 to 7 in the S7 curve show the regions where there are plateau regions of the force. The shaded areas show a reduction in elongation in the S6 charged and pre-strained below yield-sample compared to the uncharged sample but an increase in the S7 charged and pre-strained above yield-sample.

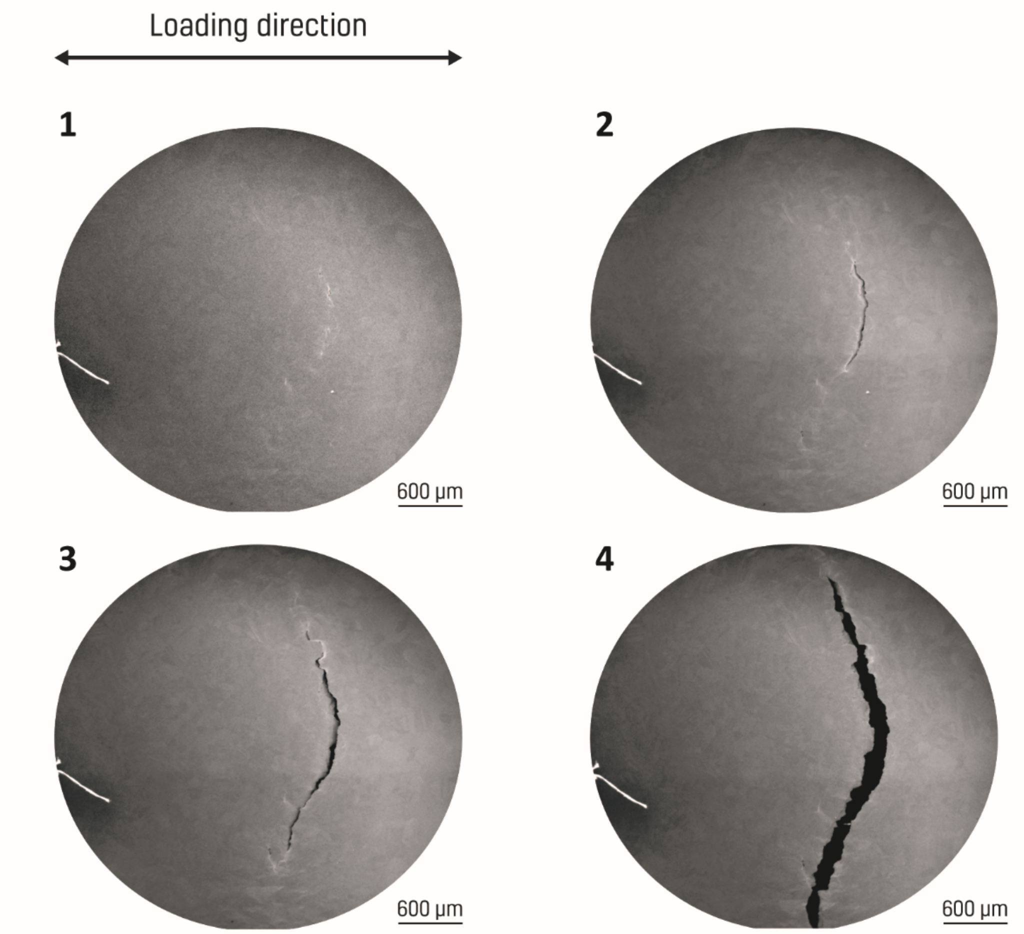

Figure 9. In-situ images of Alloy 718 S6 (pre-strained before yield and 4 h pre-charged) sample. Points 1 to 4 correspond to the points marked in the load-elongation curve in Fig. 8. Crack initiation and propagation steps can be correlated with load and elongation values of the curve

As in the previous experiments, the crack length over time was calculated from the *in-situ* images, displayed in Fig. 10. The uncharged sample, S5, is the last one to fail. Comparing the time from which cracks are initiated until final failure, it can be seen that the crack propagation rate of S6 is higher than S5. However, S7 shows a slower propagation than the uncharged S5 sample (990 s of crack propagation compared with 570 s for S5). This is in agreement with the load-elongation curves in Fig. 8.

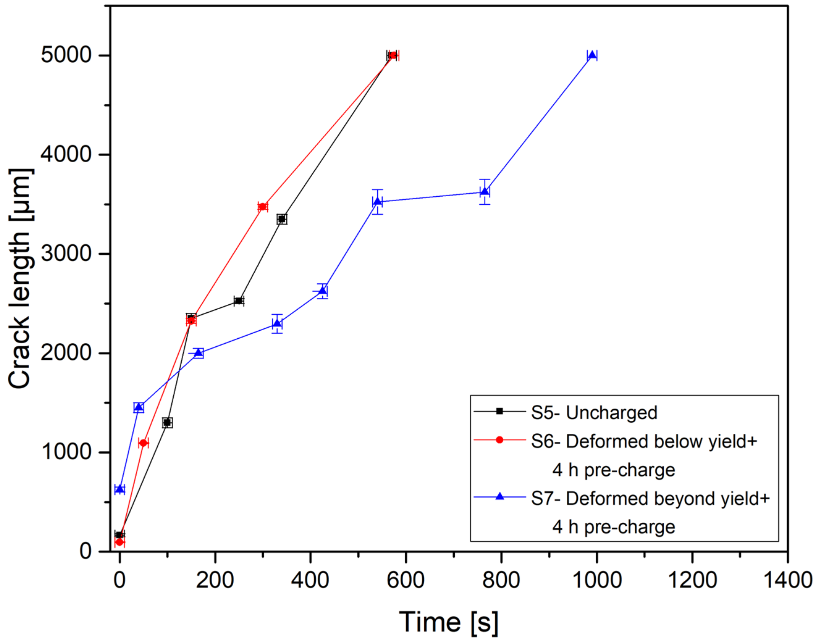

Figure 10. Crack length over time for Alloy 718 S5, S6 and S7 samples with crack initiation normalized to 0 s. The slope of the curves corresponds to the crack propagation rate. Samples S5 and S6 show a similar behaviour but the propagation rate in sample S7 was retarded

Fig. 11 shows the fracture surfaces of the samples. The sample S5 without pre-strain, Fig. 11-a, exhibits a typical ductile failure where small dimples within large ones can be seen, similar to the uncharged sample of the previous set of samples. The inclusions present on the fracture surface, marked with arrows, are most likely formed during the production process of the alloy [46]. This was the only sample in which inclusions were seen. The fracture surface of sample S6 exhibits some similarities with S3 and S4. This specimen also shows dimples and regions with river markings indicated by dashed boxes. On the other hand, S7 presents to a large extent only dimples.

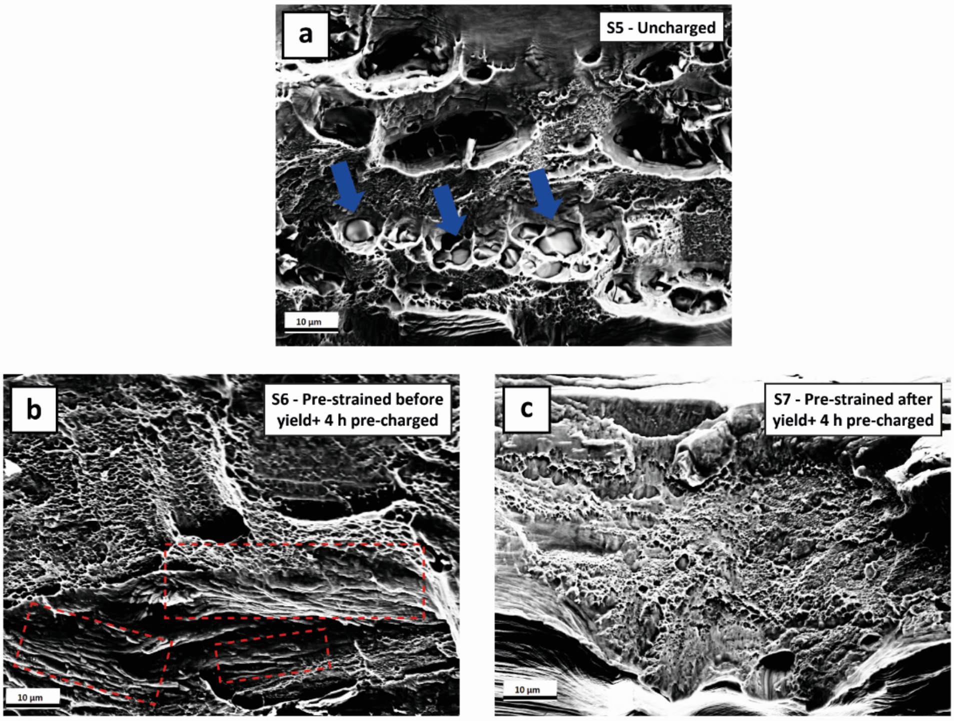

Figure 11. Fracture surface of (a) S5, (b) S6 and (c) S7 Alloy 718 samples. The charging for all samples is from the bottom as shown in Fig. 7-d. Inclusions were present in S5 sample, marked with arrows in (a). S5 and S7 show a ductile fracture while "quasi-cleavage" regions can be seen in S6 sample, marked with dashed boxes in (b)

Moreover, optical micrographs of the top surface were taken after sample failure next to the fracture surface, as shown in Fig. 12. Mechanical twinning can be observed in the samples in the proximity to the fracture surface.

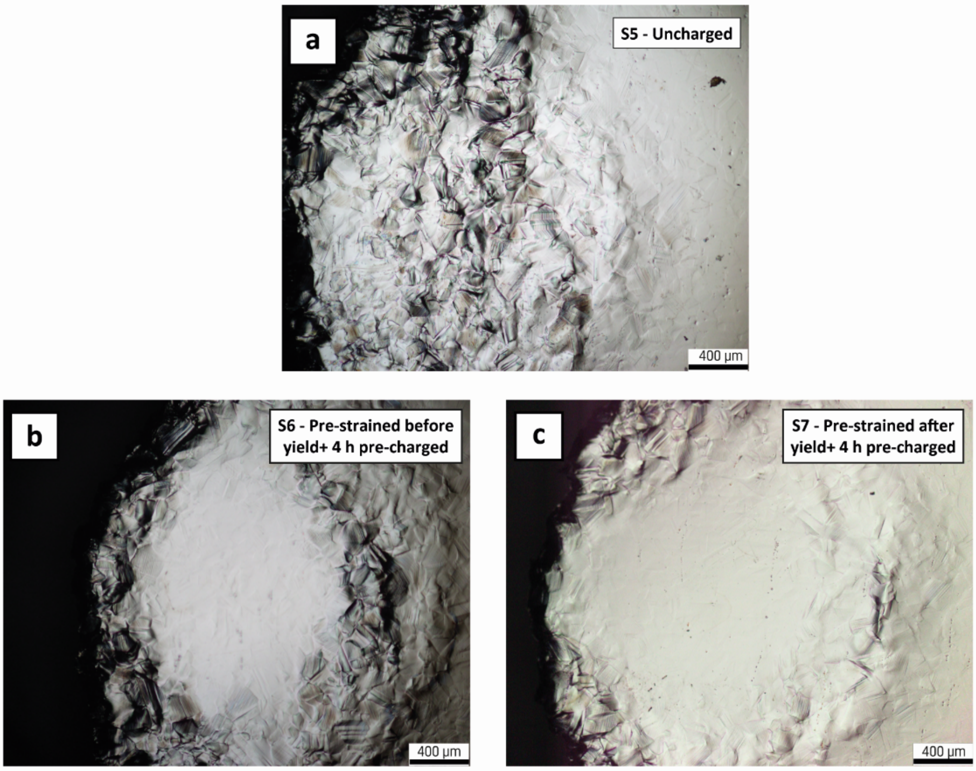

Figure 12. Optical micrographs of (a) S5, (b) S6 and (c) S7 Alloy 718 samples showing deformation and mechanical twinning next to the fracture surface

A. 4. Discussion

Method

The method developed allows direct charging of materials for the investigation of H effects for a wide range of sample sizes with the advantage of testing macroscopic samples. The simulation results in Fig. 2 confirmed that, although the geometry is not standardized, the stress distribution in the charged and thinned area is sufficiently homogenous, eliminating possible undesired stressed-driven H diffusion to regions with higher hydrostatic stresses in the sample.

An important advantage of this method is that samples can be continuously charged while testing, which is crucial for materials with high H diffusivity and simultaneously low H solubility, for example ferritic steels. Moreover, there is no risk of sample corrosion as can happen with electrochemical charging, with the possibility of sample failure. Furthermore, with cathodic charging there can be a pre-damage in the samples, which can alter the effect of H. For instance, it has been reported [47] that cathodic charging alone generated slip lines and surface and subsurface cracks. The pre-damage caused by the charging resulted finally in a reduction of yield strength and an increased embrittlement.

To the authors' knowledge, the presented method is the first one reported that combines *in-situ* charging and tensile testing inside an SEM, presenting no risk for the SEM even when the sample fractures.

Effect of pre-charging time

In the load-elongation curves from Fig. 4, the elongation of S4 seems to be larger than S2 and S3. Nevertheless, if only the elongation is considered from the point where cracks are initiated (first drop in the load) until the final fracture of the sample, it can be seen that with increasing charging time the elongation was decreased. In the S4 sample, the load dropped abruptly from point 1 to point 2 (zero load), while in S2 and S3 samples failure was not so abrupt. This behaviour was also evidenced in the *in-situ* images and the crack propagation in Fig. 6. For S4 only two *in-situ* images of the crack were recorded, since the failure of the sample occurred immediately after crack initiation. Furthermore, as mentioned before, the crack propagation rate of S4 was the highest. In this context, sample S4 showed a greater susceptibility to H due to the higher amount of pre-charged H. Contrary to this, although crack initiation of S2 and S3 was before S4, the propagation was slower, especially in the areas that were not in contact with the H source. A possible reason for this behaviour is that there is a gradient in H concentration, and since H diffusion in Ni is low [48, 49], there is not enough time for H to diffuse to the sides of the samples (which are not in direct contact with the plasma) so crack propagation is not accelerated in such areas, in contrast to the directly H-charged regions.

In ductile crack growth, there is almost no emission of dislocation directly from crack tips due to strong bonding. Most of the egressing dislocations, around crack tips, produce crack blunting and plastic deformation rather than crack advance. The coalescence of large voids involves nucleation and growth of small voids, and large dimples with smaller dimples appear on fracture surfaces [50], as it can be seen in Figs. 7-a and 11-a in the uncharged specimens.

The morphologies of H-enhanced fractures can be unaffected or changed from ductile microvoid coalescence to quasi-cleavage, cleavage or intergranular failure. In sample S2, the fracture behaviour, Fig. 7-b, was clearly affected by H changing to a brittle intergranular failure dominated by grain boundary decohesion.

Regarding the flat "featureless" regions and the regions with striations of samples S3 and S4, they are referred in literature as "quasi-cleavage" [51] and occur when both transgranular cleavage and ductile failure operate together. Materials that fail with a quasi-cleavage mechanism usually show river markings, which are originated inside the grains and run approximately parallel to the crack propagation direction. These markings can be seen in Figs. 7-c, d and 11-b running parallel to the crack propagation direction, i.e. perpendicular to the loading direction.

Lynch explained the presence of dimples in the charged samples with his Adsorption Induced Dislocation Emission (AIDE) model [2]. It states that dislocation emission in the presence of H is different from crack growth in an inert environment. Dislocations are emitted from the crack tip on suitable inclined slip planes as a result of interatomic bonds weakening by H. Consequently, a greater proportion of dislocation activity results in crack growth, the coalescence of cracks with voids occurs at lower strains (in accordance with the load-elongation curves in Fig. 4) and shallower dimples are produced on fracture surfaces.

Although the crack propagation rate is greater in S4, with the observation of fracture surfaces it seems that the S2 sample is more susceptible than S3 and S4. This behaviour can be explained considering the plasma conditions. Although all the samples were tested with the same bias voltage plasma, in the S2 sample the power supplied was 4 W compared to 7 W in the other two samples. This increase in power can increase the temperature of the sample, increasing the H diffusivity in the sample and thus decreasing the H concentration. Unfortunately, in the current realization it is not possible to measure (or actively control) the sample temperature during experiments, but this is planned to be implemented for future work.

Effect of pre-straining

According to the results presented, pre-straining the sample before yield (S6) shows similar H susceptibility as in the previous experiments. This specimen displayed similar effects as the charged samples in the previous set. The elongation was reduced and the crack propagation rate increased. Furthermore, the fracture surface exhibited a quasi-cleavage mode. Contrarily, it seems that pre-straining the sample to a post yield condition (S7) reduces the sensitivity for HE.

Ji. et al. [52] detected similar effect in 310S stainless steel and they suggested that pre-strain hinders the formation of fresh mechanical twins and H delivery to twin boundaries, avoiding a high H concentration in twin boundaries. Since S7 exhibits lower susceptibility to detrimental H effects, it is possible that the H concentration was lowered at twin and grain boundaries. High-resolution SEM was used to compare the density of mechanical twins between the samples but no clear difference was observed. Another explanation for the behaviour of S7 could be that there is a strain hardening effect in the uncharged sides of the sample that lowers the crack propagation rate, giving rise to steps of constant load, as shown in Fig. 8.

A. 5. Conclusions and outlook

A novel *in-situ* method for HE studies has been developed and successfully implemented. This methodology is based on *in-situ* continuously charging materials with H plasma inside an SEM and allows having high-resolution observation while deforming the material of interest. In addition, although H outgassing from the material cannot be avoided (H arriving at the surface recombines and desorbs), there is a constant supply of H, which leads to a dynamic equilibrium of the H concentration. It is worth mentioning that the standard tungsten filament SEM used for this work only provides limited resolution of *in-situ* images, which could be highly improved by transferring the setup to a new field emission gun SEM. Nevertheless, in the present proof-of-principle case, the observations were sufficient to monitor the sample deformation and crack propagation and correlate them with the load-elongation curves.

With respect to the studied solution annealed Alloy 718 material, in all the charged samples, with the exception of S7 sample, the crack propagation rate was increased and the ductility decreased when H was present. Furthermore, with the *in-situ* images it was possible to detect that the crack propagation rates were decreased once the crack run into the regions that were not in contact with plasma, which were the last parts of the sample to fail.

Fracture surface observation of uncharged samples showed a typical ductile fracture with the presence of dimples. The charged samples, on the other hand, displayed either a brittle intergranular failure or a quasi-cleavage with river markings features. This difference could be attributed to a change in the sample temperature when applying more power to strike the plasma.

Future efforts will relate to modify the sample to introduce cracks in order to allow detailed crack microstructure interaction observations at higher magnifications, as well as detailed determination of the H concentration in the material.

Acknowledgments

The authors gratefully acknowledge the financial support under the scope of the COMET program within the K2 Center “Integrated Computational Material, Process and Product Engineering (IC-MPPE)” (Project No 859480). This program is supported by the Austrian Federal Ministries for Transport, Innovation and Technology (BMVIT) and for Digital and Economic Affairs (BMDW), represented by the Austrian research funding association (FFG), and the federal states of Styria, Upper Austria and Tyrol.

A. 6. References

[1] Johnston B., Mayo M. C. Khare A. “Hydrogen: The energy source for the 21st century”. Technovation. 25(6): 569-585 (2005).

[2] Lynch S. P. “Hydrogen embrittlement phenomena and mechanisms”. In: Vaja R.S., Shoji T. (Ed.) Stress Corrosion Cracking. Woodhead Publishing, Cambridge, pp 90-130 (2011).

[3] de Barbadillo J. J., Mannan S. K. “Alloy 718 for oilfield applications”. JOM. 64(2): 265-270 (2012).

[4] Johnson W. “On some remarkable changes produced in iron and steel by the action of hydrogen and acids”. Nature 11: 393 (1875).

[5] Gerberich W. W., Oriani R., Lii M.-J., Chen T., Foecke T. “The necessity of both plasticity and brittleness in the fracture thresholds of iron”. Philos. Mag. A 63:1363 (1991).

[6] Lynch S. P. “Environmentally assisted cracking: Overview of evidence for an adsorption-induced localised slip process”. Acta Metall. 36(10): 2639-2661 (1988).

[7] Birnbaum H. K., Sofronis P. “Hydrogen-enhanced localized plasticity- a mechanism for hydrogen-related fracture”. Mater. Sci. Eng. A176: 191-202 (1994).

[8] Vehoff H., Neumann P. “Crack propagation and cleavage initiation in Fe-2.6%-Si single crystals under controlled plastic crack tip opening rate in various gaseous environments”. Acta Metall. 28(3): 265-272 (1980).

[9] Barnoush A., Vehoff H. “Hydrogen embrittlement of aluminum in aqueous environments examined by in situ electrochemical nanoindentation”. Scripta Mater. 58(9): 747-750 (2008).

[10] Barnoush A., Vehoff H. “Recent developments in the study of hydrogen embrittlement: Hydrogen effect on dislocation nucleation”. Acta Mater. 58(16): 5274-5285 (2010).

[11] Beachem C. D. “A new model for hydrogen-assisted cracking (Hydrogen “Embrittlement”)”. Metall. Mater. Trans. B. 3(2): 441-455 (1972).

[12] Oriani O. A., Josephic P. H. “Equilibrium aspects of hydrogen-induced cracking in steels”. Acta Metall. 22(9): 1065-1074 (1974).

[13] Tabata T., Birnbaum H. K. “Direct observations of the effect of hydrogen on the behaviour of dislocations in iron”. Scripta Metall. 17: 947- 950 (1983).

[14] Robertston I. M., Birnbaum H. K. “An HVEM study of hydrogen effects on the deformation and fracture of nickel”. Acta Metall. 34: 353- 366 (1986).

[15] Matsui M., Kimura H. “The effect of hydrogen on the mechanical properties of high purity iron”. Mater. Sci. Eng. 40: 207-216 (1979).

[16] Nagumo M., Nakamura M., Takai K. “Hydrogen thermal desorption relevant to delayed-fracture susceptibility of high-strength steels”. Metall. Mater. Trans. A. 32A: 339-347 (2001).

[17] Lynch S. P. “Mechanisms of hydrogen-assisted cracking”. Met. Forum. 2: 189-200 (1979).

[18] Nagumo M., Yagi T., Saitoh H. “Deformation-induced defects controlling fracture toughness of steel revealed by tritium desorption behaviours”. Acta Mater. 48: 943-951 (2000).

[19] He S., Ecker W., Pippan R., Razumovskiy V. I. “Hydrogen-enhanced decohesion mechanism of the special Σ5(0 1 2)[1 0 0] grain boundary in Ni with Mo and C solutes”. Comput. Mater. Sci. 167: 100-110 (2019).

[20] Lynch S. P. “Metallographic contributions to understanding mechanisms of environmentally assisted cracking”. Metallography. 23: 141-171 (1989).

[21] Lynch S. P. “Comments on “A unified model of environmental assisted cracking”. Scripta Mater. 61: 331-334 (2009).

[22] Birnbaum H. K., Robertson I. M., Sofronis P. “Hydrogen effects on plasticity”. In: Kubin L., Hirth K. P. (Eds.) Disocations in Solids. Elsevier, Amsterdam, pp. 249-293 (2009).

[23] Birnbaum H. K. “Mechanisms of hydrogen related fracture of metals”. In: Moody N. R., Thompson A. W. (Eds.) Hydrogen effects on material behaviour: The Minerals, Metals and Materials Society. pp. 639-658 (1990).

[24] Birnbaum H. K., Robertston I. M., Sofronis P., Teter D. In: Magnin T. (Ed.) Corr.-def. interact. Trans Tech, Great Britain, pp 172-195 (1997).

[25] Bhadeshia H. K. “Prevention of hydrogen embrittlement in steels”. ISIJ Int. 56: 24-36 (2016).

[26] Robertson I. M., Sofronis P., Nagao A., Martin M. L., Wang S., Gross D. W. “Hydrogen embrittlement understood”. Metall. Mater. Trans. B. 46: 1085-1103 (2015).

[27] Barnoush A., Vehoff H. “In situ electrochemical nanoindentation: a technique for local examination of hydrogen embrittlement”. Corr. Sci. 50: 259-267 (2008).

[28] Pippan R., Wurster S., Kiener D. “Fracture mechanics of micro samples: Fundamental considerations”. Materials and Design. 159: 252-267 (2018).

[29] Conrads H., Schmidt M. “Plasma generation and plasma sources”. Plasma Sources Sci. Technol. 9: 441-454 (2000).

[30] Wan D., Deng Y., Barnoush A. “Hydrogen embrittlement effect observed by in-situ hydrogen plasma charging on a ferritic alloy”. Scripta Mater. 151: 24-27 (2018).

[31] Wan D., Deng Y., Hammer Meling J. I., Alvaro A., Barnoush A. “Hydrogen-enhanced fatigue crack growth in a single-edge notched tensile specimen under in-situ hydrogen charging inside an environmental scanning electron microscope”. Acta Mater. 170: 87-99 (2019).

[32] Vaghela N. “RF (13.56 MHz) Impedance Matching”. Huettinger Electronic Inc. http://www.if.ufrgs.br/~ckrug/pvd/rf-1.pdf. Accessed 3 September 2019.

[33] Abaqus Unified FEA-SIMULIATM by Dessault Systèmes®, (n.d.). https://www.3ds.com/products-services/simulia/products/abaqus/ (accessed December 5, 2019)

[34] Stroth U. Plasmaphysik-Phänomene, Grundlagen und Anwendung. Springer Spektrum, Garching, Germany (2011).

[35] Magnus F., Gudmundsson J. T. “Digital smoothing of the Langmuir probe I-V characteristic”. Rev. Sci. Instrum. 79, 073503 (2008).

[36] Chen F. F. “Lecture notes on Langmuir Probe Diagnostics”. In Mini-Course on Plasma Diagnostics, IEEE-ICOPS meeting, Jeju, Korea (2003).

[37] Liu L., Zhai C., Lu C., Ding W., Hirose A., Kobayashi K. F. “Study of the effect of δ phase on hydrogen embrittlement of Inconel 718 by notch tensile tests”. Corr. Science. 47: 355-367 (2005).

[38] Tarzimoghadam Z., Ponge D., Klöwer J., Raabe D. “Hydrogen-assisted failure in Ni-based superalloy 718 studied under in situ hydrogen charging: The role of localized deformation in crack propagation”. Acta Mater. 128: 365-374 (2017).

[39] Zhang Z., Obasi G., Morana R., Preuss M. “Hydrogen assisted crack initiation and propagation in a nickel-based superalloy”. Acta Mater. 113: 272-283 (2016).

[40] Zhang Z., Obasi G., Morana R., Preuss M. “In-situ observation of hydrogen induced crack initiation in a nickel-based superalloy”. Scripta Mat. 140: 40-44 (2017).

[41] Drexler A., Oberwinkler B., Primig S., Turk C., Povoden- Karadeniz E., Heinemann A., Ecker W., Stockinger M. “Experimental and nummerical investigations of the γ” and γ’ precipitation kinetics in Alloy 718”. Mater. Sci. Eng. A. 723: 314-323 (2018).

[42] Drexler A., Fischersworring-Bunk A., Oberwinler B., Ecker W., Gänser H.-P. “A microstructural based creep model applied to alloy 718”. Int. J. Plast. 105: 62-73 (2018).

[43] Jebaraj J. J. M., Morrison D. J., Suni I. I. “Hydrogen diffusion coefficient through Inconel 718 in different metallurgical conditions”. Corr. Sci. 80: 517-522 (2014).

[44] Mutzke, A., Schneider, R., Eckstein, W., Dohmen, R.; Schmid, K., von Toussaint, U., Badelow, G. (2019) “SDTrimSP Version 6.00” (IPP 2019-2). Garching: Max-Planck-Institut für Plasmaphysik.

[45] Tanabe T., Furuyama Y., Imoto S. “Hydrogen ion permeation through metals”. J. Nulc. Mater. 145-147: 305-308 (1987).

[46] Mitchell A. “Superalloys 718, 625 and various derivatives”. In: Loria E. A. (Ed.) The Minerals, Metals & Materials Society. pp 15-27 (1991).

[47] Lu X., Wang D., Wan D., Zhang Z. B., Kheradmand N., Barnoush A. “Effect of electrochemical charging on the hydrogen embrittlement susceptibility of alloy 718”. Acta Mater. 179: 32-48 (2019).

[48] Birnbaum H. K., Wert C. A. “Diffusion of hydrogen in metals”. Ber. Bunsen-Ges. 72(8): 806-816 (1972).

[49] Drexler A., Depover T., Verbeken K., Ecker W. “Model-based interpretation of thermal desorption spectra of Fe-C-Ti alloys”. J. Alloys Compd. 789: 647-657 (2019).

[50] Lynch S. “Mechanistic and fractographic aspects of stress corrosion cracking”. Corros. Rev. 30: 105-123 (2012).

[51] Martin M. L., Fenske J. A., Liu G. S., Sofronis P., Robertson I. M. “On the formation and nature of quasi-cleavage fracture surfaces in hydrogen embrittled steels”. Acta Mater. 59(4): 1601-1606 (2011).

[52] Ji H., Park I-J., Lee S.-M., Lee Y.-K. “The effect of pre-strain on hydrogen embrittlement in 310S stainless steel”. J. Alloys Compds. 598: 205-212 (2015).

B. Addressing H-material interaction in fast diffusion materials- A feasibility study on a complex phase steel

A. Massone [1,2], A. Manhard [3], W. Jacob [3], A. Drexler [4], C. Posch [1], W. Ecker [1], V. Maier-Kiener [5], D. Kiener [2]

1. Materials Center Leoben Forschungs GmbH, 8700 Leoben, Austria
2. Department Materials Science, Chair of Materials Physics, Montanuniversität Leoben, 8700 Leoben, Austria
3. Max-Planck-Institut für Plasmaphysik, Boltzmannstr. 2, D-85748 Garching, Germany
4. Institut für Werkstoffkunde, Fügetechnik und Umformtechnik, Technische Universität Graz, Rechbauerstrasse 12, 8010 Graz, Austria
5. Department Materials Science, Chair of Physically Metallurgy and Metallic Materials, Montanuniversität Leoben, Roseggerstrasse 12/Max-Tendler-Strasse 9, 8700 Leoben, Austria

Abstract

Hydrogen embrittlement (HE) is one of the main limitations in the use of advanced high-strength steels in the automotive industry. To have a better understanding of the interaction between hydrogen (H) and a complex phase steel, an in-situ method with plasma charging was applied in order to provide continuous H supply during mechanical testing in order to avoid H outgassing. For such fast-H diffusion materials, only direct observation during in-situ charging allows for addressing H effects on materials. Different plasma charging conditions were analysed, yet there was not a pronounced effect on the mechanical properties. The H concentration was calculated while using a simple analytical model as well as a simulation approach, resulting in consistent low H values, below the critical concentration to produce embrittlement. However, the dimple size decreased in the presence of H and, with increasing charging time, the crack propagation rate increased. The rate dependence of flow properties of the material was also investigated, proving that the material has no strain rate sensitivity, which confirmed that the crack propagation rate increased due to H effects. Even though the H concentration was low in the experiments that are presented here, different technological alternatives can be implemented in order to increase the maximum solute concentration.

B. 1. Introduction

One of the main goals in the automotive industry is the reduction of weight while maintaining an adequate strength and toughness, at low cost, and enhancing both safety and fuel economy. In this scenario, advanced high-strength steels (AHSS) are excellent candidates for this application, since they combine both high strength and low weight [1,2]. The most important ones are dual phase (DP), ferritic-bainitic (FB), martensitic, transformation-induced plasticity (TRIP), and complex phase (CP) steels. DP steels consist of martensitic islands in a ferritic matrix and they combine low yield strength combined with high ultimate tensile strength. FB steels have a microstructure of fine ferrite and bainite and strengthening is obtained by both grain refinement and second phase hardening with bainite. Martensitic steels show the highest tensile strength level and they are often subjected to post-quench tempering in order to improve ductility. TRIP steels exhibit superior strength and good formability as a result of the transformation of metastable retained austenite to martensite during deformation. The microstructure of CP steels contains small amounts of martensite, retained austenite, and pearlite within a ferrite/bainite matrix. An extreme grain refinement is created in this material by retarded recrystallization or precipitation of microalloying elements, such as Ti or Nb [3].

Despite their remarkably good mechanical properties, AHSS are susceptible to hydrogen embrittlement (HE), and this can lead to a loss of ductility. When AHSS are electroplated with a sacrificial metal, typically Zn, H can be absorbed during the coating deposition, as the process is not 100% efficient. Moreover, if the sacrificial coating corrodes in service, the exposed areas of the steel substrate will act as cathodic sites and H can be absorbed into the material [4]. H can also be introduced into the material during the painting process of a body in white structure. Lovicu et al. [5] measured the H content absorbed during the production process of autobody components, in which cathodic reactions in water solution take place in the phosphatizing and electrophoresis stages of the painting process. During these reactions, atomic H can form on the steel surface and diffuse into the material. The absorbed H during the painting process was lower than about 0.4 wppm. In this context, H is one of the main limitations in the use of AHSS, since it can reduce the ultimate tensile strength, ductility, fatigue strength, and/or fracture toughness of the steels [6]. This degradation becomes apparent when the material is under residual or applied tensile stresses. Absorbed H diffuses through the metal facilitating crack propagation and, the higher the stress level of the material, the more susceptible it is to undergo detrimental HE effects [7].

The mechanism of HE has been under discussion for many years, leading to different interpretations and controversial findings [8–16]. Nevertheless, it is accepted that HE can only occur for a critical combination of local stress and local H concentration [6,17–19]. This critical value for H concentration may depend on applied stress, microstructure, trapping state, and tensile strength level, among others. Moreover, it is believed that there is a saturation level above which there is a minimal change in HE susceptibility [17]. Drexler et al. confirmed that this is the case for AHSS [18,19].

High-strength materials are more prone to HE due to an increased number of potential fracture initiation sites, with martensite usually being the most susceptible steel phase [7]. The morphology of H-assisted fracture in AHSS depends on the steel microstructure and H concentration and it can be either unaffected or changed from ductile microvoid coalescence to quasi-cleavage, cleavage, or intergranular failure [17–20].

The effect of H on high-strength steels has been widely studied [5,6,18–35], but there are few studies regarding the interaction between H and CP steels. Malitckii et al. [32] investigated the role of retained austenite in CP steel and proposed that fatigue intergranular areas might be formed due to H accumulation at the austenite/martensite interfaces, followed by H-induced decohesion. Loidl et al. studied the effect of H on a CP1200, among other different AHSS. They showed that the degree of embrittlement was similar to martensitic steels and that TRIP steels presented the highest tendency to HE [33]. Lovicu et al. [5] concluded that martensitic microstructures exhibit great susceptibility to HE and, the higher the tensile strength, the lower the critical H concentration to produce damage in the material. Duprez et al. [29] studied the effect of H on a DP steel, a TRIP steel, a FB steel, and a ferrite-cementite grade. They demonstrated that the ductility of all the samples was reduced after electrochemical charging, with TRIP and DP steels the most susceptible ones. Nevertheless, after discharging the samples for one week, a large part of the ductility was recovered. This proved that the damage was caused by the intrinsic presence of H and not by an irreversible damage mechanism. Rehrl et al. [34] investigated the effect of different loading rates in four grades of AHSS and showed that, at high strain rates, there was no effect of H on the mechanical properties. Only with slow strain rate testing, the elongation at failure was reduced. This was explained when considering that at a high strain rate, the H diffusion is too slow to reach highly stressed microstructure regions. Drexler et al. studied the local H accumulation and its effect on HE for cold formed, punched, and heat treated CP1200 and DP1200 [18–20].

In all of the studies mentioned above, the investigations were made either with ex-situ H charging or without in-situ observation. These two approaches can lead to a misinterpretation of the results. When the materials are ex-situ charged, there is a risk of H outgassing before the test is performed, especially in some steels where H diffusion is very fast [35]. Without in-situ observation, the H effect can only be analysed post-mortem and not during the test. Even though the effect on mechanical properties can be determined, details on crack dynamics cannot be investigated without an in-situ approach. In order to overcome these limitations, several studies have already been made with in-situ charging [36–40] and, in the present work, the interaction between H and a CP steel was investigated by implementing an in-situ method, which allows for in-situ H charging during a tensile test inside a scanning electron microscope (SEM).

B.2. Materials and methods

2. 1. Material

A CP1200 steel was investigated in this work. The main microstructural phases are martensite, tempered martensite, and bainite, with a small content (<2%) of retained austenite. Table 1 shows the chemical composition of the material.

Table 1: *Chemical composition of the investigated industrial steel grade.*

	C	Mn	Si	Cr	S	Nb	Ti	Al
wt %	<0.20	<2.6	<0.8	<1.00	<0.010	<0.05	<0.15	0.015-1.0

The microstructure analysis was conducted on a field emission SEM Zeiss LEO 1525 (Carl Zeiss GmbH, Oberkochen, Germany) while using an acceleration voltage of 20 kV and by EBSD using a pixel size of 59 nm and a working distance of 15.7 mm. Figure 1 depicts the microstructure of the material. Figure 1a exhibits the secondary electron image and Figure 1b shows the inverse pole figure map in the normal direction of the same region. The average prior austenite grain size was measured to be ~3 µm.

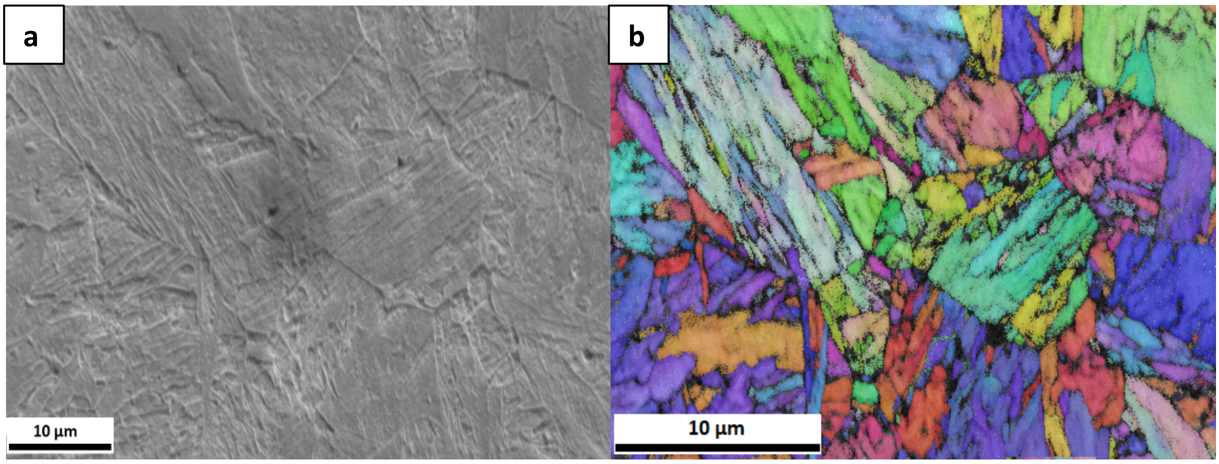

Figure 1. (a) Secondary electron image and (b) inverse pole figure in the normal direction of the investigated CP1200 microstructure

The as-delivered material had a thickness of 1.2 mm and tensile samples with the geometry of 32 mm length, 5 mm width, and 0.5–1.10 mm thickness were fabricated by electrical discharge machining parallel to the rolling direction. The samples were then ground and polished with 9 µm, 3 µm and 1 µm diamond paste to remove surface damage from machining. In the centre of the sample, in a rounded area of 4 mm diameter, the thickness was reduced to ~120–200 µm to reach steady-state permeation through the thickness of the charged samples more quickly. Table 2 displays the thicknesses of the samples.

Table 2. *Case studies and sample thicknesses*

Case Study	Overall Thickness (mm)	Center-Reduced Thickness (mm)
Rate Dependence of Flow Properties (Tensile Samples)	1.06 ± 0.01	–
Effect of H Pre-Charging Time	0.5 ± 0.01	0.12 ± 0.01
Effect of Plasma Parameters	1.10 ± 0.01	0.18 ± 0.01
Effect of H Charging-Discharging	1.10 ± 0.01	0.20 ± 0.01

In-situ mechanical tests were performed in an SEM Zeiss Stereoscan 440 (Carl Zeiss GmbH, Oberkochen, Germany) operating at an acceleration voltage of 10 kV for imaging. A Kammrath & Weiss tensile stage (Kammrath & Weiss GmbH, Dortmund, Germany) equipped with a 10 kN load cell and an inductive displacement sensor was used for the tensile tests. The accuracy of the load cell is in the order of ~1 N, and the accuracy of the displacement sensor is ~0.5 µm.

The effect of strain rate was studied by tensile testing uncharged specimens with nominal strain rates of 3×10^{-5} s^{-1}, 1.5×10^{-4} s^{-1}, and 3×10^{-4} s^{-1}. For these tests, samples with uniform thickness and no thinned area were used. To further study the strain rate sensitivity and measure depth-dependent properties, nanoindentation testing was performed on a KLA G200 platform nanoindenter (KLA, Milpitas, CA, USA) that was equipped with a three-sided diamond Berkovich tip (Synton-MDP). Six constant strain rate indentations with an applied indentation strain rate of 0.05 s^{-1} and additionally five strain-rate jump tests with a strain-rate profile of 0.05 s^{-1}, 0.005 s^{-1}, 0.05 s^{-1}, 0.001 s^{-1}, and 0.05 s^{-1} (applied changes in the strain rate every 500 nm) were executed [41]. The continuous stiffness measurement technique was utilized to continuously measure the contact stiffness and, thereby, the hardness and Young's modulus over indentation depth. This technique involves applying a dynamic load that is then used to measure the stiffness, which is further processed in order to calculate the modulus and hardness of the material. This method allows for the measurement of the depth-dependent properties of materials [41].

2.2. Plasma H Charging

The effect of H-material interaction was studied on the CP steel while using a dedicated in-situ design. H was charged into the material via localised loading by a deuterium plasma cell, allowing for the combination of in-situ charging, mechanical testing, and observation in an SEM. The applied method consists of a miniaturized radio frequency-plasma cell, in which two electrodes are confined in a vacuum vessel and deuterium gas is supplied. The tensile sample, operating as the grounded electrode, can, in this way, be charged from the bottom side with the H isotope, providing a contamination free top surface for observation. Only the thinned centre of the samples was charged and the observation was localized in this region. The main advantage of this method, when compared to conventional electrochemical charging, is that it allows having a high-resolution observation during H charging and deformation. Furthermore, there is no risk for the SEM, since the plasma turns off automatically when the sample fractures. For more details of the method, see ref. [40].

The influence of different H charging conditions was examined by applying different power settings, obtaining plasmas with different bias voltages. A higher bias voltage can be correlated with a higher ion flux and implantation range and, consequently, higher ion concentrations. Power levels of 5 W, 6 W, 8 W, and 11 W were applied, resulting in DC bias voltages of 110 V, 127 V, 173 V, and 174 V, respectively. All of the samples were consistently only charged during the tensile test, i.e., no pre-charging was performed. It was demonstrated [42] that, in the presence of H, the reduction of fracture area increases with decreasing deformation rate and that only with slow strain rate testing the elongation to failure of a material can be decreased [34]. With a slow deformation rate, diffusible H has more time to migrate towards the crack tip, which results in an embrittlement of the material. For this reason, the tensile tests were performed with a slower strain rate than the previous cases, using a displacement rate of 0.1 µm/s. Afterwards, the fracture surfaces were observed in the FEG-SEM LEO 1525.

A sample was charged for 4 h and then discharged for 12 h before starting the test in order to address the potential reversibility of HE and the possibility of plasma damage. The results were subsequently compared with an uncharged specimen.

Moreover, maintaining plasma parameters fixed, the effect of pre-charging time was investigated. Three samples were tested: an uncharged sample for reference and two charged samples with 3 h and 6 h of H pre-charge, respectively. After the pre-charging time, the charging was also maintained during the tensile test (~1 h duration). Afterwards, the surfaces were analysed using EBSD and fractography was performed with the FEG-SEM using the previously mentioned parameters.

2.3. H Uptake and Diffusion Simulation

The model described in [43] was utilised in order to assess the present H concentration. This is a model for ion-driven permeation of H in plasma-facing materials at steady state. In steady-state, the incident flux is balanced with the reflected and permeated fluxes. Depending on the relative rate of recombination and diffusion on front and back sides of the membrane, there are three possible ion-driven permeation processes: diffusion-limited on both sides (DD regime), recombination-limited on both sides (RR regime), and recombination-limited on one side and diffusion-limited on the other side (RD regime). Equation (1) shows the estimation of the maximum concentration for a RR and RD regimes. In these regimes, the surface recombination is the rate-limiting step and is valid for fast-diffusion materials. Because the parameters on the back side do not affect the maximum concentration at steady state [43], the equation is the same for both cases.

$$C_{max} = \sqrt{\frac{\eta}{k_f}} \tag{1}$$

where C_{max} is the maximum lattice H concentration, η the ion flux, and k_f the recombination coefficient. The ion flux was calculated from Langmuir Probe measurements and it is described in detail in [40]. A Monte-Carlo program, SDTrim.SP 6.0 [44] was used for estimating the implanted fraction/particle reflection yield and the mean implantation range. The value of k_f was calculated according to three different sources [43,45,46].

For a more detailed analysis, the H concentration was calculated using a more sophisticated diffusion model [47,48], developed and implemented as subroutine (UMATHT) in the finite element simulation software package Abaqus (version 2019) [49]. Newton–Raphson scheme is used to solve the system of equations, whereas Crank–Nicholson procedure is used for the time integration. This is a sequentially coupled diffusion-mechanical model, which considers concentration driven diffusion, stress driven diffusion, as well as physically meaningful boundary conditions. The interplay between trapped and lattice H is considered by the following relationship written in its multiple trap formulation [50]:

$$\frac{\gamma_{lattice}\left(1-\gamma_{trap,k}\right)}{\gamma_{trap,k}\left(1-\gamma_{lattice}\right)} = \exp\left(-\frac{\Delta E_k}{R_g T}\right), \quad (k = 1, \dots, m) \tag{2}$$

With $\gamma_{lattice}$ as site fraction of lattice H, $\gamma_{trap,k}$ as trap site fraction and ΔE_k as trapping energy for the kth sort of trap. The parameters of the model can be either determined from permeation experiments [51,52] or from thermal desorption spectroscopy measurements [53,54]. The applied model for the CP1200 steel only considers one effective trap with a trap energy of 30 kJ/mol and a trap density of 5.7×10^{-7} [18]. A trapping energy of about 30 kJ/mol is representative for dislocations and some kinds of grain boundaries and it is related to rather shallow traps. The three-dimensional (3D) sample geometry was modelled making use of a quarter symmetry and it was discretised by finite elements with linear shape functions (DC3D8) and an element size of interest of 2×10^{-3}–2×10^{-2} mm, resulting in a number of 13 elements alongside the flux direction. A mesh convergence study was done in order to avoid mesh dependency of the results. The applied flux boundary condition on the plasma-oriented surface in the 3D model results from the incident ion intake flux ϕ_i of 10^{20} $m^{-2}s^{-1}$ in 1.15 nm depth and on the recombination flux $\phi_r = k_f c_{lattice}^2$, with $c_{lattice}$ being the locally corresponding lattice hydrogen concentration. Due to narrow distance between the flux due to plasma loading and the recombination flux, the one-dimensional (1D) hydrogen permeation FE model calculated net influx is used to prescribe the hydrogen intake in the 3D model. Figure 2 depicts the boundary conditions applied to the 1D hydrogen permeation model. In fact, the boundary conditions on the SEM-oriented face of the sample were chosen corresponding to, both, the RR ($flux = k_f c_{lattice}^2$) and the RD ($c_{lattice} = 0$) regimes, and the differences were negligible. Therefore, only the model and results of the RD case are shown in the present paper.

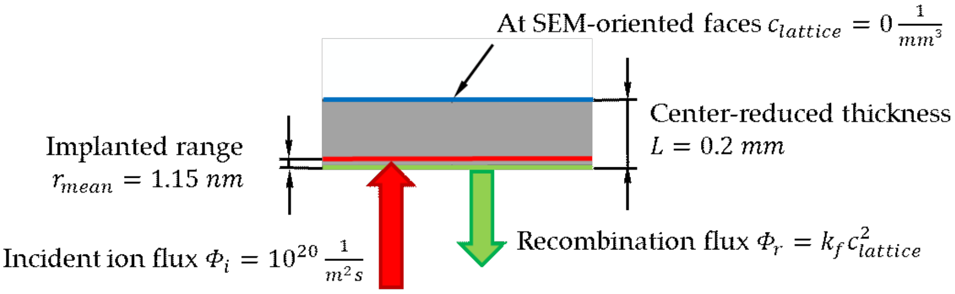

Figure 2. RD boundary conditions of the one-dimensional (1D) hydrogen permeation model. The time history of the sum of the incident ion flux and the recycling flux is applied as boundary condition at the H charging area in the three-dimensional (3D) model.

B. 3. Results

3.1. Rate Dependance of Flow Properties

Figure 3a shows the stress–strain curves of three specimens that were tested with 3×10^{-5} s^{-1}, 1.5×10^{-4} s^{-1}, and 3×10^{-4} s^{-1}. The initial part of the curve that corresponds to 3×10^{-5} s^{-1} strain rate does not start with zero stress, due to possible friction effects, but after approximately 1% strain, the curve exhibits a normal behaviour. There is almost no difference between the three curves; the yield stress is ~1060 MPa, the tensile strength ~1200 MPa, and strain to failure ~9%. The strain rate sensitivity of a material can be verified by the value of the strain rate sensitivity index, m, from a simple power-law relationship [55]:

$$\sigma = \varepsilon^{m} \tag{3}$$

where σ is the flow stress and ε the strain rate. The value of m can be then determined as the slope of the plot of lnσ vs. lnε. Figure 3b depicts the flow stress vs. strain rate for the strains that are indicated in the box in Figure 3a. The calculated *m* for three curves was almost zero, proving that the material exhibits no significant strain rate sensitivity in the investigated strain rate regime.

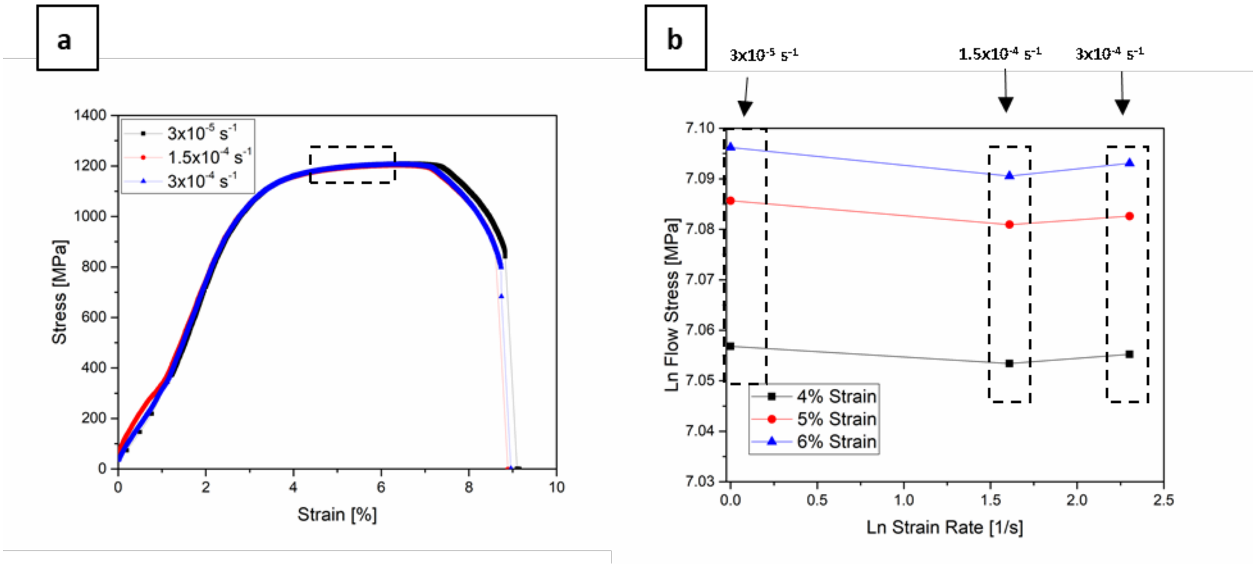

Figure 3. (a) Stress-strain curves of CP 1200 steel tested strain rates of 3×10^{-5} s^{-1}, 1.5×10^{-4} s^{-1}, and 3×10^{-4} s^{-1}; (b) ln flow stress-ln strain rate plot for the strains indicated in the box in (**a**), showing no significant strain rate sensitivity.

At a macroscopic level, the three samples exhibited a high degree of ductility (necking). Figure 4 shows the fracture surfaces of the three specimens, where the same ductile failure behaviour was observed for all specimens, i.e., microvoid coalescence, leading to the presence of dimples on the fracture surfaces. The size of approximately 50 dimples in each of the three samples were estimated from the SEM images, giving a bimodal distribution with sizes of 14.5 ± 0.8 µm and 6.6 ± 0.6 µm. No effect of strain rate was observed in the tested range.

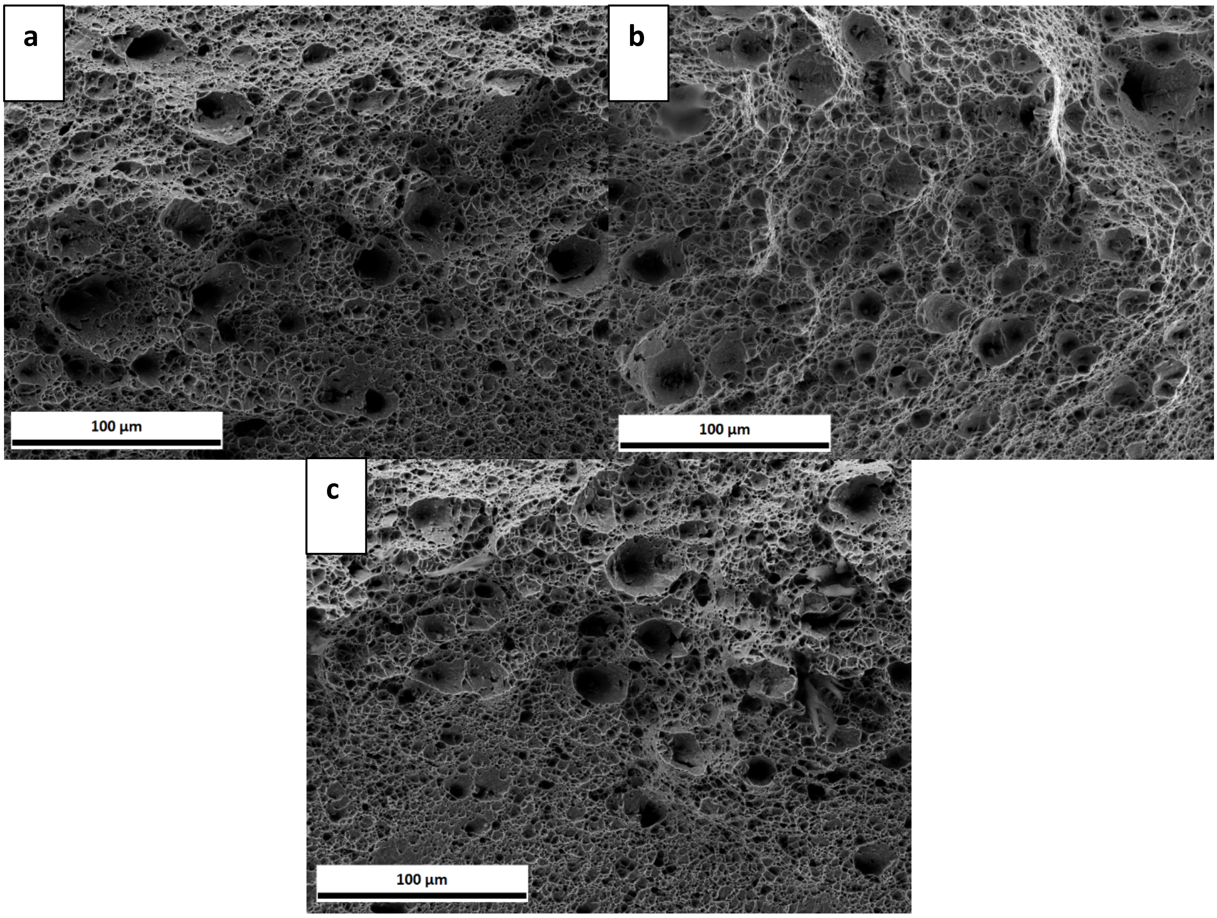

Figure 4. Fracture surfaces of complex phase (CP) steel tested with strain rates of (**a**) 3×10^{-5} s^{-1}; (**b**) 1.5×10^{-4} s^{-1}; (**c**) 3×10^{-4} s^{-1}.

From the constant strain rate indentation tests, the average hardness and Young's Modulus were calculated to be 5.13 GPa and 233 GPa, respectively. Similar hardness values were reported for tempered martensite and martensitic steels with similar C content [56,57]. Figure 5a depicts the load-indentation depth plot that corresponds to the strain rate jump tests and Figure 5b shows the exemplarily resulting hardness and Young's modulus over indentation depth. The Young's modulus is independent of the applied strain rate and the differences in data points is due to the differences in testing times with different strain rates. The hardness levels clearly shift with strain rate, even though by only a small amount. The decreasing hardness at very shallow indentation depths is related to the indentation size effect [58], but it does not affect the analysis of strain rate sensitivity. The calculation of the strain rate sensitivity m in nanoindentation experiments is made with the hardness, which is directly related with the stress through Equation (4):

$$\sigma = H/C^{*} \qquad (4)$$

where σ is the flow stress, H the hardness and C^* a constraint factor. The calculated strain rate sensitivity m was on average 0.006 ± 0.0005. This result confirms that the material exhibit almost no strain rate sensitivity within the tested parameter range.

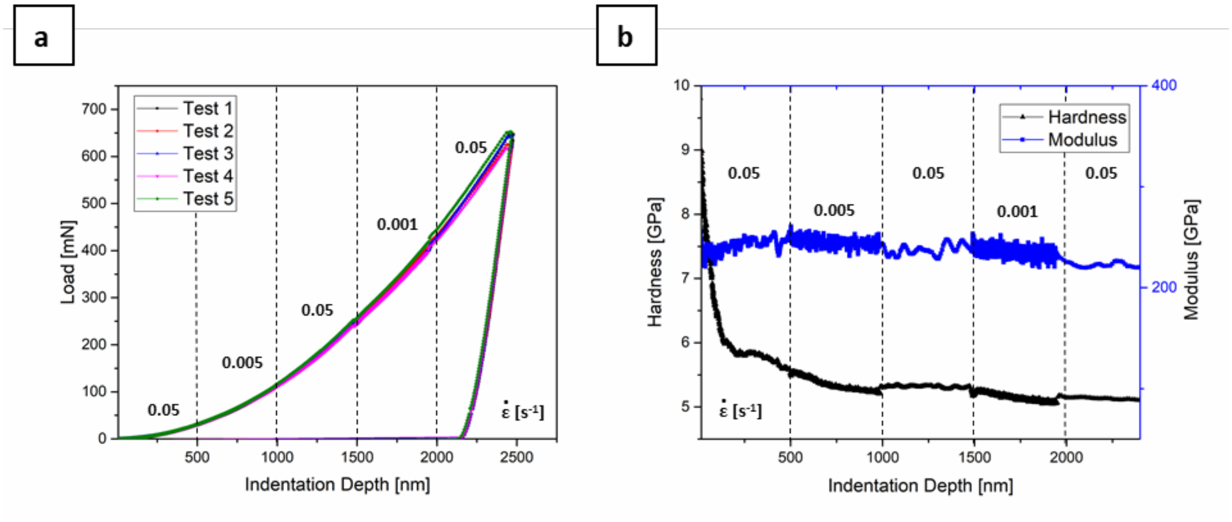

Figure 5. (**a**) Load-indentation depth plots corresponding to jump tests with 0.05 s^{-1}, 0.005 s^{-1}, 0.05 s^{-1}, 0.001 s^{-1}, and 0.05 s^{-1}, with a change in the strain rate every 500 nm; (**b**) the exemplarily resulting hardness and Young's modulus.

3.2. Effect of H Charging

3.2.1. Effect of Pre-Charging Time

Figure 6 depicts the load-elongation curves of an uncharged sample and two charged samples with different pre-charging times, both also continuously charged during the tensile test. The first linear part of the curve is not affected by the presence of H. However, a trend can be observed in the plastic part, after the crack onset, which is indicated by an arrow. With increasing H-charging time, the elongation to failure decreased slightly, and there was a more pronounced drop in the load at ~ 200 µm, which is when cracking was initiated.

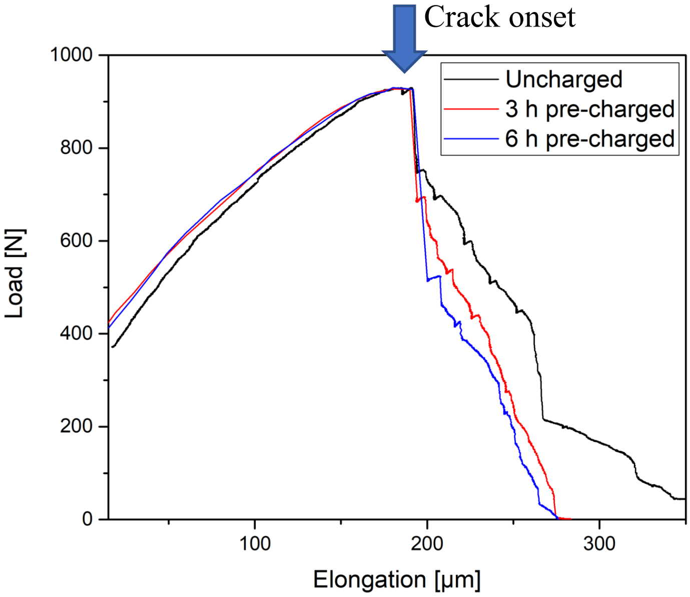

Figure 6. Load-elongation curves of three CP steel samples: uncharged, 3 h, and 6 h pre-charged.

In Figure 7, the fracture surfaces of the three samples are presented. The uncharged sample, Figure 7a, exhibits a ductile failure. When comparing with the uncharged samples from Figure 4, they do not look very similar, since, in this set of samples, the thickness was reduced in the centre of the sample, as described above, which gives rise to a somewhat different appearance of the fracture surface. The charged samples presented in Figure 7b,c, on the other hand, exhibit some differences when compared to the uncharged specimen. In Figure 7b, in addition to voids, some flat regions can be seen. In the sample with the longer charging time, Figure 7c, there is a marked difference between the upper and lower part of the fracture surface, as indicated with a red line. Only in the upper part of the surface microvoids can be observed, while the lower part, where the H was supplied, shows another failure mechanism with more localized damage. Even though the lower part of Figure 7a also exhibits some surface damage, this is less pronounced than for the charged sample.

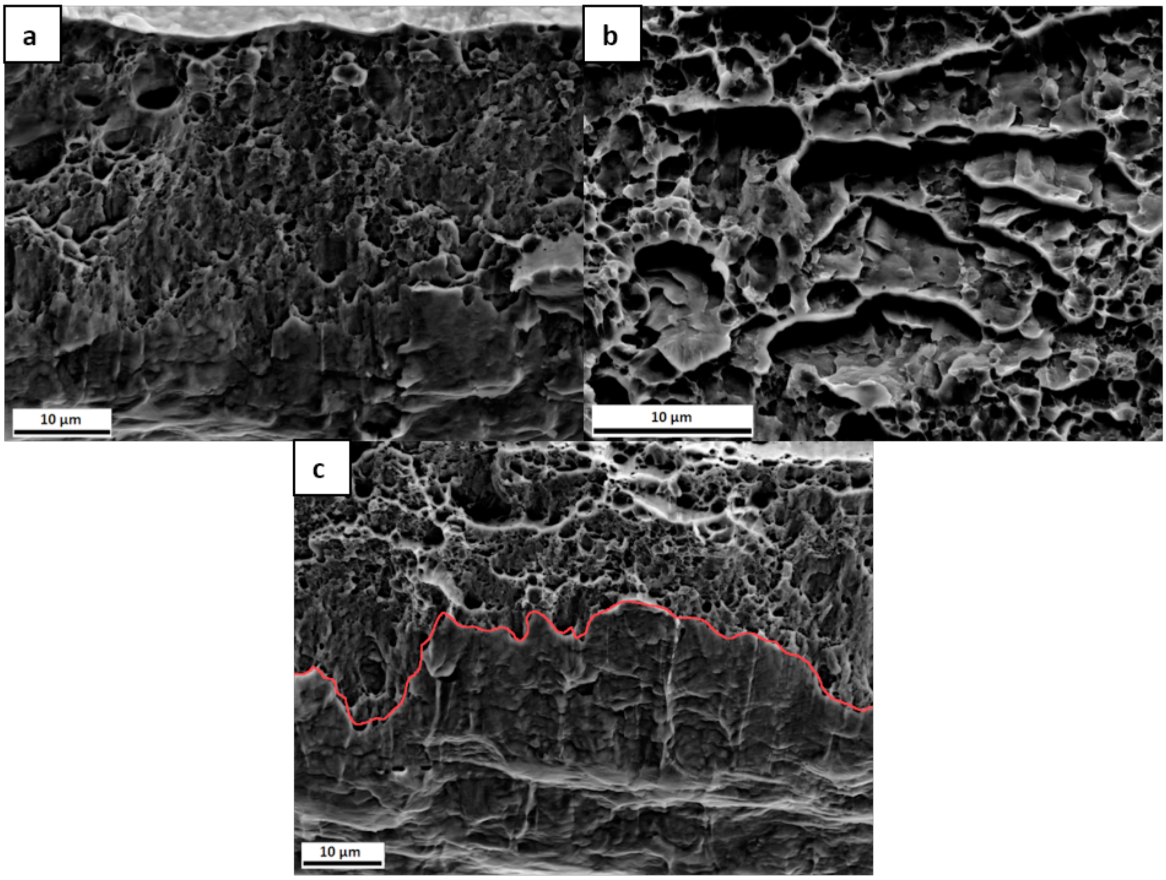

Figure 7. Fracture surfaces of the (**a**) uncharged; (**b**) 3 h pre-charged; and, (**c**) 6 h pre-charged CP steel samples.

From in-situ SEM images that were recorded during the tests, the linear intercept of the crack length was estimated at different loading steps for each sample, as shown in Figure 8a. For comparison purposes, the crack initiation times were normalized to 0 s. When comparing the slopes of the curves for each sample, it can be seen that the crack propagation rate increased with charging time. Figure 8b shows a linear estimate of the crack growth rate for the three samples. While the crack growth rate for the uncharged sample was ~1.5 μm/s, the 3 h pre-charged sample exhibited a rate of 2.5 μm/s, while, for the 6 h pre-charged one, it further increased to 3 μm/s.

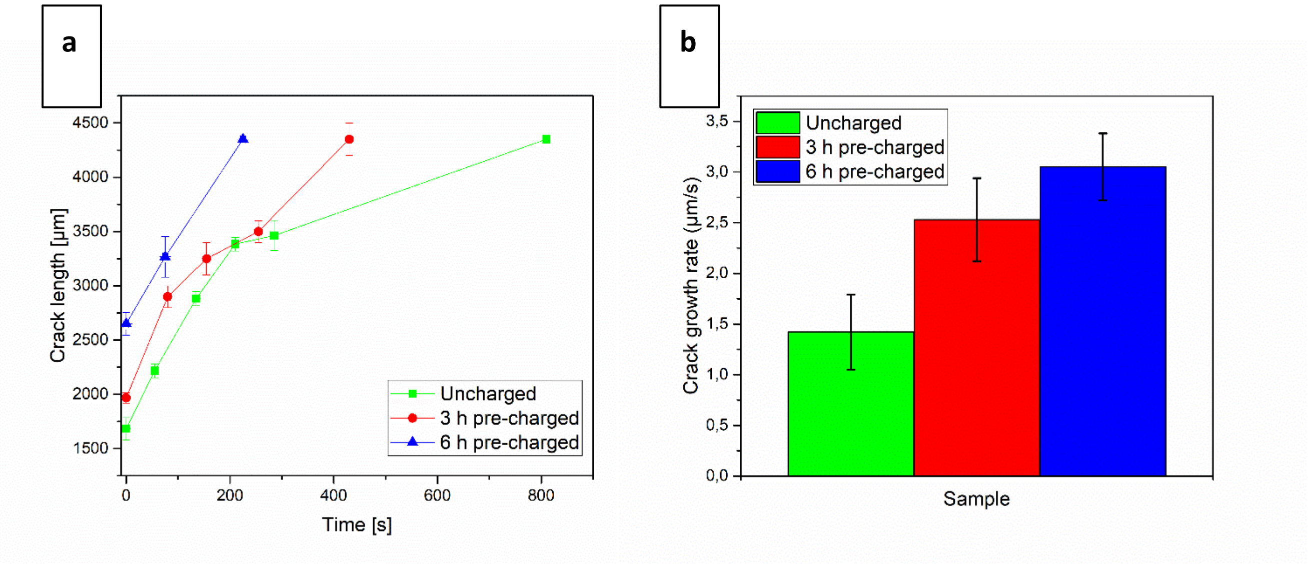

Figure 8. (**a**) Normalized crack length evolution; (**b**) crack growth rate of the uncharged, 3 h pre-charged and 6 h pre-charged CP steel samples.

The surface of samples in regions near the fracture site was analysed using EBSD. The Inverse Pole Figure maps in the normal direction are shown in Figure 9. Secondary cracks, highlighted with arrows, can only be seen in the sample with the longer charging time, Figures 9c and d. Nevertheless, while the secondary cracks seem to follow interfaces in Figure 9c, it was not possible to determine whether the cracks started at grain boundaries or inside the grains. No secondary cracks were observed in the uncharged and 3 h pre-charged samples.

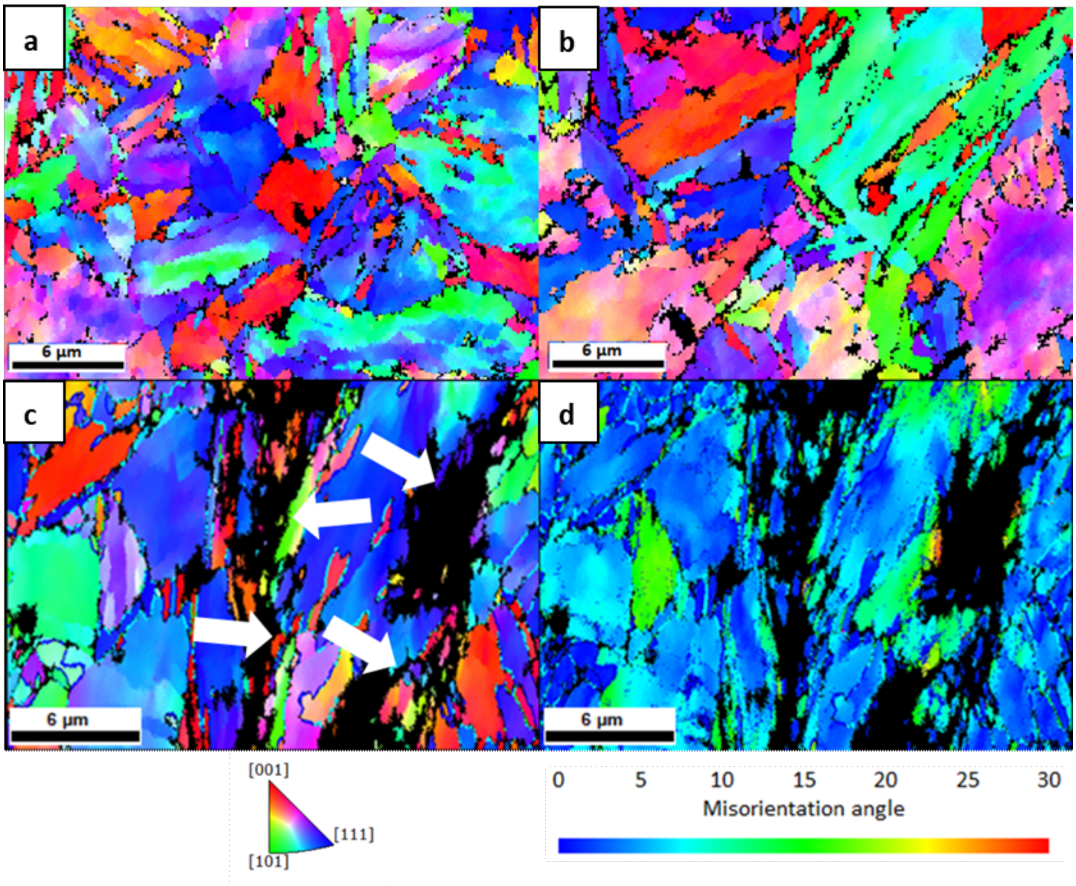

Figure 9. Inverse Pole Figure maps in the normal direction of the (a) uncharged, (b) 3 h pre-charged, (c) 6 h pre-charged CP steel samples near the fracture and (d) misorientation map of 6 h pre-charged CP steel sample.

3.2.2. Effect of Plasma Parameters

Figure 10 shows the load-elongation curves of samples tested under different plasma conditions. The noise that was observed in some of the curves was due to interference between the radio frequency power supply and the electronics in the tensile module, despite the shielding of the cables. While inconvenient, this does not affect the data. It is important to mention that, since the samples used for each case study correspond to a different machining set, the difference in thickness gives rise to different maximum loads.

The linear loading regimes of the curves are approximately the same for all tested samples. Nevertheless, there are some differences in the maximum load (tensile strength) and elongation to failure. It was expected that the samples with higher power and, therefore, higher H concentration, would be the first ones to fail, but no clear trend was observed. Because load is plotted instead of stress due to the locally thinned sample geometry, the differences in tensile strength could be attributed to small differences in the thickness of the samples due to fabrication. Even a slight difference of ~0.02 mm in the thicknesses of the thinned area of the samples tested could lead to an error of around 5.5% and 3.5% in the maximum load and elongation to failure, respectively, which is consistent with the differences observed in Figure 10. Considering that the H concentration increases with the power (a higher power results in a higher plasma bias voltage), the sample that was tested with 11 W should have the smallest elongation to failure, while the sample with 5 W, the largest. In Figure 10 it can be seen that, even though the sample with 11 W has lower elongation to failure than the samples with 6 W and 8 W, the one with 5 W has approximately the same.

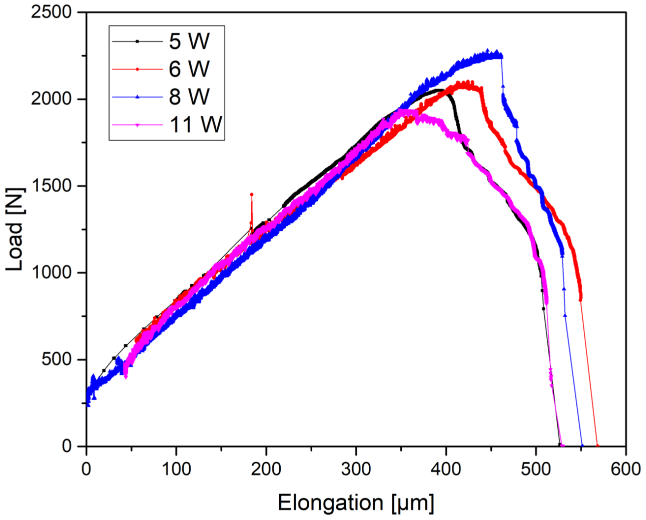

Figure 10. Load-elongation curves of CP 1200 steel tested under different plasma charging conditions. Power levels of 5 W, 6 W, 8 W, and 11 W were applied for running the plasma.

Figure 11 displays the fracture surfaces of the tested samples within the reduced thickness area. Although all of them failed in a ductile manner, they exhibited less degree of necking than the uncharged specimens and there were some differences at the microscopic level. Figure 11a,b show a very similar morphology. While the upper part of the surfaces exhibit the presence of dimples, the lower parts show a rather smooth surface with less dimples. Figure 11c, on the other hand, shows a mixture of dimples with areas (marked with a box) that could be shear fracture or grains specially oriented. In Figure 11d, the fracture surface morphology is more uniform than the previous cases, being dominated by the presence of small dimples.

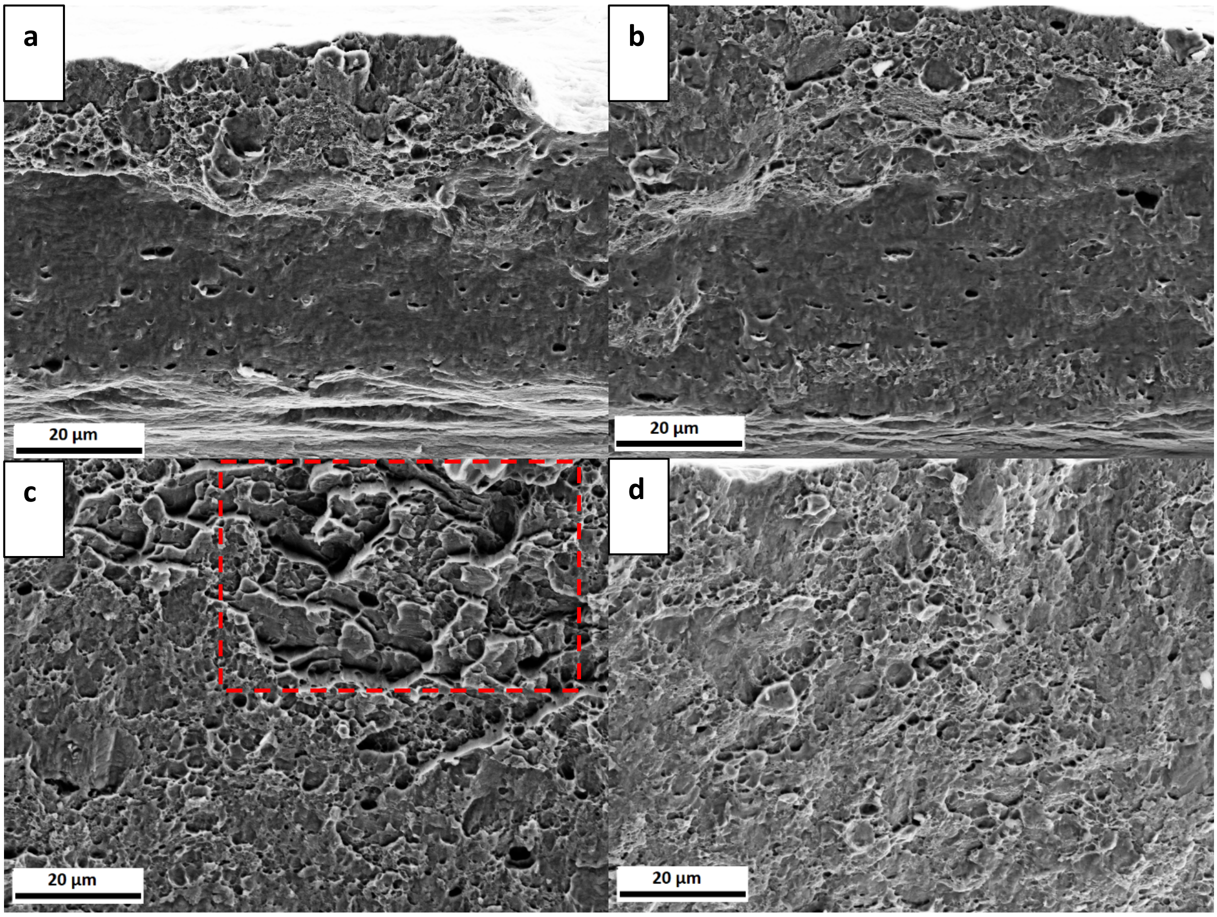

Figure 11. Fracture surfaces of the CP steel specimens tested with (a) 5 W; (b) 6 W; (c) 8 W; and, (d) 11 W. The red box in (c) indicates an area with shear fracture or specially oriented grains.

3.2.3. Effect of H Charging-Discharging

In Figure 12, the stress-strain characteristic of an uncharged sample is compared to a sample that was charged and tested after a discharging time of 24 h. There are some differences in the data, but these are related to small dimensional differences. This would support the notion that HE is a reversible effect. Fractography was also performed to fully support this statement.

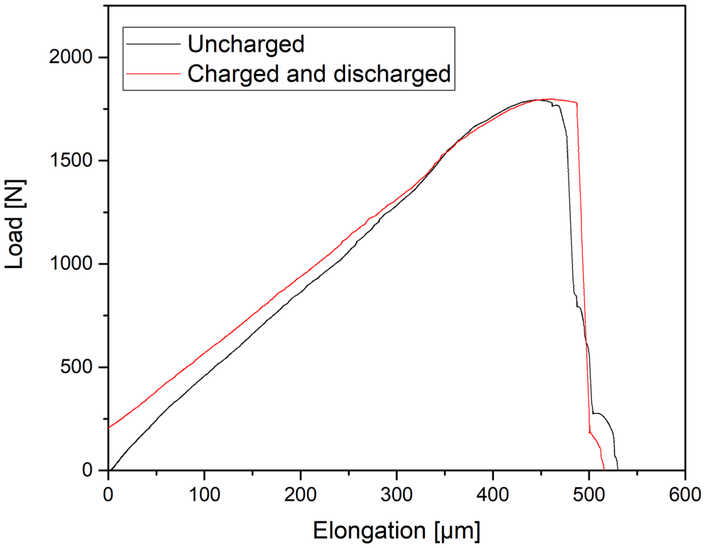

Figure 12. Load-elongation curves of an uncharged CP 1200 steel sample and one initially charged for 4 h and tested after discharging for additional 12 h in vacuum.

Figure 13 shows fracture surfaces corresponding to the uncharged and charged and discharged samples. It can be seen that, while the uncharged sample exhibits a typical ductile microvoid coalescence failure, see Figure 4, the charged and discharged sample display some regions where the morphology is similar to the one presented in Figure 11c, with a mixture of dimples and more flat features.

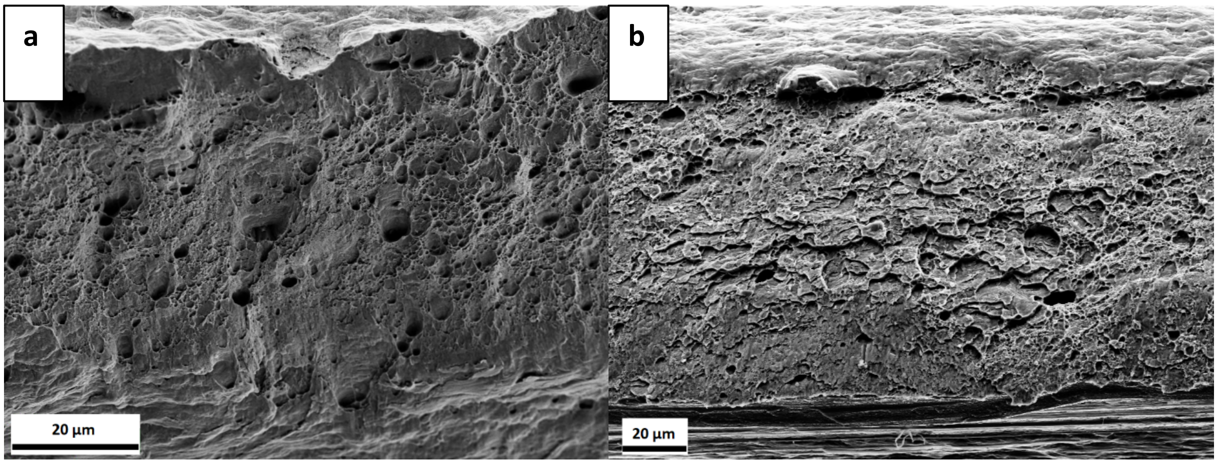

Figure 13. Fracture surfaces of the (**a**) uncharged and (**b**) charged and discharged CP steel specimens.

3.3. H Concentration

The Monte-Carlo program STrim.SP 6.0D gave a r_{mean}=1.15 nm and that 41% of the particles are implanted. From Langmuir Probe measurements [40], the ion flux was calculated to be 10^{20} $m^{-2}s^{-1}$. Table 3 shows the recombination coefficients that were calculated according to refs. [43,45,46] and the resulting H concentration. Because the different sources resulted in different concentration values, it is considered that they give a range for H concentration. It is important to mention that these values correspond to lattice H, i.e., the analytical calculation does not consider the trapping effect and, therefore, a higher concentration is expected in the material.

Table 3. Recombination coefficient and lattice H concentration calculated with different sources.

Source	k_f (m^4 s^{-1})	$C_{lattice}$ (wppm)
Shu et al. [43]	1.75×10^{-21}	1.31×10^{-4}
Zhou et al. [45]	5.56×10^{-21}	7.34×10^{-5}
Baskes [46]	5.00×10^{-24}	2.45×10^{-3}

Figure 14 shows more elaborated simulation results. Here, Figure 14a depicts the cross section with two different views of the tensile samples, where the arrows indicate the direction of H charging. The concentration decreases through the thickness of the sample, resulting in 0 wppm at the top surface. The lattice concentration shows very good agreement with the analytical calculation made with ref. [46]. However, the total H concentration summing over the H stored in the interstitial lattice positions and in H traps reaches 0.82 wppm, and it is around a factor of 350 higher than the corresponding lattice H. Figure 14b shows the corresponding flux for the three sources in the evaluation node. Even though the values differ, the three cases show that a steady state is reached after approximately 500 s.

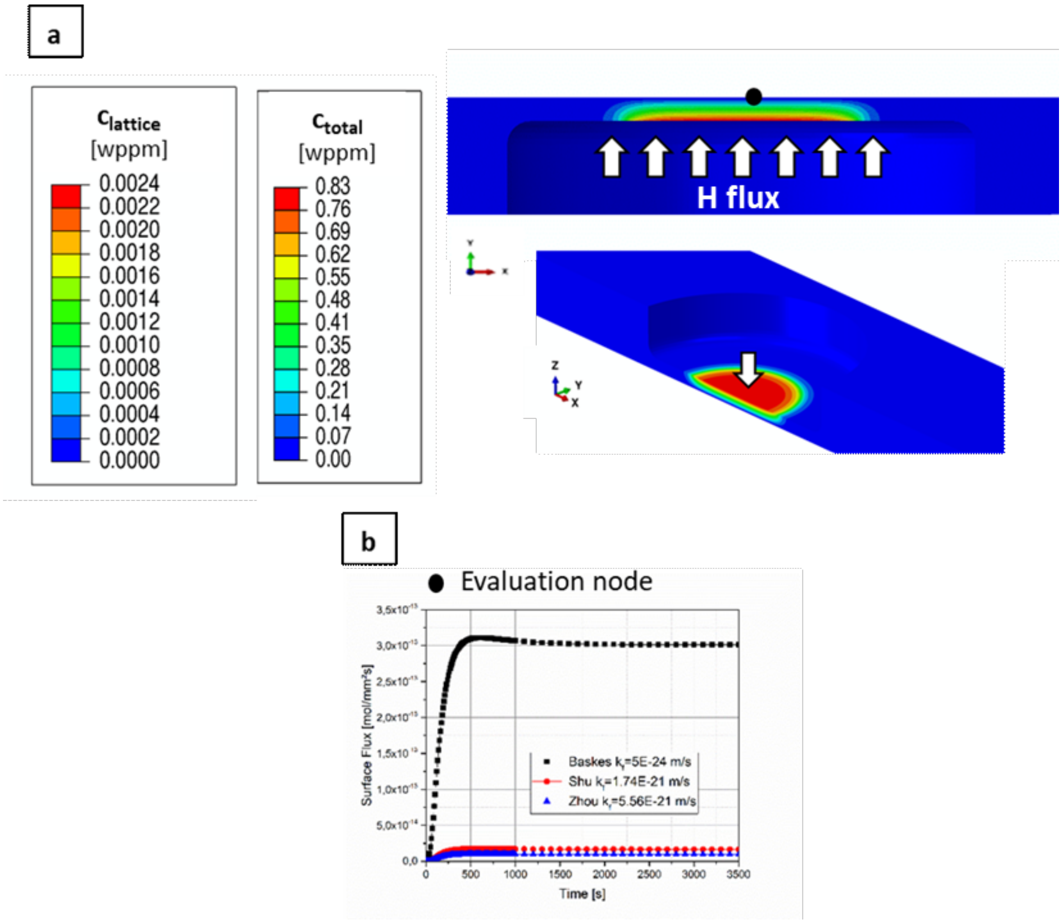

Figure 14. (a) H concentration distribution through the thickness of the CP steel sample, the arrows indicate the direction of H charging from the bottom of the samples; and (b) H flux over time in an evaluation node on the top surface of the sample.

B. 4. Discussion

The H degradation behaviour is known to be dependent on the concentration of the absorbed H [58]. Zackroczmski et al. studied the effect of H concentration on a duplex stainless steel and concluded that the intensity of HE was strongly dependent on the concentration of the absorbed H. Furthermore, HE does not occur below a critical H concentration value [6,17]. Generally speaking, a higher DC self-bias voltage leads to a higher ion concentration [60]. This means that, increasing the power supplied to the RF discharge, an increase in the H concentration should be obtained. Taking this into account, it was expected that, with increasing power in Figure 10, the total elongation (related to the ductility of the specimens) should decrease. As mentioned before, this behaviour was not observed in the samples that were tested with 5 W, 6 W, 8 W, and 11 W, and considering that the accuracy of the displacement sensor is ~0.5 µm, the small differences in elongation to failure could be attributed to the 3.5% error arising from the slight differences in thickness.

Although there were no marked differences in the load-elongation curves, the fracture surfaces exhibited different characteristics. When comparing with the fracture surfaces of the uncharged samples shown in Figure 4, there are some differences with the charged samples in Figure 11. The uncharged samples exhibit a typical ductile failure, formed by the coalescence of large voids involving the nucleation and growth of small voids leading to the presence of large and small dimples on the fracture surface with a bimodal distribution [61]. On the other hand, although, in the charged samples, dimples can also be observed, these have smaller size than in the uncharged case. The dimple size of the samples tested with 5 W and 6 W, as estimated from the SEM images, was 1.4 ± 0.2 µm. The sample tested with 8 W exhibited a dimple size of 2.4 ± 0.5 µm and the 11 W sample, 1.8 ± 0.4 µm. While these values do not follow a specific trend, they are smaller than the uncharged specimens, which presented a bimodal distribution with sizes of 14.5 ± 0.8 µm and 6.6 ± 0.6 µm, as before mentioned. This is in agreement with many previous studies, which showed that the presence of H reduces the dimple size on the fracture surface [58–66].

Moreover, the samples depicted in Figures 11a and b show similar features: the lower part of the fracture surface is rather flat with less dimple features, while the upper part looks more similar to ductile failure. This flat part could be the result of the plastic deformation of the sample. Nevertheless, the dimples in this case are uniform in size and there is not a bimodal distribution present as compared to the uncharged specimens. The similarities between these two samples, with 5 W and 6 W, could be attributed to similar H concentration values. When considering that the H charging is conducted from the bottom of the sample, it is reasonable that with a gradient in H concentration, a gradient in the fracture surface morphology is obtained. In contrast to these two specimens, the ones that were tested with 8 W and 11 W exhibit a more uniform fracture surface, less plastically deformed, and also different to the ones seen in the uncharged specimens. Both of the samples have smaller dimples than the uncharged ones and the main difference between the two charged samples is that in the 8 W condition there are some with flat features. It has been reported [67] that a reduction in dimple size can be a consequence of H effect and it represents a large increase in dimple nucleation.

The load-elongation curves presented in Figure 12 demonstrate that there is either no effect on the mechanical properties caused by the presence of H, or that this effect is reversible, and the properties of the material are restored once the H is eliminated from the samples. These facts would be in line with the premise that diffusible H, which can allegedly diffuse out of the specimens at room temperature, is responsible for HE [68], while trapped H has little to no effect. It has been reported [16] that, in this material, H is mainly trapped at dislocations and martensitic lath boundaries, which are not deep traps. Therefore, it is believed that all of the H effuses when discharging the material.

Anyways, the observation of the fracture surfaces in Figure 13 demonstrates that the failure characteristic is somewhat affected.

In Figure 6, the load-elongation curves depict a different trend than in the previous cases. Notably, the three specimens tested converged to approximately the same maximum load. This is mostly set by the unaffected uncharged specimen parts. However, once the failure in the thinned charged parts of the samples started, there was a larger drop in the load with increasing charging time. Furthermore, the crack propagation rate, as shown in Figure 8, also increased in the presence of H and the ultimate strain was reduced by the presence of H. Even though the crack propagation rate was accelerated with increasing charging time, the final elongation was approximately the same for the charged samples. This is in agreement with the result presented in Figure 14b, where it is shown that a steady-state is reached after a very short charging time and the H concentration does not further increase. It is also worth mentioning that the material exhibits diminishing strain rate sensitivity (see Section 3.1.), which means that the changes in crack propagation rate does not relate to different loading situations, but due to H effects on crack propagation.

The fracture surfaces in Figure 7 depict that, in the presence of H, the fracture morphology changed. In the 3 h pre-charged sample, as in Figure 7b, there are “flat” regions, while, in the sample with 6 h of H pre-charge, there is damage in the bottom part of the surface. Although none of the samples exhibited brittle fracture characteristics, the fracture morphology was affected by the presence of H for both pre-charging times, (Figure 7b and c). It is known that the morphologies of H-enhanced fracture surfaces can be changed from microvoid coalescence to quasi-cleavage, cleavage or intergranular fracture, or they can also be unaffected [69]. Furthermore, dimple size was also calculated from the SEM images for these samples, again confirming again that, in the presence of H, the dimple size was reduced. The uncharged specimen exhibited a dimple size of 3.2 ± 0.9 µm, while the sizes of the 3 h pre-charged and 6 h pre-charged samples were 1.3 ± 0.1 and 1.4 ± 0.2 µm, respectively.

To gain a better understanding on the H effect on these samples, the surfaces of the samples were also investigated through EBSD. Analysing the EBSD scans next to the fracture site, it was evident that in the 6 h pre-charged sample secondary cracks formed, and a larger amount of local misorientation in their surroundings was present, as shown in Figure 9d. Misorientation maps can be used as an approach for visualizing plastic deformation. They are a measure of the geometric dislocations in the crystalline lattice and, therefore, measures of plastic deformation at the microstructural level [70]. Although there is a lack of quantitative measures of deformation (strain, strain gradient, dislocation density, etc.), it can be locally related to the density of geometrically necessary dislocations. This indicates that in the sample with 6 h pre-charging, there is a localized plastic deformation in the areas next to the secondary cracks, which means that H could promote a greater dislocation activity in some regions of the microstructure that eventually lead to the formation of many secondary cracks.

The calculation of the present H concentration using two different approaches, a simple analytical method and a more sophisticated simulation approach, generally results in a low value. As expected, there is a gradient through the thickness of the sample, giving the lowest value at the top surface subjected to observation. On the plus side, a steady state concentration profile is reached after only 500 s. This is almost immediately after starting the charging, meaning that varying the pre-charging times would not have any effect in the results, as confirmed by the final elongation of the charged samples presented in Figure 6. Nevertheless, this does not explain why the crack propagation rate increased with charging time and why secondary cracks were only observed in the 6 h pre-charged sample. A possible explanation is that with pre-charging deeper traps are filled up causing more damage.

The low H concentrations could explain why there were no major differences in the load-elongation curves presented in Figure 10, i.e., the mechanical properties were not strongly affected. According to the simulation results that are shown in Figure 14, the maximum H concentration in the plasma-exposed surface is 0.83 wppm and Drexler et al. [18] found that for the same CP1200 steel there is a minor effect on the fracture strain at this H exposure. When considering that during body in white painting process, steel absorbs around 0.4 wppm of H content [5], it would be safe to assume that the CP steel will maintain its mechanical properties during this production process. Drexler et al. [18] showed that a pronounced HE starts at a H concentration of around 2 wppm. Nevertheless, as mentioned previously, some differences in the fracture surfaces were observed, especially when compared with the uncharged specimens, already indicating an onset on material behaviour modification at quite low H concentration, but without losing their strength and ductility.

Low H concentrations will always be a challenge for this high-diffusivity material, but different technological alternatives can be implemented in order to solve this issue. In the future, for example, impermeable nm thick coatings, transparent to the electron beam, could be used to limit the outgassing on the top surface of the sample. For instance, Baskes et al. [46] proposed that permeation barriers made of, for example, Ti or Zr could be used to reduce the recombination coefficient by more than 10 orders of magnitude giving a significant increase in the total H concentration in the material. Another alternative could be to reduce the sample temperature. A higher temperature enhances diffusion and, thereby, reduces the maximum concentration [71].

Even though it is not possible to fully eliminate the gradient in the H concentration, the maximum solute concentration would be higher. Furthermore, the swift diffusion of H defines that only by using an in-situ charging approach any modification can be observed. Ex-situ charged samples would immediately return to their original condition, as shown in Figure 12.

B. 5. Conclusions

The presented methodology allowed for having a direct observation of H effect on a CP steel during tensile tests, enabling monitoring the deformation and crack propagation with their correlation to the load-elongation curves. With more conventional charging methods, such as H gas or electrochemical charging, it can be very challenging to have in-situ charging and observation and, for such fast diffusing materials, only direct observation during in-situ charging, as established here, will allow addressing H effects on materials.

Different approaches were performed in order to investigate the behaviour of the steel under the effect of H. The combination of the applied charging conditions and a material exhibiting high H diffusivity resulted in a low H concentration, slightly below the critical value in order to produce embrittlement in the samples. Even though there was a constant supply of H, which led to a dynamic equilibrium of H concentration, this value was not sufficient to have a large impact on the mechanical properties of the material. When comparing these results with the H concentration absorbed during the body in white painting process, it can be concluded that the CP steel is a suitable material to build body in white components.

As aforementioned, there are already slight modifications in fracture characteristics and crack propagation rates, even noticeable at these concentrations. Furthermore, a number of possible future alternatives to generally increase the total H concentration in the material microstructure exist.

Acknowledgments

The authors gratefully acknowledge the financial support under the scope of the COMET program within the K2 Center “Integrated Computational Material, Process and Product Engineering (IC-MPPE)” (Project No 859480). This program is supported by the Austrian Federal Ministries for Climate Action, Environment, Energy, Mobility, Innovation and Technology (BMK) and for Digital and Economic Affairs (BMDW), represented by the Austrian research funding association (FFG), and the federal states of Styria, Upper Austria and Tyrol. The authors also acknowledge Voestalpine Stahl GmbH for the donation of the CP1200 material.

B. 6. References

[1] Matlock, D. K.; Speer, J. G.; De Moor, E.; Gibbs, P. J. Recent developments in advanced high strength sheet steels for automotive applications: An overview. *Jestech.* 2012, *15*, 1–12.

[2] Bergmann, C.; Mraczek K.; Kröger B.; Sturel T.; Jürgensen J.; Yagodzinskyy Y.; Guo X.; Vucko F.; Kuhlmann M.; Veith S.; Pohl M. Hydrogen embrittlement resistance evaluation of

advanced high strength steel for automotive applications. In Proceedings of Steely Hydrogen, Ghent, Belgium, 29–31 May 2018, A01:1-15.

[3] Eurostat. Available online: https://ec.europa.eu/eurostat/statistics-explained/index.php/Construction_production_(volume)_index_overview (accessed on 15 July 2020).

[4] Figueroa, D.; Robinson, M. The effects of sacrificial coatings on hydrogen embrittlement and re-embrittlement of ultra high strength steels. *Corros. Sci.* 2008, *50*, 1066–1079, doi:10.1016/j.corsci.2007.11.023.

[5] Lovicu, G.; Bottazzi, M.; D'Aiuto, F.; De Sanctis, M.; DiMatteo, A.; Santus, C.; Valentini, R. Hydrogen Embrittlement of Automotive Advanced High-Strength Steels. *Met. Mater. Trans. A* 2012, *43*, 4075–4087, doi:10.1007/s11661-012-1280-8.

[6] Louthan, M.R. Hydrogen Embrittlement of Metals: A Primer for the Failure Analyst. *J. Fail. Anal. Prev.* 2008, *8*, 289–307, doi:10.1007/s11668-008-9133-x.

[7] Hilditch, T.B.; Lee, S.-B.; Speer, J.G.; Matlock, D.K. Response to Hydrogen Charging in High Strength Automotive Sheet Steel Products. *Sae Tech. Pap. Ser.* 2003, 47–56, doi:10.4271/2003-01-0525.

[8] Gerberich, W.W.; Oriani, R.A.; Lji, M.-J.; Chen, X.; Foecke, T. The necessity of both plasticity and brittleness in the fracture thresholds of iron. *Philos. Mag. A* 1991, *63*, 363–376, doi:10.1080/01418619108204854.

[9] Oriani, R. A.; Josephic, P. H. Equilibrium aspects of hydrogen-induced cracking in steels. *Acta Metall.* 1974, *22*, 1065–1074.

[10] Lynch, S. Environmentally assisted cracking: Overview of evidence for an adsorption-induced localised-slip process. *Acta Met.* 1988, *36*, 2639–2661, doi:10.1016/0001-6160(88)90113-7.

[11] Lynch, S. Metallographic contributions to understanding mechanisms of environmentally assisted cracking. *Metals.* 1989, *23*, 147–171, doi:10.1016/0026-0800(89)90016-5.

[12] Lynch, S.P. Comments on "A unified model of environment-assisted cracking. *Scr. Mater.* 2009, *61*, 331–334, doi:10.1016/j.scriptamat.2009.02.031.

[13] Birnbaum, H.; Sofronis, P. Hydrogen-enhanced localized plasticity—a mechanism for hydrogen-related fracture. *Mater. Sci. Eng. A* 1994, *176*, 191–202, doi:10.1016/0921-5093(94)90975-x.

[14] Robertson, I.; Birnbaum, H.; Sofronis, P. Chapter 91 Hydrogen Effects on Plasticity. In *Dislocations in Solids*; *2009*; *15*, 249–293.

[15] Birnbaum, H.K. Mechanisms of Hydrogen Related Fracture of Metals. In *Mechanisms of Hydrogen Related Fracture of Metals*; Defense Technical Information Center (DTIC), Urbana, Illinois, USA, 1989; pp. 639–658.

[16] Birnbaum, H. K.; Robertston, I. M.; P.; Sofronis, I. M.; Teter, D. Mechanisms of hydrogen related fracture - a review. In proceedings of Second International Conference on Corrosion-Deformation Interactions-CDI '96, Nice, France, 1996, pp. 172–195.

[17] Lynch, S. Hydrogen embrittlement phenomena and mechanisms. *Corros. Rev.* 2012, *30*, 105–123, doi:10.1515/corrrev-2012-0502.

[18] Drexler, A.; Bergmann, C.; Manke, G.; Kokotin, V.; Mraczek, K.; Pohl, M.; Ecker, W. On the local evaluation of the hydrogen susceptibility of cold-formed and heat treated advanced high strength steel (AHSS) sheets. *Mater. Sci. Eng. A.* 2021, *800*, 140276, doi:10.1016/j.msea.2020.140276.

[19] Drexler, A.; Ecker, W.; Winzer, N.; Mraczek, K.; Kokotin, V.; Manke, G.; Bergmann, C. A step towards numerical evaluation of the local hydrogen susceptibility of punched and cold-formed advanced high strength steel (AHSS) sheets. In Proceeding of Steely Hydrogen, Gent, Belgium, May 29–31 2018

[20] Drexler, A.; Bergmann, C.; Manke, G.; Kokotin, V.; Mraczek, K.; Pohl, M.; Ecker, W. Local hydrogen accumulation after cold forming and heat treatment in punched advanced high strength steel sheets. Submitt. to *J. Alloys Compd.* 2020.

[21] Murakami, Y.; Yokoyama, N.N.; Takai, K. Fatigue. Effect of Hydrogen Trapped by Inclusions on Ultra-Long Life Fatigue Failure of Bearing Steel. *J. Soc. Mater. Sci. Jpn.* 2001, *50*, 1068–1073, doi:10.2472/jsms.50.1068.

[22] Todoshchenko, O.; Yagodzinskyy, Y.; Yagodzinska, V.; Saukkonen, T.; Hänninen, H. Hydrogen effects on fracture of high-strength steels with different micro-alloying. *Corros. Rev.* 2015, *33*, 515–527, doi:10.1515/corrrev-2015-0044.

[23] Ravichandran, K.; Dwarakadasa, E.; Kishore Some considerations on the occurrence of intergranular fracture during fatigue crack growth in steels. *Mater. Sci. Eng.* 1986, *83*, L11–L16, doi:10.1016/0025-5416(86)90188-6.

[24] Venezuela, J.; Liu, Q.; Zhang, M.; Zhou, Q.; Atrens, A. A review of hydrogen embrittlement of martensitic advanced high-strength steels. *Corros. Rev.* 2016, *34*, 153–186, doi:10.1515/corrrev-2016-0006.

[25] DePover, T.; Escobar, D.M.P.; Wallaert, E.; Zermout, Z.; Verbeken, K. Effect of hydrogen charging on the mechanical properties of advanced high strength steels. *Int. J. Hydrog. Energy* 2014, *39*, 4647–4656, doi:10.1016/j.ijhydene.2013.12.190.

[26] DePover, T.; Wallaert, E.; Verbeken, K. Fractographic analysis of the role of hydrogen diffusion on the hydrogen embrittlement susceptibility of DP steel. *Mater. Sci. Eng. A* 2016, *649*, 201–208, doi:10.1016/j.msea.2015.09.124.

[27] McCoy, R.A.; Gerberich, W.W.; Zackay, V.F. On the resistance of TRIP steel to hydrogen embrittlement. *Met. Mater. Trans. A* 1970, *1*, 2031–2034, doi:10.1007/bf02642820.

[28] Davies, R.G. Hydrogen embrittlement of dual-phase steels. *Met. Mater. Trans. A* 1981, *12*, 1667–1672, doi:10.1007/bf02643572.

[29] Duprez, L.; Verbeken, K.; Verhaege, M. Effect of hydrogen on the mechanical properties of multiphase high strength steels. In Proceedings of the 2008 International Hydrogen Conference: Effects of hydrogen on materials. Jackson, WY, USA, 07–10 September 2008, pp. 62–69.

[30] Ronevich, J.A.; Speer, J.G.; Matlock, D.K. Hydrogen Embrittlement of Commercially Produced Advanced High Strength Sheet Steels. *Sae Int. J. Mater. Manuf.* 2010, *3*, 255–267, doi:10.4271/2010-01-0447.

[31] DePover, T.; Laureys, A.; Escobar, D.P.; Eeckhout, E.V.D.; Wallaert, E.; Verbeken, K. Understanding the Interaction between a Steel Microstructure and Hydrogen. *Materials.* 2018, *11*, 698, doi:10.3390/ma11050698.

[32] Malitckii, E.; Yagodzinskyy, Y.; VilaçaP. Role of retained austenite in hydrogen trapping and hydrogen-assisted fatigue fracture of high-strength steels. *Mater. Sci. Eng. A* 2019, *760*, 68–75, doi:10.1016/j.msea.2019.05.103.

[33] Loidl, M.; Kolk, O.; Veith, S.; Gobel, T. Characterization of hydrogen embrittlement in automotive advanced high strength steels. *Mater. Und Werkst.* 2011, *42*, 1105–1110, doi:10.1002/mawe.201100917.

[34] Rehrl, J.; Mraczek, K.; Pichler, A.; Werner, E. Mechanical properties and fracture behavior of hydrogen charged AHSS/UHSS grades at high- and low strain rate tests. *Mater. Sci. Eng. A* 2014, *590*, 360–367, doi:10.1016/j.msea.2013.10.044.

[35] Bhadeshia, H.K.D.H. Prevention of Hydrogen Embrittlement in Steels. *Isij Int.* 2016, *56*, 24–36, doi:10.2355/isijinternational.isijint-2015-430.

[36] E bner, A.S.; Brinckmann, S.; Plesiutschnig, E.; Clemens, H.; Pippan, R.; Maier-Kiener, V. A Modified Electrochemical Nanoindentation Setup for Probing Hydrogen-Material Interaction Demonstrated on a Nickel-Based Alloy. *Jom.* 2020, *72*, 1–10, doi:10.1007/s11837-020-04104-9.

[37] Wan, D.; Deng, Y.; Meling, J.I.H.; Alvaro, A.; Barnoush, A. Hydrogen-enhanced fatigue crack growth in a single-edge notched tensile specimen under in-situ hydrogen charging inside an

environmental scanning electron microscope. *Acta Mater.* 2019, *170*, 87–99, doi:10.1016/j.actamat.2019.03.032.

[38] DePover, T.; Hajilou, T.; Wan, D.; Wang, D.; Barnoush, A.; Verbeken, K. Assessment of the potential of hydrogen plasma charging as compared to conventional electrochemical hydrogen charging on dual phase steel. *Mater. Sci. Eng. A* 2019, *754*, 613–621, doi:10.1016/j.msea.2019.03.097.

[39] Kim, J.; Tasan, C.C. Microstructural and micro-mechanical characterization during hydrogen charging: An in situ scanning electron microscopy study. *Int. J. Hydrog. Energy* 2019, *44*, 6333–6343, doi:10.1016/j.ijhydene.2018.10.128.

[40] Massone, A.; Manhard, A.; Jacob, W.; Drexler, A.; Ecker, W.; Hohenwarter, A.; Wurster, S.; Kiener, D. An SEM compatible plasma cell for in situ studies of hydrogen-material interaction. *Rev. Sci. Instrum.* 2020, *91*, 043705, doi:10.1063/1.5142043.

[41] Maier, V.; Durst, K.; Mueller, J.; Backes, B.; Höppel, H.W.; Göken, M. Nanoindentation strain-rate jump tests for determining the local strain-rate sensitivity in nanocrystalline Ni and ultrafine-grained Al. *J. Mater. Res.* 2011, *26*, 1421–1430, doi:10.1557/jmr.2011.156.

[42] Toh, T.; Baldwin WM. Ductility of steel with varying concentrations of hydrogen. In: Stress corrosion cracking and embrittlement; Robertson, W. D., Ed.; Wiley, NY, USA, 1956, pp. 176–186.

[43] Shu, W.; Okuno, K.; Hayashi, Y. Ion-driven permeation of deuterium in metals. *Jaeri-M.* 1993, *43*, 1–62.

[44] Mutzke, A.; Schneider, R.; Eckstein, W.; Dohmen, R.; Schmid, K.; von Toussaint, U.; Badelow, G. SDTrimSP Version 6.00 (IPP 2019-2). Max-Planck-Institut für Plasmaphysik, Garching, 2019, 1–92

[45] Zhou, H.; Hirooka, Y.; Ashikawa, N.; Muroga, T.; Sagara, A. Gas- and plasma-driven hydrogen permeation through a reduced activation ferritic steel alloy F82H. *J. Nucl. Mater.* 2014, *455*, 470–474, doi:10.1016/j.jnucmat.2014.07.061.

[46] Baskes, M. A calculation of the surface recombination rate constant for hydrogen isotopes on metals. *J. Nucl. Mater.* 1980, *92*, 318–324, doi:10.1016/0022-3115(80)90117-8.

[47] Barrera, O.; Tarleton, E.; Tang, H.; Cocks, A. Modelling the coupling between hydrogen diffusion and the mechanical behaviour of metals. *Comput. Mater. Sci.* 2016, *122*, 219–228, doi:10.1016/j.commatsci.2016.05.030.

[48] Fischer, F.; Mori, G.; Svoboda, J. Modelling the influence of trapping on hydrogen permeation in metals. *Corros. Sci.* 2013, *76*, 382–389, doi:10.1016/j.corsci.2013.07.010.

[49] Dassault Systemes, ABAQUS User's Manual 2016.

[50] Svoboda, J.; Fischer, F. Modelling for hydrogen diffusion in metals with traps revisited. *Acta Mater.* 2012, *60*, 1211–1220, doi:10.1016/j.actamat.2011.11.025.

[51] Drexler, A.; Siegl, W.; Tkadletz, M.; Ecker, W.; Mori, G.; Svoboda, J.; Fischer, F. D. Cycled hydrogen permeation through Armco iron – a joint experimental and modeling approach. *Corros. Sci.* 2020, *176*, 109017 DOI: 10.1016/j.corsci.2020.109017

[52] Svoboda, J.; Mori, G.; Prethaler, A.; Fischer, F. Determination of trapping parameters and the chemical diffusion coefficient from hydrogen permeation experiments. *Corros. Sci.* 2014, *82*, 93–100, doi:10.1016/j.corsci.2014.01.002.

[53] Drexler, A.; DePover, T.; Verbeken, K.; Ecker, W. Model-based interpretation of thermal desorption spectra of Fe-C-Ti alloys. *J. Alloy. Compd.* 2019, *789*, 647–657, doi:10.1016/j.jallcom.2019.03.102.

[54] Drexler, A.; DePover, T.; Leitner, S.; Verbeken, K.; Ecker, W. Microstructural based hydrogen diffusion and trapping models applied to Fe–C X alloys. *J. Alloy. Compd.* 2020, *826*, 154057, doi:10.1016/j.jallcom.2020.154057.

[55] Alturk, R.; Mates, S.; Xu, Z.; Abu-Farha, F. Effects of Microstructure on the Strain Rate Sensitivity of Advanced Steels. In Proceedings of the 3rd Pan American Materials Congress; Springer Science and Business Media LLC, San Diego, CA, USA, 26 February–2 March, 2017; pp. 243–254.

[56] Canale, L.C.; Yao, X.; Gu, J.; Totten, G. A historical overview of steel tempering parameters. *Int. J. Microstruct. Mater. Prop.* 2008, *3*, 474, doi:10.1504/ijmmp.2008.022033.

[57] Grange, R.A.; Hribal, C.R.; Porter, L.F. Hardness of tempered martensite in carbon and low-alloy steels. *Met. Mater. Trans. A* 1977, *8*, 1775–1785, doi:10.1007/bf02646882.

[58] Pharr, G.M.; Herbert, E.G.; Gao, Y. The Indentation Size Effect: A Critical Examination of Experimental Observations and Mechanistic Interpretations. *Annu. Rev. Mater. Res.* 2010, *40*, 271–292, doi:10.1146/annurev-matsci-070909-104456.

[59] Zakroczymski, T.; Glowacka, A.; Swiatnicki, W. Effect of hydrogen concentration on the embrittlement of a duplex stainless steel. *Corros. Sci.* 2005, *47*, 1403–1414, doi:10.1016/j.corsci.2004.07.036.

[60] Selwyn, G. S. Optical diagnostic techniques for rie. In Proceedings of the sixth symposium on Plasma Processing, San Diego, CA, USA, October 1986. Mathad, G. S., Schwartz, G.C., Gottscho, R.A., Eds; Pennington, NJ, USA, 1987, 220–253.

[61] Lynch, S. Mechanistic and fractographic aspects of stress corrosion cracking. *Corros. Rev.* 2012, *30*, 105–123, doi:10.1515/corrrev-2012-0501.

[62] Thompson, A.W. The behavior of sensitized 309S stainless steel in hydrogen. *Mater. Sci. Eng.* 1974, *14*, 253–264, doi:10.1016/0025-5416(74)90106-2.

[63] Stenerud, G.; Wenner, S.; Olsen, J.S.; Johnsen, R. Effect of different microstructural features on the hydrogen embrittlement susceptibility of alloy 718. *Int. J. Hydrog. Energy* 2018, *43*, 6765–6776, doi:10.1016/j.ijhydene.2018.02.088.

[64] Tiwari, G.; Bose, A.; Chakravartty, J.; Wadekar, S.; Totlani, M.; Arya, R.; Fotedar, R. A study of internal hydrogen embrittlement of steels. *Mater. Sci. Eng. A* 2000, *286*, 269–281, doi:10.1016/s0921-5093(00)00793-0.

[65] Marchi, C.S.; Somerday, B.; Tang, X.; Schiroky, G. Effects of alloy composition and strain hardening on tensile fracture of hydrogen-precharged type 316 stainless steels. *Int. J. Hydrog. Energy* 2008, *33*, 889–904, doi:10.1016/j.ijhydene.2007.10.046.

[66] Matsuo, T.; Yamabe, J.; Matsuoka, S.; Murakami, Y. Influence of Hydrogen and Prestrain on Tensile Properties of Type 316L Austenitic Stainless Steel. In Proceedings of the 2008 International Hydrogen Conference: Effects of hydrogen on materials. Jackson, WY, USA, 07–10 September 2008, pp. 105–112.

[67] Thompson, A.W. Ductile fracture topography: Geometrical contributions and effects of hydrogen. *Met. Mater. Trans. A* 1979, *10*, 727–731, doi:10.1007/bf02658394.

[68] Takai, K.; Watanuki, R. Hydrogen in Trapping States Innocuous to Environmental Degradation of High-strength Steels. *Isij Int.* 2003, *43*, 520–526, doi:10.2355/isijinternational.43.520.

[69] Robertson, I.M.; Sofronis, P.; Nagao, A.; Martin, M.L.; Wang, S.; Gross, D.W.; Nygren, K.E. Hydrogen Embrittlement Understood. *Met. Mater. Trans. A* 2015, *46*, 1085–1103, doi:10.1007/s11663-015-0325-y.

[70] Brewer, L.; Othon, M.; Young, L.; Angeliu, T. Misorientation Mapping for Visualization of Plastic Deformation via Electron Back-Scattered Diffraction. *Microsc. Microanal.* 2006, *12*, 85–91, doi:10.1017/s1431927606060120.

[71] Gao, L.; Manhard, A.; Jacob, W.; Von Toussaint, U.; Balden, M.; Schmid, K. High-flux hydrogen irradiation-induced cracking of tungsten reproduced by low-flux plasma exposure. *Nucl. Fusion* 2019, *59*, 056023, doi:10.1088/1741-4326/ab0915.

C. Prospects of enhancing the understanding of material-hydrogen interaction by novel in-situ and in-operando methods

A. Massone[1,2,*], D.Kiener[2]

1. Materials Center Leoben, Forschungs GmbH, Roseggerstrasse 12, 8700 Leoben, Austria
2. Department Materials Science, Chair of Materials Physics, Montanuniversität Leoben, Jahnstrasse 12, 8700 Leoben, Austria

Abstract

A main scientific and technical challenge facing the implementation of new and sustainable energy sources is the development and improvement of materials and components. In order to provide commercial viability of these applications, an intensive research in material-hydrogen (H) interaction is required. This work provides an overview of recently developed in-situ and in-operando H-charging methods and their applicability to investigate mechanical properties, H-absorption characteristics and H embrittlement (HE) susceptibility of a wide range of materials employed in H-related technologies, such as subsea oil and gas applications, nuclear fusion and fuel cells.

C. 1. Introduction

The increasing demand for energy supply leads to the necessity of providing more sustainable energy sources. The main energy sources used nowadays include coal, oil, natural gas and nuclear energy [115]. These energy sources are largely responsible of global warming as carbon dioxide (CO_2) is emitted from these fossil fuels. To reduce greenhouse emissions, it is necessary to find an alternative to the present fossil fuel technologies, and many political and technological measures have been adopted throughout the world to decrease the amount of CO_2.

H is expected to play a key role as a potential future energy source. It can be generated from renewable sources and produces electricity when reacting with oxygen in fuel cells, being water the only by-product [116]. Fuel cells are formed by two electrodes, which are separated by a solid or liquid electrolyte or membrane. H (or a H-containing fuel) and oxygen are fed into the anode and cathode of the fuel cell, respectively, and electrochemical reactions assisted by catalysts take place at the electrodes. The electrolyte or membrane enables the transport of ions between the electrodes, and the electrons flowing through an external circuit provide, in this way, an electrical current [116]. H based electrical energy has many advantages over other energy sources: Higher efficiency (65%)

compared to diesel (45%) or gasoline (22%), higher specific energy content than gasoline and diesel and, as mentioned above, it produces only renewable waste [117].

With the introduction of H as an energy source, H technology plays an important role in many applications, and the interaction between H and the materials used in such applications needs to be considered and investigated to ensure a successful technology implementation. For instance, in comparison with other fuels, H is difficult to store and transport. In this scenario, H storage is considered as one of the most crucial and technically challenging barriers to the widespread use of H as an effective energy carrier [118]. As such, a future H economy will require two types of storage systems: one for transportation and one for stationary applications.

For transportation applications, the material should be capable of containing a high weight per cent and a high-volume density of H, and also be able to rapidly absorb and desorb it at room environment conditions. Ideally, such material should be created using low energy-preparation methods, have a good thermal conductivity, be safe and reusable on exposure to air, and have the ability to be recycled and reused [116].

There are several different established storage methods [119], which can be categorized either as physical storage (compressed gas and cryogenic storage) or as storage in solid materials (physisorption and chemical storage). Materials used in physical storage applications are mainly selected for their mechanical properties in order to improve the structure of the vessels. While chemical storage materials are selected primarily for their physical properties [120].

Nuclear fusion energy is another potential alternative for electric power generation. Compared to energy produced by combustion, nuclear fission can produce about ten million times more energy [13]. In addition to high specific energy, nuclear energy has the advantage of not releasing CO_2 into the atmosphere. Another advantage is that the fuel can be reprocessed and reused, conserving natural resources. The downside of this technology is that long-term storage of nuclear waste is an issue [13]. The selection of candidate materials for advanced nuclear reactors require a thorough understanding of their performance under severe environmental conditions combined with radiation damage [121].

Oil and gas production also play a key role in the growing energy demand. Even though this source is not renewable, this industry sector is still popular and important reserves of oil and gas are left to be discovered and exploited. With the depletion of the continental shelf reserves, offshore exploration and production is moving to ultra deepwater. These are usually challenging locations and under extreme environments, facing high pressure and/or high temperature [122]–[124], and require the development of new materials, methodologies and technologies.

As can be anticipated from the requirements mentioned above, in conjunction with the tendency of H to cause material embrittlement, the main scientific and technical challenges facing the described potential energy sources are cost reduction and increased durability of materials and components. This requires an intense research regarding the development of improved or new materials, to provide commercial viability of these applications.

Small-scale testing of materials has gained prominence, initially by providing a methodology to examine small material volumes [125] . This was widely explored and opened new possibilities to study mechanical properties and deformation mechanisms of materials. For example, Korte et al. [126] performed micropillar compression to examine the plastic flow of individual phases. Studying plasticity in brittle materials requires the suppression of cracking. By making micropillars with diameters in the order of a micron, not only cracking is suppressed, but also it is possible to produce singly crystals test samples [127], [128]. With this testing method, they were able to study the differences in flow behavior in different hard phases. Furthermore, ion beam radiation damage has been investigated [129] by combining nano-compression with in-situ observation of the deformation behavior. Due to the limited penetration depth of ions, testing small volumes is essential to assess the properties of ion beam irradiated materials. Micropillar compression can also be used to study individual phases. For instance, Jun et al. [130] investigated the local strain rate sensitivity of the ⍰ phase in a dual-phase Ti alloy. Since deformation of Ti alloys is elastically and plastically rather anisotropic at the grain scale [131], the strain rate sensitivity could differ with grain orientation and slip systems, making the local investigation using small-scale testing crucial. Micropillar compression has also been used to analyze different deformation mechanisms by designing micropillars with specific orientation and microstructure [132], allowing examination of variable deformation mechanisms in non-trivial crystal structures.

To study nanostructured materials, such as thin films, small-scale testing methods are designated as best suited approaches to provide valuable insights into the mechanical behavior. Glechner et al. [133] investigated the mechanical properties of transition-metal carbide and nitrides using various micromechanical testing methods. They carried out nanoindentation, uniaxial compression tests on nano-pillars and bending tests on nano-cantilever beams. In this way, they were able to compare the mechanical behaviour of different thin films. Furthermore, small-scale testing can be used for local property mapping, for example using nanoindentation. This technique can be a very useful in the study of the effects of H on deformation since it is very localized and can be used to test small volumes. Maier-Kiener et al. [134] performed nanoindentation testing to analyze the phase stability of a nanocrystalline high-entropy alloy by detecting phase decomposition via changes in hardness, Young's modulus and strain rate sensitivity. Spherical nanoindentation can also be used to examine local flow properties by converting hardness to representative stress in materials with small internal-length scales [135]. Local processes and details happening during crack propagation can also be studied with micromechanical testing. For example, recently Burtscher et al. [136] tested miniaturized notched cantilevers to investigate the effect of different interface types on crack propagation.

It can be anticipated that small-scale testing offers a wide number of possibilities to study deformation mechanisms. The present work will give an overview of the suitability and potential implementation of different recently developed small-scale in-situ and in-operando H-charging methods to study the interaction of H with a wide range of materials that are currently used in H-related applications, such as structural and gas applications, H storage, in the automotive industry, among others. Fig. 1 depicts a scheme of the applicability of the methods in the mentioned applications. Notably, due to their versatile nature, they can be used to study the mechanical properties, H absorption characteristics and HE susceptibility of almost any material.

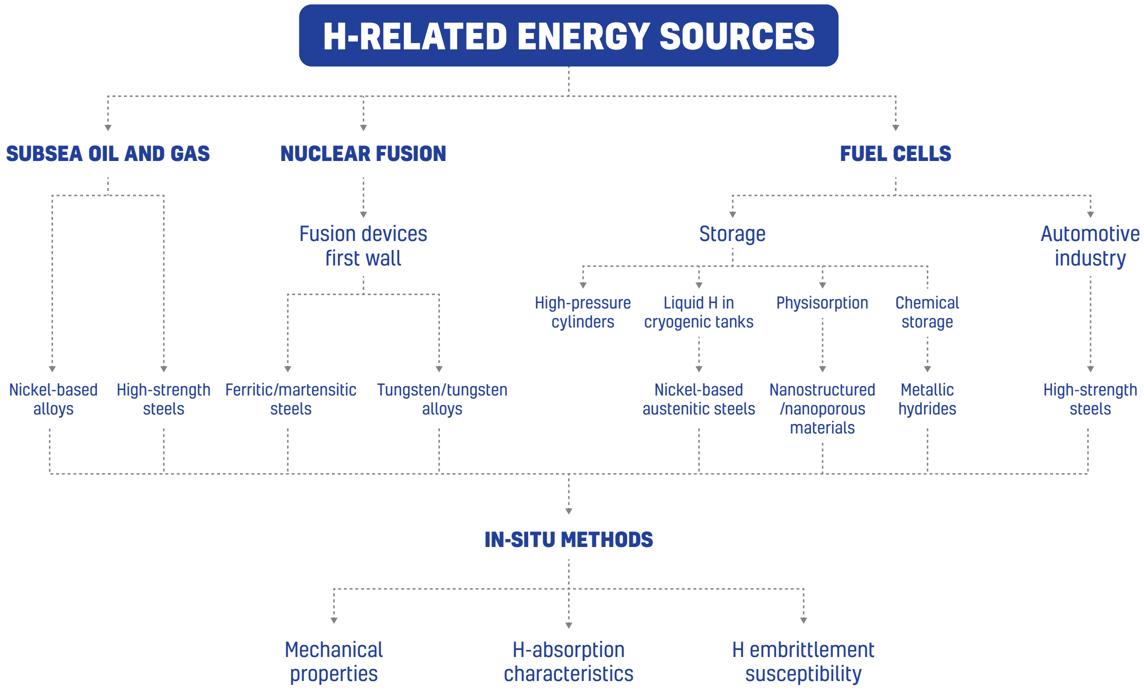

Figure 1. Applicability of in-situ methods to materials used in H-related applications

C. 2. Current status of in-situ and in-operando methods for studying H effect on materials

To study the interaction between H and any material, environmental, mechanical and material aspects should be well defined [45] in order to ensure a conclusive analysis. One of the first in-situ studies controlling these three factors was performed by Vehoff et al. [137]. They developed a bulk method for studying crack propagation under a controlled environment and controlled plastic strain conditions. Nevertheless, it was only defined for macroscopic single crystals with specific orientation and challenging to apply on complex microstructures. Robertson, Birnbaum and Sofronis [62], [90] also developed an in-situ approach for small scale investigations using straining experiments in an environmental transmission electron microscope (TEM). With this technique it was possible to directly observe the effect of H on dislocations, which seems to play an important role in HE of metals [45]. However, there were some uncertainties in the experimental conditions of their approach. For instance, the interpretation of crack growth was difficult, as the electron beam dissociated the H molecules, making the environmental conditions not defined well enough, and although the observation was with high-resolution, the field of view was limited to the transparent region of the sample, which is typically in the μm regime.

Following the in-situ approaches, another micro- and nanoscale mechanical testing method widely used in studying HE is the combination of electrochemical charging with nanoindentation testing [41], [45], [82], [83], [85], [93], [94], as shown in Fig. 2a. Nanoindentation is capable of resolving dislocation nucleation in samples with low dislocation density. Furthermore, this technique offers noticeable advantages such as the possibility to perform multiple tests within a single grain. And even though the volume of deformation is small, it is large enough to activate multiple slip systems under the indenter [82]. The primary focus of most of these studies was on the effect of H on the pop-in load in the load-displacement curves, which corresponds to the homogeneous dislocation nucleation at the onset of plasticity. These dislocations are nucleated from dislocation-free material. However, this analysis only applies for coarse-grained materials with a low dislocation density.

With nanoindentation it is also possible to investigate the effect of H on the hardness and Young's modulus of the materials. The evaluation of the effect of H on hardness can be correlated to the effect of H on dislocation mobility as well as solid solution strengthening or softening. Ebner et al. [83] developed a method, Fig. 2b, to perform electrochemical nanoindentation tests with continuous stiffness measurement, which allows a continuous measurement of Young's modulus and hardness over indentation depth. With such measurement, information on external influences, such as frame stiffness or depth-dependent properties in more complex material systems can be obtained.

Even though these approaches combine in-situ H charging and mechanical testing, it is not possible to have high-resolution observation during the tests to investigate the effect of H on the microstructure. Kim et al. [92] developed an in-situ technique to perform both microstructural and mechanical analysis during electrochemical H permeation, as depicted in Fig. 2c. During electrochemical charging, liquid electrolytes can contaminate sample surfaces by corrosion. Therefore, they charge the samples from the bottom surface to provide an objective surface without contamination for high-resolution observation. They used their technique to perform H mapping, investigate H-induced phase transformation, and conducted in situ nanoindentation with a scanning electron microscopy (SEM). H distribution influences the damage nucleation, which plays an important role in HE susceptibility. For instance, in materials with more than one phase, such as duplex stainless steels consisting of ferrite and austenite, the H diffusivity differs largely in both phases. Knowledge of the H distribution and the preferred diffusion paths, for example employing silver decoration [138], [139], can help to detect the weak phases or features in the microstructure. Furthermore, real-time SEM imaging during H charging can provide the observation of phase transformations, while EBSD analysis can document the formation of hydrides in hydride forming materials. Moreover, with in-situ H charging and in-situ nanoindentation in an SEM, the effect of H on mechanical properties at a specific microstructural feature of interest can be investigated.

Deng et al. [73], [91] performed in-situ micro-cantilever bending tests with nanoindentation in an environmental SEM (ESEM) to have a full observation of potential H effects on the deformation process and microstructure evolution on a FeAl alloy, Fig. 2d. Atomic H was produced by the reaction of Al with water vapor, which was used as the default environment in the ESEM. Micro-cantilever bending tests with in-situ H charging provide a good compromise by using micro-sized samples, small enough to capture H effects, while at the same time having enough volume capacity to avoid the disadvantages from ETEM tests, which do not ensure a certain constant strain/stress state and can have proximity effects since smaller samples are used. The downside of their method is that it is only applicable to materials that produce atomic H by reaction with water vapor. Hajilou et al. [75] also performed micro-cantilever bending tests, in this case with an in-situ miniaturized electrochemical charging cell, to investigate the effect of H on the crack propagation of notched micro-cantilevers. To maintain the dimensional integrity avoiding local corrosion on the sample, they used a glycerol electrolyte instead of aqueous solutions. With their approach, they were able to confine the H interaction with the sample to a localized region in the vicinity of the notch and allow to observation of the H effect with high resolution.

Another strategy of in-situ testing to allow high-resolution observation during mechanical testing is with H-plasma charging [80], [81], [89], [95]. Wan et al. [81] developed an in-situ method using low pressure H-plasma in an ESEM chamber to allow in-situ mechanical testing with in-situ H charging. They connected a plasma cleaner to the SEM chamber, and a H generator was connected to the working gas inlet of the plasma cleaner, as shown in Fig. 2e. A tensile specimen was then installed into a tensile/compression module. The limitation in their method is to have an in-situ observation by using normal SEM mode. Due to high flammability of H, they had to evacuate the chamber before imaging. Therefore, rather than in-situ imaging, it was limited to in-situ in position and ex-situ in environment. An important advantage of their charging method is that, since the plasma phase is not directly injected on the specimen surface, the surface would have the least possible damage from exposure to plasma and only the active particles could take part in the reaction. With their method, they were able to perform tensile tests as well as fatigue crack growth experiments.

Massone et al. [80] also performed in-situ studies using plasma charging. Their method, depicted in Fig. 2f, also consists of in-situ mechanical testing and in-situ H charging in the SEM. An in-situ observation using the SEM is in this case possible while charging. They built a miniaturized plasma cell in which a plasma is ignited through a radio frequency discharge. The tensile sample, acting as the grounded electrode of the setup, is charged from the bottom, leaving a contamination-free top surface for SEM observation, similar to the unidirectional charging approach in reference [92]. A disadvantage of these two concepts, where the samples are charged in a unidirectional way, is that a H concentration gradient is created, with the objective surface having the lowest concentration. Nonetheless, a constant supply of H leads to a dynamic equilibrium of the H concentration, thereby the charging time to detect H effects on the objective surface depends on the thickness of the sample and the H diffusivity. A difference between the methods from references [80] and [92] is that in the first case, the sample can be tested until fracture, since the plasma turns off automatically when the sealing of the plasma cell is lost. In the second case, on the other hand, only non-destructive mechanical tests can be conducted since the sample isolates the electrolyte from the vacuum environment.

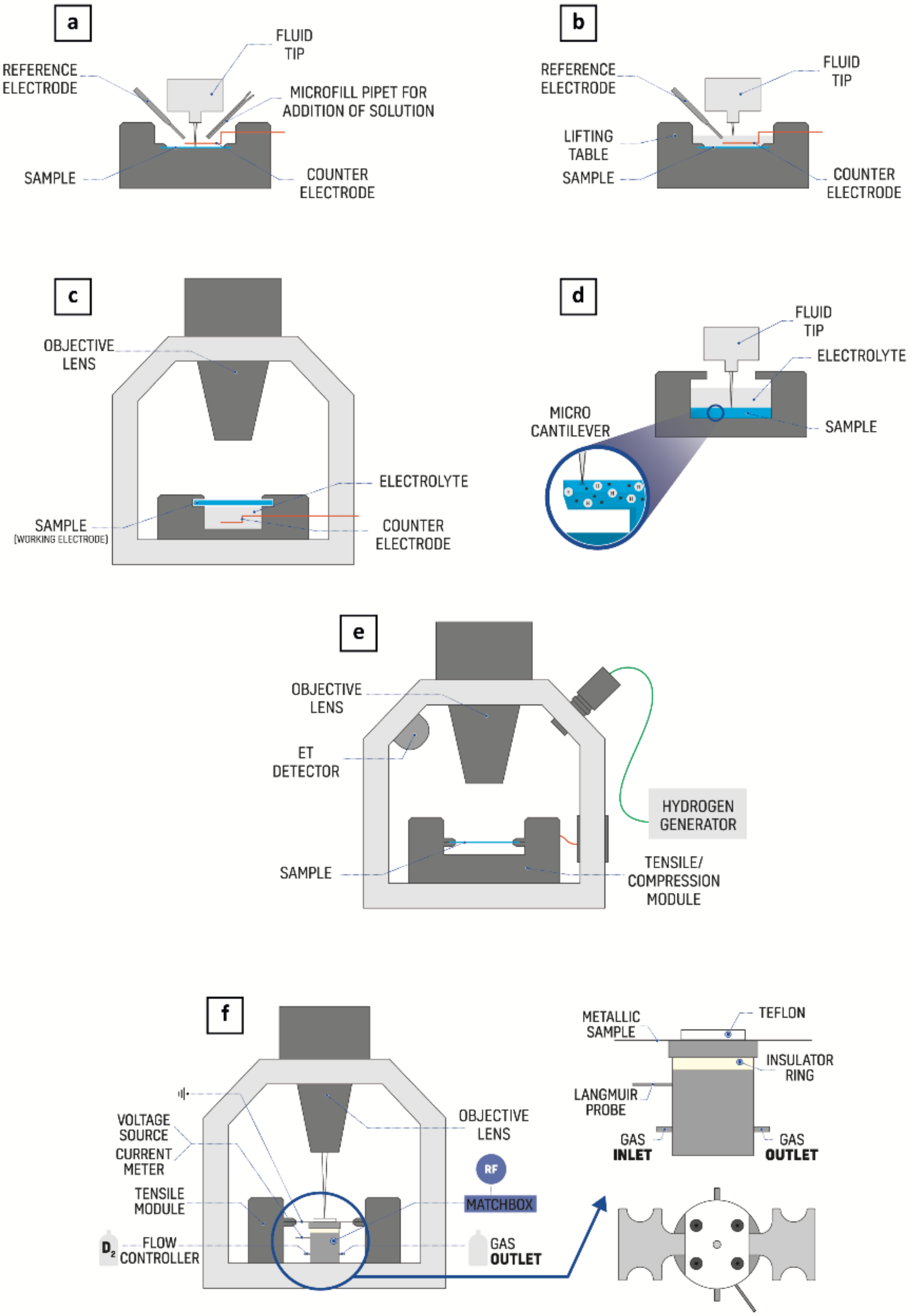

Figure 2. Schemes on in-situ H methods. (a) Nanoindentation combined with electrochemical charging. (b)Modified version of electrochemical nanoindentation test. (c) Electrochemical nanoindentation inside an

SEM. (d) Microcantilever bending test inside an ESEM. (e) Tensile test combined with H-plasma inside an ESEM. (f) Tensile test with a miniaturized plasma cell inside an SEM

C. 3. H absorption mechanisms

In order to study H-material interactions, it is instructive to understand the different involved supply methods and their limits. The sources of H in the previously described methods are either via electrochemical charging or through H plasma. In electrochemical charging, H evolution reaction may proceed through the following reaction steps in a neutral/alkaline solution [140]:

$$H_2O + M + e^- \leftrightarrow MH_{ads} + OH^+ \quad \text{Volmer} \quad (1)$$

$$MH_{ads} + H_2O + e^- \leftrightarrow H_2 + OH^- + M \quad \text{Heyrovsky} \quad (2)$$

Equation 1 corresponds to H adsorption, which is followed by electrochemical, equation 2, desorption reactions. The last step of the process is the absorption of H from the surface to the bulk. Fig. 3 shows a scheme of the H evolution reaction in these two steps during electrochemical charging in a neutral/alkaline solution. By controlling the electrolyte solution concentration, the potential and current density and the charging time, different H concentrations can be obtained.

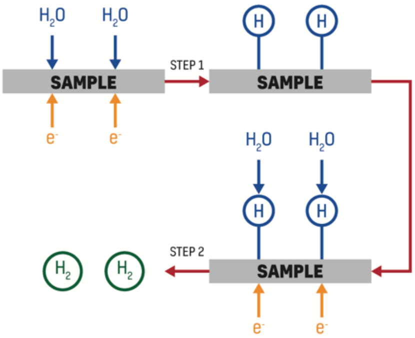

Figure 3. H evolution reaction in Volmer-Heyrovsky mechanism during electrochemical charging

In plasma charging, on the other side, ion-driven permeation (IDP) takes place. This differs from electrochemical H absorption and gas-driven permeation (GDP) in the way by which H isotopes enter the material. In GDP, the molecules of H_2 must be adsorbed on the surface, dissociate and be absorbed in the bulk, resulting in a comparatively small permeation rate. On the contrary, in IDP H ions enter the bulk with excess energy, resulting in a comparatively large permeation rate [141]. Depending on the relative rate of recombination (R) and diffusion (D) on both sides of the samples, one in contact with plasma and the other subjected to observation, the IDP process of H isotopes can be divided into three categories.

- RR regime: Rate limited by recombination on both sample sides.

- RD regime: Rate limited by recombination on the plasma-exposed side and diffusion on the observation side.

- DD regime: Rate limited by diffusion on both sides.

Usually, the maximum permeation flux appears in the RR regime and the minimum in the DD regime, respectively. The IDP transport regime of H isotopes depends on the incident ion flux and parameters of the plasma-exposed side (mean implantation depth, recombination coefficient and diffusion coefficient), as well as parameters of the other side (sample thickness, recombination coefficient and diffusion coefficient)

Fig. 4 shows schematically the H concentration profile for electrochemical charging (a) and the IDP model at steady-state (b) across the thickness of the material. In the IDP model, Φ_i is the incident ion flux, Φ_r is the reflected flux and Φ_p the permeated flux. In steady-state, the condition $\Phi_i = \Phi_r + \Phi_p$ is obeyed.

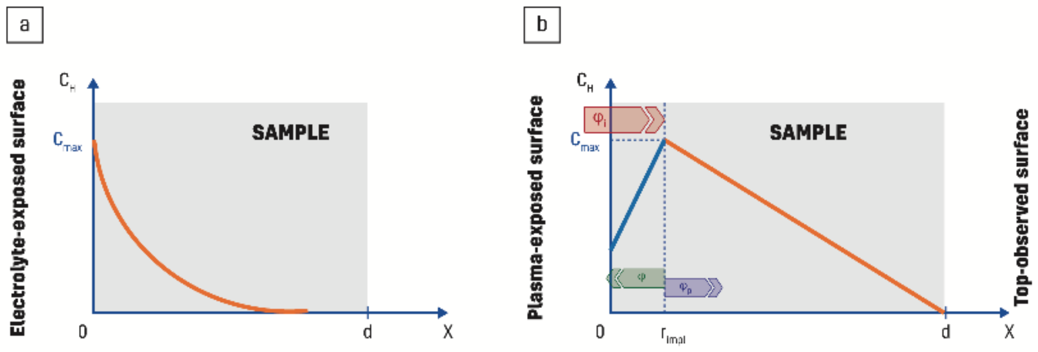

Figure 4. H concentration profile for (a) an electrochemical charged sample and (b) the model of ion-driven permeation at steady-state with plasma charging

Equations 4 and 5 show the maximum concentration for RR/RD and DD regimes, respectively.

$$C_{RR/RD} = \sqrt{\frac{\varphi_i}{k_f}} \qquad (4)$$

$$C_{DD} = \frac{r_{impl}\varphi_i}{D_f} \qquad (5)$$

Hereby, ϕ_i is the incident flux, k_f a recombination coefficient, r_{impl} the mean implantation depth and D_f the diffusion coefficient. The equations for RR and RD regimes are the same since usually the recombination coefficient on the plasma-exposed side is much larger than on the observation side [141].

As shown in Fig. 4b, the maximum H concentration for IDP appears at a distance $x=r_{impl}$ (mean implantation depth), which can be calculated using for example a Monte-Carlo program [97]. The maximum concentration depends only on the incident ion flux and the parameters at the plasma-exposed side (r_{impl}, k_f and D). The parameters on the observation side do not affect the maximum concentration at steady-state. Since the other side of the plasma-charged surface in [80] is under vacuum, the concentration on the top-observed surface is considered to be 0.

Baskes et al. [100] classified the metals as exothermic metals (e.g. Zr and Ti), which have no entry barrier for an H atom entering the bulk; or endothermic metals (e.g. Ni, Fe, Al), where the barrier is the sum of the solution and diffusion activation energies. For exothermic metals, surface recombination is the rate-limiting step and large bulk concentrations may be easily obtained. Contrarily, surface recombination is not the limiting step for the endothermic metals. Fig. 5 depicts the recombination constant and H concentration as a function of inverse temperature for various metals for an ion flux of 10^{16} $m^{-2}s^{-1}$ [100]. Notably, this is the same flux expected with the plasma cell from the method described in reference [80]. It is shown in Fig. 5 that exothermic metals, such as Zr and Ti, can reach a much higher surface concentration than their endothermic counterparts.

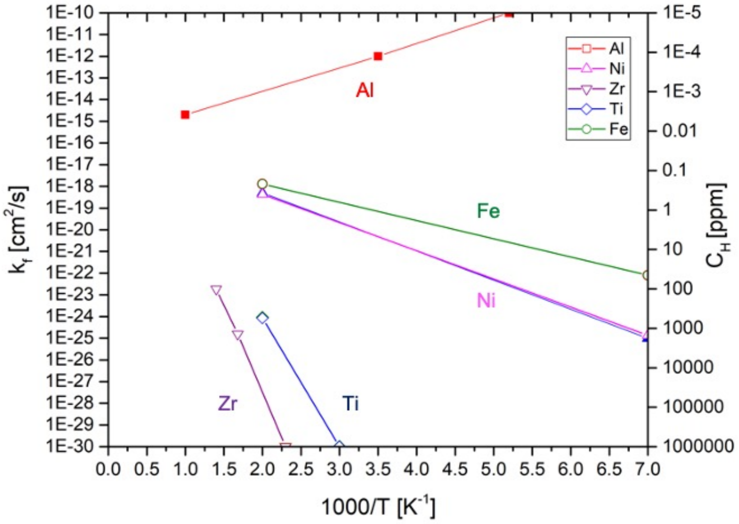

Figure 5. Recombination constant k_f as a function of inverse of temperature for various metals and H concentration for an ion flux of 10^{16} $m^{-2}s^{-1}$. This figure has been reproduced from [100] with the author's consent.

This analytical model by Baskes [100] has been applied to the in-situ H plasma charging method from [80] and compared with simulation results [96], and it has been confirmed that the simulated concentration of lattice H shows a very good agreement with the analytical calculation. Nevertheless, it is important to mention that this model only considers the solute fraction concentration. When considering the total concentration, i.e., H stored in interstitial lattice positions and H in traps, the values tend to be higher. Therefore, the following calculations of H absorption will correspond to a lower bound of the expected total concentration, since any material with lattice defects can trap H. For instance, interfaces of non-metallic inclusions are strong trapping sites for H with high trap activation energy; while lattice imperfections, grain boundaries, dislocations and microvoids are shallow traps [142].

The respective recombination coefficient k_f for the concentrations corresponding to RR/RD regimes was calculated according to reference [99]:

$$k_f = 4.8\, x\, 10^{-21} \exp\left(\frac{0.48\,(eV)}{kT}\right) \quad (6)$$

where k is the Boltzmann constant and T the temperature.

Table 1 shows the calculated H concentrations using equations 4-6 for different materials at room temperature, while Fig. 6 depicts the transport regimes as function of temperature for a list of materials for an ion flux of 10^{20} m^{-2} s^{-1}. The materials in Table 1 were classified by their transport regime according to Fig. 6. Nevertheless, both lattice concentrations from equations 4 and 5 are displayed. It can be seen that all H concentration values corresponding to the DD regime are larger than the other regimes. The transport parameters with the corresponding regime determination depend on the temperature and the ion flux [141]. Therefore, it is not possible to determine a specific transport regime for each material. For a general overview, at temperatures below ~100°C, for example, W, Al, Mo and Ni, among others, exhibit a DD characteristic and therefore, a higher H concentration is expected in these materials in comparison with the other materials in Table 1.

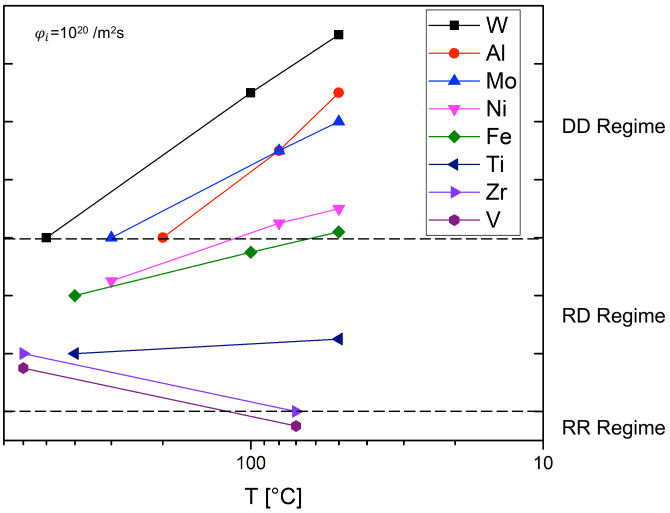

Figure 6. Transport regimes as a function of temperature for various materials [141], [143]. This figure has been reproduced with the author's consent.

Table 1. Lattice H concentrations for RR/RD and DD permeation regimes

	Material	$C_{lattice}$ RR/RD [wppm]	$C_{lattice}$ DD [wppm]
DD regime	*Al*	2.1E-04	11760.1
	Mo	5.6E-05	0.8
	Ni	6.4E-05	734.3
	W	3.0E-05	466.5
RD/RR regimes	*Fe*	7.3E-05	8.1E-04
	Mg	3.3E-04	2.6E-03
	Pd	4.8E-05	0.2
	Pt	2.7E-05	0.1
	Ti	1.3E-04	3.5
	V	9.4E-05	1.1E-02
	Zr	8.8E-05	67.4
	Zircaloy	8.8E-05	27.4

Asadipoor et al. [144] analysed the effect of H on a dual phase steel using ex-situ electrochemical charging, in-situ H-plasma charging and the combination of both. They demonstrated that with in-situ H-plasma charging, ductile fracture modes dominated over brittle modes, while with ex-situ electrochemical charging the brittle features were dominant. This indicated that plasma charging provides a lower H concentration than electrochemical charging. Nevertheless, as shown in Table 1, the upper limit of the range corresponding to the DD permeation regime is for most materials in the range of some wppm and thus high enough to produce an effect. This critical concentration to induce an observable H effect depends on the material, and not only on the strength level but also on the stress concentration factor [145].

C. 4. Applicability of novel in-situ methods towards challenges in H-related energy sources

4.1. Subsea oil and gas

The first group of H-related energy sources shown in Fig. 1 corresponds to subsea oil and gas applications. Both nickel-based alloys and high-strength steels are among the most widely used materials in the oil and gas industry due to their outstanding mechanical properties and corrosion resistance. Deep wells that face corrosive environments, combined with high temperature and high pressure require high-strength materials with sufficient corrosion resistance that can withstand this harsh conditions [146]. Although Ni alloys fulfil these requirements, they are highly susceptible to HE [22], [33], [43], [104], [111], [112]. Both solution annealed and aged conditions suffer a ductility loss in the presence of H, being the aged condition the most affected one. Even though the effect of H on Ni-based alloys has been widely studied [22], [33], [43], [83], [102], [104], [111], [112], it is still an ongoing research and the implementation of the recently developed in-situ methods could provide detailed information concerning the identification of the susceptible microstructural features and related modification to improve the alloys accordingly, thereby maximizing strength while avoiding detrimental H effects.

4.2. Nuclear fusion

Nuclear fusion has a very attractive potential to offer an environmentally friendly and safe energy source. A fusion power plant is free from concern of exhaustion of fuels and production of CO_2. Furthermore, the product of the fusion reaction is helium, which is not radioactive, limiting the nuclear waste only to structural materials with neutron-induced activation [147]. Despite its advantages, there are still scientific and technological problems that have to be solved before the successful commercialisation of fusion power. Among these, a challenge is the selection and development of the plasma facing materials, which will experience extreme heat and particle flux [148]. Plasma facing materials have two main roles, the protection of the first wall from high particle flux and the transportation of thermal energy away from the surface. Therefore, the selected materials should have high thermal conductivity and high resistance to erosion by particle bombardment [14].

Tungsten (W) is among the few possible plasma-facing candidate materials for the first wall of fusion devices [149]. It has very low solubility for H, high resistance to sputtering, high thermal conductivity and a high melting point. The amount of H that can be permanently retained in W is determined by the microstructure and the defect density in the material [150], [151]. These defects act as trap sites for H, while excess solute H diffuses out even at room temperature. Radiation damage, either by incident H ions or by fast neutrons from the deuterium fusion reaction, can increase the natural defect density [149]. In this way, the number of trap sites is for H retention is increased. The ions produce damage only in the near-surface regions due to saturation of the implantation zone leading to high stress fields, which produce cracks and gas-filled cavities [152]. These defects degrade the thermo-mechanical stability and also act as trap sites for H.

To study the suitability of W and W alloys as plasma-facing materials, the in-situ plasma charging methods from references [81] and [80] can be used to simulate real (or close to real) conditions. In reference [80], deuterium plasma with different bias voltages can be ignited, giving the possibility to analyse the effect of different plasma parameters on the tungsten-based materials. Also, the mechanical properties can be investigated, allowing the characterization of crack growth behaviour and the mechanical stability after ion implantation. For instance, Yoon et al. [16] reported that W heavy alloys can suffer HE during the sintering process under H atmosphere. They showed that the elongation and UTS decreased in the presence of H, but the mechanical properties were restored by a heat treatment in vacuum. On the other hand, Li et al. [108] did not see any obvious HE effect on the W heavy alloy specimen after deuterium implantation under the analysed conditions. Nevertheless, they stated that the mechanism of deuterium transport and retention in tungsten heavy alloys is still not well understood and the impact of deuterium implantation could vary under different experimental conditions. For this reason, the application of the in-situ plasma charging methods to investigate the embrittlement effect under different plasma conditions would provide valuable insights.

4.3. Fuel cell technology

Materials suitable for H storage have to meet specific requirements in order to be used in the development of H-based technologies. In order to improve and maximize the efficiency of H storage systems, the characteristics and properties of the used materials, such as chemical composition, structure and morphology, and their thermodynamic and kinetic properties, have to be deeply understood [153]. In this context, the described in-situ methods could provide valuable information regarding the mechanical properties, the microstructural characterization and H-absorption characteristics of potentially suitable materials.

4.3.1. Storage

Liquid H in cryogenic tanks

When considering the scheme from Fig. 1, the first group of materials for H storage suitable for implementing in-situ H charging methods are nickel-based austenitic steels. These are good candidates for the structural materials used in H storage systems based on liquid H, for components of fuel cell vehicles and stationary fuel cell systems and for equipment for H stations, H pipelines and transport systems [76], [154]. In these systems, there is a direct exposure to high-pressure H and thus the austenitic stainless steels can suffer HE. Furthermore, austenitic stainless steels with low Ni content are generally metastable and form α’-martensite during deformation [155]. It has been reported that these steels are more susceptible to HE due to the faster H transport through the stress-induced martensite near the crack tip [18], [34], [76], [113], [114], [154], [156], [157]. Even though the presented methods cannot exactly simulate the operating conditions under high-pressure H gas, as they use electrochemical or plasma charging, they can provide a detailed analysis of the microstructure evolution under deformation, a thorough examination of the H-material interaction and related changes in the deformation and failure processes not easily accessible from post-mortem inspections.

Chemical storage

Metallic hydrides are the materials of choice used for chemical H storage. When comparing with liquid H storage, storage by absorption as chemical compounds has definite advantages from the safety perspective, since energy input is required to release H. Furthermore, metal hydrides have higher H-storage density than H gas or liquid H [158]. Liquid H requires an additional refrigeration unit to maintain a cryogenic state, adding weight and energy costs, resulting in a 40% energy loss [159].

Typical materials used in this application have the form MH, MH_2 and MH_3, with H fitting into octahedral or tetrahedral sites in the lattice or a combination of both, and also metallic hydrides of intermetallic compounds with the form AB_xH_n. The variation of elements allows tailoring the properties. Element A is usually a rare earth metal and tends to form a stable hydride. Element B is a transition metal and forms only unstable hydrides. This element plays a catalytic role in enhancing the hydriding/dehydriding characteristics, it can alter the equilibrium pressures for the H absorption/desorption, and it should enhance the stability of the alloys. Some examples of intermetallic compounds suited to form metallic hydrides are $LaNi_5$, ZrV_2, $ZrMn_2$, $TiMn_2$, $CeNi_3$, YFe_3, Y_2Ni_7, Th_2Fe_7, Y_6Fe_{23}, TiFe, ZrNi, Mg_2Ni, Ti_2Ni [153].

Hydride forming elements such as Ti, V and Zr are typically dominated by a RR or RD H transport regime at room temperature (Fig. 5). Therefore, a rather low H lattice concentration is expected with plasma charging in these materials, as shown in Table 1. The typical storage density of hydride materials is around 1.3-1.5% in weight of H [160], which is equivalent to 13000-15000 wppm. This means that the gravimetric capacity of metal hydrides is much larger than the total amount of H that can be supplied by the previously mentioned methods. Nevertheless, they can provide the possibility to study characteristics of H-absorption and their relation with the materials microstructure, as the hydride formation will cause local modifications and potential damage in the material microstructure. Furthermore, assessment between different microstructural features in terms of H-absorption and hydride formation, as well as a comparison between different materials and alloys is possible and would benefit alloy selection microstructure design.

4.3.2. Automotive industry

The implementation of fuel cell technology in the automotive market is currently gaining worldwide popularity due to higher fuel efficiency, longer driving range and fast refuelling of fuel cell [5]. The next group of materials in the scheme in Fig. 1 represents high-strength steels. These are excellent candidates for the automotive industry, since they combine light weight and high strength, two essential characteristics in this industry. However, high strength steels are sensitive to HE and the higher the strength, the larger the susceptibility of the material. Their use is mainly limited by H, since it can reduce their ultimate tensile strength, ductility, fatigue strength and/or fracture toughness [27]. H uptake in autobody components can already result from assembling and/or finishing processes. Usually, advanced high strength steels are electroplated with a sacrificial metal, and H can be absorbed during this coating deposition. H can also be absorbed if the sacrificial coating corrodes during service and the exposed areas start acting as cathodic sites [28]. Moreover, during the painting process, cathodic reactions in water solution take place [161]. In this process, H is generated and part of it can be absorbed and diffuse into the steel. Lovicu et al. [88] analysed the H concentration after a real production cycle (phosphatizing, electrodeposition and curing) in four types of advanced high-strength steels and showed that all samples absorbed less than 0.4 wppm. This value is lower than the usual critical concentrations, which are approximately between 1 and 4 wppm [88], suggesting a safe use to build body-in-white components. Nevertheless, the H uptake ability as well as the critical H concentrations to produce embrittlement are different for each steel.

Most of the studies made on high-strength steels are performed using ex-situ H charging [9], [17], [31], [39], [86], [88], [162], [163] with the consequent risk of H outgassing taking place before testing the material, in particular in the case of steels with fast H-diffusion, such as ferritic grades. Therefore, this approach introduces an inherent error source that can alter the results.

Kim et al. [92] applied the electrochemical in-situ setup for a duplex stainless steel and a ferritic stainless steel. Even though they did not control the H concentration in the materials, they detected the presence of H at the objected surface of the duplex stainless steel using the silver decoration technique and saw an effect of H on the mechanical properties of the ferritic stainless steel. This proves that enough H can be absorbed even in fast diffusion steels via electrochemical charging to cause HE effects.

Considering the values of H lattice concentration with plasma charging in Table 1 for Fe, it can be seen that they are in the order of 10^{-5}-10^{-4} wppm. Nevertheless, as mentioned before, these correspond only to the lattice concentration, and the total value including traps is expected to be higher. For example, in reference [96] the total H concentration was calculated for a complex phase steel, resulting in 0.82 wppm, which was around a factor of 350 higher than the corresponding lattice H. This means that the plasma charging method from reference [80] provides a higher H concentration than the one expected in the painting process, opening the possibility to study H effect on steels in a condition similar to a real production cycle.

C. 5. Conclusions

The current status of in-situ H-charging methods has been reviewed, demonstrating their applicability to study the interaction of H with different materials used in a wide range of industrial applications. With the necessity of new renewable energy sources based on H, it is essential to understand its effect on materials that must perform under H atmospheres. The described methods are based on in-situ electrochemical or plasma charging combined with mechanical testing, and in some cases even allow for in-situ observation. Each of them has their own limitations and advantages, but all of them can provide previously inaccessible novel information of the effect of H on metallic materials. As such, they should be considered as valuable tools in our road towards a green energy society.

Acknowledgments

The authors gratefully acknowledge the financial support under the scope of the COMET program within the K2 Center "Integrated Computational Material, Process and Product Engineering (IC-MPPE)" (Project No 859480). This program is supported by the Austrian Federal Ministries for Climate Action, Environment, Energy, Mobility, Innovation and Technology (BMK) and for Digital and Economic Affairs (BMDW), represented by the Austrian research funding association (FFG), and the federal states of Styria, Upper Austria and Tyrol. DK acknowledges funding by the European Research Council (ERC) under the European Union's Horizon 2020 research and innovation program, grant agreement No. 771146 (TOUGHIT).

C. 6. References

[1] "International Energy Agency." https://www.iea.org/data-and-statistics?country=WORLD&fuel=Energy supply&indicator=TPESbySource (accessed Mar. 19, 2021).

[2] M. Z. Jacobson, W. G. Colella, and D. M. Golden, "Atmospheric science: Cleaning the air and improving health with hydrogen fuel-cell vehicles," *Science (80-.).*, vol. 308, no. 5730, pp. 1901–1905, 2005, doi: 10.1126/science.1109157.

[3] E. T. Sayed *et al.*, "Direct urea fuel cells: Challenges and opportunities," *J. Power Sources*, vol. 417, no. January, pp. 159–175, 2019, doi: 10.1016/j.jpowsour.2018.12.024.

[4] R. O'Hayre, S.-W. Cha, W. G. Colella, and F. B. Prinz, *Fuel Cell Fundamentals*, Third Edit. New Jersey: Wiley, 2016.

[5] A. G. Olabi, T. Wilberforce, and M. A. Abdelkareem, "Fuel cell application in the automotive industry and future perspective," *Energy*, vol. 214, p. 118955, 2021, doi: 10.1016/j.energy.2020.118955.

[6] S. S. Hsieh, B. S. Her, and Y. J. Huang, "Effect of pressure drop in different flow fields on water accumulation and current distribution for a micro PEM fuel cell," *Energy Convers. Manag.*, vol. 52, no. 2, pp. 975–982, 2011, doi: 10.1016/j.enconman.2010.08.025.

[7] S. Fukuyama, M. Imade, and K. Yokogawa, “Development of new material testing apparatus in high-pressure hydrogen and evaluation of hydrogen gas embrittlement of metals,” 2007, doi: https://doi.org/10.1115/PVP2007-26820.

[8] Jari, “Technical standards for components (valve and PRD) for compressed-hydrogen vehicle fuel device,” 2004.

[9] L. Duprez, K. Verbeken, and M. Verhaege, “Effect of hydrogen on the mechanical properties of multiphase high-strength steels,” in *International Hydrogen Conference: Effects of hydrogen on materials*, 2008.

[10] J. Sanchez, S. F. Lee, M. A. Martin-Rengel, J. Fullea, C. Andrade, and J. Ruiz-Hervías, “Measurement of hydrogen and embrittlement of high strength steels,” *Eng. Fail. Anal.*, vol. 59, pp. 467–477, 2016, doi: 10.1016/j.engfailanal.2015.11.001.

[11] M. Loidl, O. Kolk, S. Veith, and T. Göbel, “Characterization of hydrogen embrittlement in automotive advanced high strength steels,” *Materwiss. Werksttech.*, vol. 42, no. 12, pp. 1105–1110, 2011, doi: 10.1002/mawe.201100917.

[12] C. Bergmann *et al.*, “Hydrogen embrittlement resistance evaluation of advanced high strength steels in automotive applications,” *SteelyHydrogen*, no. 1, p. A01, 2018, [Online]. Available: http://steelyhydrogen2018proc.be/articles/pdf/1.

[13] E. J. Ben Anthony, *Handbook of climate change mitigation*, vol. 4. 2016.

[14] D. M. Duffy, “Modeling plasma facing materials for fusion power,” *Mater. Today*, vol. 12, no. 11, pp. 38–44, 2009, doi: 10.1016/S1369-7021(09)70297-4.

[15] J. Linke *et al.*, “Challenges for plasma-facing components in nuclear fusion,” *Matter Radiat. Extrem.*, vol. 4, no. 5, 2019, doi: 10.1063/1.5090100.

[16] H. K. Yoon, S. H. Lee, S. J. L. Kang, and D. N. Yoon, “Effect of vacuum-treatment on mechanical properties of W-Ni-Fe heavy alloy,” *J. Mater. Sci.*, vol. 18, no. 5, pp. 1374–1380, 1983, doi: 10.1007/BF01111957.

[17] T. Depover, D. Pérez Escobar, E. Wallaert, Z. Zermout, and K. Verbeken, “Effect of hydrogen charging on the mechanical properties of advanced high strength steels,” *Int. J. Hydrogen Energy*, vol. 39, no. 9, pp. 4647–4656, 2014, doi: 10.1016/j.ijhydene.2013.12.190.

[18] T. Michler, C. San Marchi, J. Naumann, S. Weber, and M. Martin, “Hydrogen environment embrittlement of stable austenitic steels,” *Int. J. Hydrogen Energy*, vol. 37, no. 21, pp. 16231–16246, 2012, doi: 10.1016/j.ijhydene.2012.08.071.

[19] M. Koyama, C. C. Tasan, E. Akiyama, K. Tsuzaki, and D. Raabe, “Hydrogen-assisted decohesion and localized plasticity in dual-phase steel,” *Acta Mater.*, vol. 70, pp. 174–187, 2014, doi: 10.1016/j.actamat.2014.01.048.

[20] T. Kanezaki, C. Narazaki, Y. Mine, S. Matsuoka, and Y. Murakami, “Effects of hydrogen on fatigue crack growth behavior of austenitic stainless steels,” *Int. J. Hydrogen Energy*, vol. 33, no. 10, pp. 2604–2619, 2008, doi: 10.1016/j.ijhydene.2008.02.067.

[21] Z. Zhang, G. Obasis, R. Morana, and M. Preuss, “Hydrogen assisted crack initiation and propagation in a nickel-based superalloy,” *Acta Mater.*, vol. 113, pp. 272–283, 2016, doi: 10.1016/j.actamat.2016.05.003.

[22] Z. Tarzimoghadam, D. Ponge, J. Klöwer, and D. Raabe, “Hydrogen-assisted failure in Ni-based superalloy 718 studied under in situ hydrogen charging: The role of localized deformation in crack propagation,” *Acta Mater.*, vol. 128, pp. 365–374, 2017, doi: 10.1016/j.actamat.2017.02.059.

[23] J. He, S. Fukuyama, K. Yokogawa, and A. Kimura, “Effect of hydrogen on deformation structure of Inconel 718,” *Materials Transactions, JIM*, vol. 35, no. 10. pp. 689–694, 1994, doi: 10.2320/matertrans1989.35.689.

[24] M. F. Maday and L. Pilloni, “Hydrogen effects on the tensile and fatigue properties of Eurofer’97,” *Fusion Eng. Des.*, vol. 75–79, no. SUPPL., pp. 957–961, 2005, doi: 10.1016/j.fusengdes.2005.06.024.

[25] S. Lynch, “Hydrogen embrittlement phenomena and mechanisms,” *Corros. Rev.*, vol. 30, no. 3–4, pp. 105–123, 2012, doi: 10.1515/corrrev-2012-0502.

[26] J. Cwiek, “Prevention to hydrogen degradation of steel,” *Solid State Phenom.*, vol. 183, no. 1, pp. 31–36, 2012, doi: 10.4028/www.scientific.net/SSP.183.31.

[27] M. R. Louthan, “Hydrogen embrittlement of metals: A primer for the failure analyst,” *J. Fail. Anal. Prev.*, vol. 8, no. 3 SPEC. ISS., pp. 289–307, 2008, doi: 10.1007/s11668-008-9133-x.

[28] D. Figueroa and M. J. Robinson, “The effects of sacrificial coatings on hydrogen embrittlement and re-embrittlement of ultra high strength steels,” *Corros. Sci.*, vol. 50, no. 4, pp. 1066–1079, 2008, doi: 10.1016/j.corsci.2007.11.023.

[29] W. H. Johnson, “On some remarkable changes produced in iron and steel by the action of hydrogen and acids,” *Nature*, vol. 11, no. 281, p. 393, 1875, doi: 10.1038/011393a0.

[30] Y. Momotani, A. Shibata, D. Terada, and N. Tsuji, “Hydrogen Embrittlement Behavior at Different Strain Rates in Low-carbon Martensitic Steel,” *Mater. Today Proc.*, vol. 2, no. December, pp. S735–S738, 2015, doi: 10.1016/j.matpr.2015.07.387.

[31] J. Rehrl, K. Mraczek, A. Pichler, and E. Werner, “Mechanical properties and fracture behavior of hydrogen charged AHSS/UHSS grades at high- and low strain rate tests,” *Mater. Sci. Eng. A*, vol. 590, pp. 360–367, 2014, doi: 10.1016/j.msea.2013.10.044.

[32] J. Venezuela, Q. Liu, M. Zhang, Q. Zhou, and A. Atrens, “A review of hydrogen embrittlement

of martensitic advanced high-strength steels," *Corros. Rev.*, vol. 34, no. 3, pp. 153–186, 2016, doi: 10.1515/corrrev-2016-0006.

[33] F. Galliano, E. Andrieu, C. Blanc, J. M. Cloue, D. Connetable, and G. Odemer, "Effect of trapping and temperature on the hydrogen embrittlement susceptibility of alloy 718," *Mater. Sci. Eng. A*, vol. 611, pp. 370–382, 2014, doi: 10.1016/j.msea.2014.06.015.

[34] G. Han, S. He, S. Fukuyama, and K. Yokogawa, "Effect of Nickel Equivalent on Hydrogen Environment Embrittlement of Austenitc Stainless Steels at Low Temperatures," *Acta Mater.*, vol. 46, no. 13, pp. 4599–4570, 1998.

[35] S. P. Lynch, "Environmentally assisted cracking: Overview of evidence for an adsorption-induced localised-slip process," *Acta Metall.*, vol. 36, no. 10, pp. 2639–2661, 1988, doi: 10.1016/0001-6160(88)90113-7.

[36] R. G. Davies, "Hydrogen Embrittlement of Dual-Phase Steels.," *Metall. Trans. A, Phys. Metall. Mater. Sci.*, vol. 12 A, no. 9, pp. 1667–1672, 1981, doi: 10.1007/BF02643572.

[37] P. D. Hicks and C. J. Altstetter, "Hydrogen-enhanced cracking of superalloys," *Metall. Trans. A*, vol. 23, no. 1, pp. 237–249, 1992, doi: 10.1007/BF02660868.

[38] N. Eliaz, A. Shachar, B. Tal, and D. Eliezer, "Characteristics of hydrogen embrittlement, stress corrosion cracking and tempered martensite embrittlement in high-strength steels," *Eng. Fail. Anal.*, vol. 9, no. 2, pp. 167–184, 2002, doi: 10.1016/S1350-6307(01)00009-7.

[39] D. Hardie, E. A. Charles, and A. H. Lopez, "Hydrogen embrittlement of high strength pipeline steels," *Corros. Sci.*, vol. 48, no. 12, pp. 4378–4385, 2006, doi: 10.1016/j.corsci.2006.02.011.

[40] M. Wang, E. Akiyama, and K. Tsuzaki, "Effect of hydrogen on the fracture behavior of high strength steel during slow strain rate test," *Corros. Sci.*, vol. 49, no. 11, pp. 4081–4097, 2007, doi: 10.1016/j.corsci.2007.03.038.

[41] A. Barnoush and H. Vehoff, "Hydrogen embrittlement of aluminum in aqueous environments examined by in situ electrochemical nanoindentation," *Scr. Mater.*, vol. 58, no. 9, pp. 747–750, 2008, doi: 10.1016/j.scriptamat.2007.12.019.

[42] J. Sanchez, J. Fullea, C. Andrade, and P. De Andres, "Hydrogen embrittlement of high strength steels," *Defect Diffus. Forum*, vol. 289–292, pp. 203–209, 2009, doi: 10.4028/www.scientific.net/DDF.289-292.203.

[43] X. Lu, D. Wang, D. Wan, Z. B. Zhang, N. Kheradmand, and A. Barnoush, "Effect of electrochemical charging on the hydrogen embrittlement susceptibility of alloy 718," *Acta Mater.*, vol. 179, no. 7491, pp. 36–48, 2019, doi: 10.1016/j.actamat.2019.08.020.

[44] S. K. Dwivedi and M. Vishwakarma, "Hydrogen embrittlement in different materials: A review," *Int. J. Hydrogen Energy*, vol. 43, no. 46, pp. 21603–21616, 2018, doi:

10.1016/j.ijhydene.2018.09.201.

[45] A. Barnoush and H. Vehoff, “Recent developments in the study of hydrogen embrittlement: Hydrogen effect on dislocation nucleation,” *Acta Mater.*, vol. 58, no. 16, pp. 5274–5285, 2010, doi: 10.1016/j.actamat.2010.05.057.

[46] H.K.D.H. Bhadeshia, “Prevention of Hydrogen Embrittlement in Steels,” *ISIJ Int.*, vol. 56, no. 1, pp. 24–36, 2016.

[47] J. Woodtli and R. Kieselbach, “Damage due to hydrogen embrittlement and stress corrosion cracking,” *Eng. Fail. Anal.*, vol. 7, no. 6, pp. 427–450, 2000, doi: 10.1016/S1350-6307(99)00033-3.

[48] S. V. Brahimi, S. Yue, and K. R. Sriraman, “Alloy and composition dependence of hydrogen embrittlement susceptibility in high-strength steel fasteners,” *Philos. Trans. R. Soc. A Math. Phys. Eng. Sci.*, vol. 375, no. 2098, 2017, doi: 10.1098/rsta.2016.0407.

[49] S. E. Brahimi, “Fundamentals of Hydrogen Embrittlement in Steel Fasteners,” *IBECA Technol. Corp*, pp. 1–23, 2014.

[50] D. M. Symons, “A comparison of internal hydrogen embrittlement and hydrogen environment embrittlement of X-750,” *Eng. Fract. Mech.*, vol. 68, no. 6, pp. 751–771, 2001, doi: 10.1016/S0013-7944(00)00123-5.

[51] A. H. M. Krom and A. D. Bakker, “Hydrogen trapping models in steel,” *Metall. Mater. Trans. B Process Metall. Mater. Process. Sci.*, vol. 31, no. 6, pp. 1475–1482, 2000, doi: 10.1007/s11663-000-0032-0.

[52] Y. Fukai and H. Sugimoto, “Advances in Physics Diffusion of hydrogen in metals,” *Adv. Phys.*, vol. 34, no. 2, pp. 263–326, 2006.

[53] H. Wipf, “Solubility and-diffusion of hydrogen in pure metals and alloys,” *Phys. Scr. T*, vol. 94, pp. 43–51, 2001, doi: 10.1238/physica.topical.094a00043.

[54] W. Gerberich, “Gaseous hydrogen embrittlement of materials in energy technologies,” R. P. Gangloff and B. P. Somerday, Eds. Cambridge: Woodhead Publishing Limited, 2012, pp. 209–246.

[55] S. Lynch, “Discussion of some recent literature on hydrogen-embrittlement mechanisms: Addressing common misunderstandings,” *Corros. Rev.*, no. ii, 2019, doi: 10.1515/corrrev-2019-0017.

[56] W. W. Gerberich, R. A. Oriani, M. J. Lji, X. Chen, and T. Foecke, “The necessity of both plasticity and brittleness in the fracture thresholds of iron,” *Philos. Mag. A Phys. Condens. Matter, Struct. Defects Mech. Prop.*, vol. 63, no. 2, pp. 363–376, 1991, doi: 10.1080/01418619108204854.

[57] R. A. Oriani and P. H. Josephic, “Equilibrium aspects of hydrogen-induced cracking of steels,” *Acta Metall.*, vol. 22, no. 9, pp. 1065–1074, 1974, doi: 10.1016/0001-6160(74)90061-3.

[58] R. P. Gangloff, “Hydrogen Assisted Cracking of High Strength Alloys,” in *Comprehensive Structural Integrity*, I. Milne, R. O. Ritchie, and B. Karihaloo, Eds. New York: Elsevier, 2003, pp. 31–101.

[59] C. D. Beachem, “A new model for hydrogen-assisted cracking (hydrogen ‘embrittlement’),” *Metall. Trans.*, vol. 3, no. 2, pp. 441–455, 1972, doi: 10.1007/BF02642048.

[60] I. M. Robertson and H. K. Birnbaum, “An HVEM study of hydrogen effects on the deformation and fracture of nickel,” *Acta Metall.*, vol. 34, no. 3, pp. 353–366, 1986, doi: 10.1016/0001-6160(86)90071-4.

[61] I. M. Robertson *et al.*, “Hydrogen Embrittlement Understood,” *Metall. Mater. Trans. B Process Metall. Mater. Process. Sci.*, vol. 46, no. 3, pp. 1085–1103, 2015, doi: 10.1007/s11663-015-0325-y.

[62] H. K. Birnbaum and P. Sofronis, “Hydrogen-enhanced localized plasticity-a mechanism for hydrogen-related fracture,” *Mater. Sci. Eng. A*, vol. 176, no. 1–2, pp. 191–202, 1994, doi: 10.1016/0921-5093(94)90975-X.

[63] T. Tabata and H. K. Birnbaum, “Direct observation of the effect of hydrogen on the behavior of dislocations in iron,” *Scr. Metall.*, vol. 17, no. c, pp. 947–950, 1983.

[64] D. F. Teter, I. M. Robertson, and H. K. Birnbaum, “The effects of hydrogen on the deformation and fracture of β-titanium,” *Acta Mater.*, vol. 49, no. 20, pp. 4313–4323, 2001, doi: 10.1016/S1359-6454(01)00301-9.

[65] Y. Jagodzinski, H. Hänninen, O. Tarasenko, and S. Smuk, “Interaction of hydrogen with dislocation pile-ups and hydrogen induced softening of pure iron,” *Scr. Mater.*, vol. 43, no. 3, pp. 245–251, 2000, doi: 10.1016/S1359-6462(00)00398-5.

[66] G. M. Bond, I. M. Robertson, and H. K. Birnbaum, “On the determination of the hydrogen fugacity in an environmental cell TEM facility,” *Scr. Metall.*, vol. 20, pp. 653–658, 1986, [Online]. Available: https://scholar.google.co.id/scholar?hl=id&as_sdt=0%2C5&q=kemasyarakatan+bahasa+teori+firth&btnG=#d=gs_qabs&u=%23p%3DtfGdLLvHmhYJ.

[67] S. P. Lynch, “Metallographic contributions to understanding mechanisms of environmentally assisted cracking,” *Metallography*, vol. 23, no. 2, pp. 147–171, 1989, doi: 10.1016/0026-0800(89)90016-5.

[68] S. P. Lynch, “Interpreting hydrogen-induced fracture surfaces in terms of deformation processes: A new approach,” *Scr. Mater.*, vol. 65, no. 10, pp. 851–854, 2011, doi:

10.1016/j.scriptamat.2011.06.016.

[69] S. P. Lynch, “Comments on ‘A unified model of environment-assisted cracking,’” *Scr. Mater.*, vol. 61, no. 3, pp. 331–334, 2009, doi: 10.1016/j.scriptamat.2009.02.031.

[70] Y. Kim, Y. J. Chao, M. J. Pechersky, and M. J. Morgan, “On the effect of hydrogen on the fracture toughness of steel,” *Int. J. Fract.*, vol. 134, no. 3–4, pp. 339–347, 2005, doi: 10.1007/s10704-005-1974-7.

[71] J. Song and W. A. Curtin, “Atomic mechanism and prediction of hydrogen embrittlement in iron,” *Nat. Mater.*, vol. 12, no. 2, pp. 145–151, 2013, doi: 10.1038/nmat3479.

[72] B. R. S. Rogne, N. Kheradmand, Y. Deng, and A. Barnoush, “In situ micromechanical testing in environmental scanning electron microscope: A new insight into hydrogen-assisted cracking,” *Acta Mater.*, vol. 144, pp. 257–268, 2018, doi: 10.1016/j.actamat.2017.10.037.

[73] Y. Deng, T. Hajilou, D. Wan, N. Kheradmand, and A. Barnoush, “In-situ micro-cantilever bending test in environmental scanning electron microscope: Real time observation of hydrogen enhanced cracking,” *Scr. Mater.*, vol. 127, pp. 19–23, 2017, doi: 10.1016/j.scriptamat.2016.08.026.

[74] I. Taji, T. Hajilou, and F. S. A. Barnoush, “In situ electrochemical micro - cantilever bending test of Ni based superalloys,” 2019.

[75] T. Hajilou, Y. Deng, B. R. Rogne, N. Kheradmand, and A. Barnoush, “In situ electrochemical microcantilever bending test: A new insight into hydrogen enhanced cracking,” *Scr. Mater.*, vol. 132, pp. 17–21, 2017, doi: 10.1016/j.scriptamat.2017.01.019.

[76] Y. Murakami, T. Kanezaki, Y. Mine, and S. Matsuoka, “Hydrogen embrittlement mechanism in fatigue of austenitic stainless steels,” *Metall. Mater. Trans. A Phys. Metall. Mater. Sci.*, vol. 39 A, no. 6, pp. 1327–1339, 2008, doi: 10.1007/s11661-008-9506-5.

[77] H. Uyama, M. Nakashima, K. Morishige, Y. Mine, and Y. Murakami, “Effects of hydrogen charge on microscopic fatigue behaviour of annealed carbon steels,” *Fatigue Fract. Eng. Mater. Struct.*, vol. 29, no. 12, pp. 1066–1074, 2006, doi: 10.1111/j.1460-2695.2006.01069.x.

[78] Y. Ogawa, H. Matsunaga, J. Yamabe, M. Yoshikawa, and S. Matsuoka, “Unified evaluation of hydrogen-induced crack growth in fatigue tests and fracture toughness tests of a carbon steel,” *Int. J. Fatigue*, vol. 103, pp. 223–233, 2017, doi: 10.1016/j.ijfatigue.2017.06.006.

[79] H. Vehoff and P. Neumann, “Crack propagation and cleavage initiation in Fe-2.6%-Si single crystals under controlled plastic crack tip opening rate in various gaseous environments,” *Acta Metall.*, vol. 28, no. 3, pp. 265–272, 1980, doi: 10.1016/0001-6160(80)90161-3.

[80] A. Massone *et al.*, “An SEM compatible plasma cell for in situ studies of hydrogen-material interaction,” *Rev. Sci. Instrum.*, vol. 91, no. 4, 2020, doi: 10.1063/1.5142043.

[81] D. Wan, Y. Deng, and A. Barnoush, "Hydrogen embrittlement effect observed by in-situ hydrogen plasma charging on a ferritic alloy," *Scr. Mater.*, vol. 151, no. April, pp. 24–27, 2018, doi: 10.1016/j.scriptamat.2018.03.038.

[82] A. Barnoush and H. Vehoff, "In situ electrochemical nanoindentation: A technique for local examination of hydrogen embrittlement," *Corros. Sci.*, vol. 50, no. 1, pp. 259–267, 2008, doi: 10.1016/j.corsci.2007.05.026.

[83] A. S. Ebner, S. Brinckmann, E. Plesiutschnig, H. Clemens, R. Pippan, and V. Maier-Kiener, "A Modified Electrochemical Nanoindentation Setup for Probing Hydrogen-Material Interaction Demonstrated on a Nickel-Based Alloy," *Jom*, vol. 72, no. 5, pp. 2020–2029, 2020, doi: 10.1007/s11837-020-04104-9.

[84] M. J. Duarte, X. Fang, J. Rao, W. Krieger, S. Brinckmann, and G. Dehm, "In situ nanoindentation during electrochemical hydrogen charging: a comparison between front-side and a novel back-side charging approach," *J. Mater. Sci.*, 2021, doi: 10.1007/s10853-020-05749-2.

[85] A. Barnoush and H. Vehoff, "Electrochemical nanoindentation: A new approach to probe hydrogen/deformation interaction," *Scr. Mater.*, vol. 55, no. 2, pp. 195–198, 2006, doi: 10.1016/j.scriptamat.2006.03.041.

[86] X. Li, Y. Wang, P. Zhang, B. Li, X. Song, and J. Chen, "Effect of pre-strain on hydrogen embrittlement of high strength steels," *Mater. Sci. Eng. A*, vol. 616, pp. 116–122, 2014, doi: 10.1016/j.msea.2014.07.085.

[87] T. Zakroczymski, A. Glowacka, and W. Swiatnicki, "Effect of hydrogen concentration on the embrittlement of a duplex stainless steel," *Corros. Sci.*, vol. 47, no. 6, pp. 1403–1414, 2005, doi: 10.1016/j.corsci.2004.07.036.

[88] G. Lovicu *et al.*, "Hydrogen embrittlement of automotive advanced high-strength steels," *Metall. Mater. Trans. A Phys. Metall. Mater. Sci.*, vol. 43, no. 11, pp. 4075–4087, 2012, doi: 10.1007/s11661-012-1280-8.

[89] T. Depover, T. Hajilou, D. Wan, D. Wang, A. Barnoush, and K. Verbeken, "Assessment of the potential of hydrogen plasma charging as compared to conventional electrochemical hydrogen charging on dual phase steel," *Mater. Sci. Eng. A*, vol. 754, no. March, pp. 613–621, 2019, doi: 10.1016/j.msea.2019.03.097.

[90] I. M. Robertson, "The effect of hydrogen on dislocation dynamics," *Eng. Fract. Mech.*, vol. 68, no. 6, pp. 671–692, 2001, doi: 10.1016/S0013-7944(01)00011-X.

[91] Y. Deng and A. Barnoush, "Hydrogen embrittlement revealed via novel in situ fracture experiments using notched micro-cantilever specimens," *Acta Mater.*, vol. 142, pp. 236–247,

2018, doi: 10.1016/j.actamat.2017.09.057.

[92] J. Kim and C. C. Tasan, “Microstructural and micro-mechanical characterization during hydrogen charging: An in situ scanning electron microscopy study,” *Int. J. Hydrogen Energy*, vol. 44, no. 12, pp. 6333–6343, 2019, doi: 10.1016/j.ijhydene.2018.10.128.

[93] D. Wang, X. Lu, Y. Deng, X. Guo, and A. Barnoush, “Effect of hydrogen on nanomechanical properties in Fe-22Mn-0.6C TWIP steel revealed by in-situ electrochemical nanoindentation,” *Acta Mater.*, vol. 166, pp. 618–629, 2019, doi: 10.1016/j.actamat.2018.12.055.

[94] A. Barnoush, C. Bies, and H. Vehoff, “In situ electrochemical nanoindentation of FeAl (100) single crystal: Hydrogen effect on dislocation nucleation,” *J. Mater. Res.*, vol. 24, no. 3, pp. 1105–1113, 2009, doi: 10.1557/jmr.2009.0084.

[95] D. Wan, Y. Deng, J. I. H. Meling, A. Alvaro, and A. Barnoush, “Hydrogen-enhanced fatigue crack growth in a single-edge notched tensile specimen under in-situ hydrogen charging inside an environmental scanning electron microscope,” *Acta Mater.*, vol. 170, pp. 87–99, 2019, doi: 10.1016/j.actamat.2019.03.032.

[96] A. Massone *et al.*, “Addressing H-Material Interaction in Fast Diffusion Materials—a Feasibility Study on a Complex Phase Steel,” *Materials (Basel).*, vol. 13, no. 20, p. 4677, Oct. 2020, doi: 10.3390/ma13204677.

[97] A. Mutzke *et al.*, “SDTrimSP.” Max-Planck-Institut für Plasmaphysik, Garching, 2019.

[98] W. M. Shu, Y. Hayashi, and K. Okuno, “Regime diagram of plasma-driven hydrogen transport through metals,” *Philos. Mag. B Phys. Condens. Matter; Stat. Mech. Electron. Opt. Magn. Prop.*, vol. 72, no. 3, pp. 301–309, 1995, doi: 10.1080/13642819508239085.

[99] H. Zhou, Y. Hirooka, N. Ashikawa, T. Muroga, and A. Sagara, “Gas- and plasma-driven hydrogen permeation through a reduced activation ferritic steel alloy F82H,” *J. Nucl. Mater.*, vol. 455, no. 1–3, pp. 470–474, 2014, doi: 10.1016/j.jnucmat.2014.07.061.

[100] M. I. Baskes, “A calculation of the surface recombination rate constant for hydrogen isotopes on metals,” *J. Nucl. Mater.*, vol. 92, no. 2–3, pp. 318–324, 1980, doi: 10.1016/0022-3115(80)90117-8.

[101] G. Stenerud, S. Wenner, J. S. Olsen, and R. Johnsen, “Effect of different microstructural features on the hydrogen embrittlement susceptibility of alloy 718,” *Int. J. Hydrogen Energy*, vol. 43, no. 13, pp. 6765–6776, 2018, doi: 10.1016/j.ijhydene.2018.02.088.

[102] Z. Zhang, G. Obasi, R. Morana, and M. Preuss, “In-situ observation of hydrogen induced crack initiation in a nickel-based superalloy,” *Scr. Mater.*, vol. 140, pp. 40–44, 2017, doi: 10.1016/j.scriptamat.2017.07.006.

[103] Z. Tarzimoghadam *et al.*, “Multi-scale and spatially resolved hydrogen mapping in a Ni-Nb

model alloy reveals the role of the δ phase in hydrogen embrittlement of alloy 718," *Acta Mater.*, vol. 109, pp. 69–81, 2016, doi: 10.1016/j.actamat.2016.02.053.

[104] X. Lu, Y. Ma, and D. Wang, "On the hydrogen embrittlement behavior of nickel-based alloys: Alloys 718 and 725," *Mater. Sci. Eng. A*, vol. 792, no. June, 2020, doi: 10.1016/j.msea.2020.139785.

[105] L. Fournier, D. Delafosse, and T. Magnin, "Cathodic hydrogen embrittlement in alloy 718," *Mater. Sci. Eng. A*, vol. 269, no. 1–2, pp. 111–119, 1999, doi: 10.1016/S0921-5093(99)00167-7.

[106] D. K. Matlock, J. G. Speer, E. De Moor, and P. J. Gibbs, "Recent developments in advanced high strength steels for automotive applications: An overview," *Jestech*, vol. 15, no. 1, pp. 1–12, 2012.

[107] A. Drexler *et al.*, "On the local evaluation of the hydrogen susceptibility of cold-formed and heat treated advanced high strength steel (AHSS) sheets," *Mater. Sci. Eng. A*, vol. 800, no. June 2020, p. 140276, 2021, doi: 10.1016/j.msea.2020.140276.

[108] M. Li, D. Ruprecht, G. Kracker, T. Höschen, and R. Neu, "Impact of heat treatment on tensile properties of 97W–2Ni–1Fe heavy alloy," *J. Nucl. Mater.*, vol. 512, pp. 1–7, 2018, doi: 10.1016/j.jnucmat.2018.09.055.

[109] H. Maier *et al.*, "Deuterium retention in tungsten based materials for fusion applications," *Nucl. Mater. Energy*, vol. 18, no. July 2018, pp. 245–249, 2019, doi: 10.1016/j.nme.2018.12.032.

[110] A. Massone and D. Kiener, "Prospects of enhancing the understanding of material-hydrogen interaction by novel in-situ and in-operando methods," *Renew. Sustain. Energy Rev.*, 2021.

[111] L. Liu, C. Zhai, C. Lu, W. Ding, A. Hirose, and K. F. Kobayashi, "Study of the effect of δ phase on hydrogen embrittlement of Inconel 718 by notch tensile tests," *Corros. Sci.*, vol. 47, no. 2, pp. 355–367, 2005, doi: 10.1016/j.corsci.2004.06.008.

[112] V. Demetriou, J. D. Robson, M. Preuss, and R. Morana, "Study of the effect of hydrogen charging on the tensile properties and microstructure of four variant heat treatments of nickel alloy 718," *Int. J. Hydrogen Energy*, vol. 42, no. 37, pp. 23856–23870, 2017, doi: 10.1016/j.ijhydene.2017.02.149.

[113] T. Michler, A. A. Yukhimchuk, and J. Naumann, "Hydrogen environment embrittlement testing at low temperatures and high pressures," *Corros. Sci.*, vol. 50, no. 12, pp. 3519–3526, 2008, doi: 10.1016/j.corsci.2008.09.025.

[114] M. Koyama *et al.*, "Hydrogen desorption and cracking associated with martensitic transformation in Fe-Cr-Ni-Based austenitic steels with different carbon contents," *Int. J.*

Hydrogen Energy, vol. 42, no. 42, pp. 26423–26435, 2017, doi: 10.1016/j.ijhydene.2017.08.209.

[115] M. Kaur and K. Pal, “Review on hydrogen storage materials and methods from an electrochemical viewpoint,” *J. Energy Storage*, vol. 23, no. March, pp. 234–249, 2019, doi: 10.1016/j.est.2019.03.020.

[116] P. P. Edwards, V. L. Kuznetsov, and W. I. F. David, “Hydrogen energy,” *Philos. Trans. R. Soc. A Math. Phys. Eng. Sci.*, vol. 365, no. 1853, pp. 1043–1056, 2007, doi: 10.1098/rsta.2006.1965.

[117] F. Khalid, I. Dincer, and M. A. Rosen, “Analysis and assessment of an integrated hydrogen energy system,” *Int. J. Hydrogen Energy*, vol. 41, no. 19, pp. 7960–7967, 2016, doi: 10.1016/j.ijhydene.2015.12.221.

[118] G. W. Crabtree, M. S. Dresselhaus, and M. V. Buchanan, “The hydrogen economy,” *Phys. Today*, vol. 57, no. 12, pp. 39–44, 2004, doi: 10.1063/1.1878333.

[119] A. Züttel, “Materials for hydrogen storage,” *Mater. Today*, vol. 6, no. 9, pp. 24–33, 2003, doi: 10.1016/S1369-7021(03)00922-2.

[120] P. Millet, *Hydrogen storage in hydride-forming materials*. Woodhead Publishing Limited, 2014.

[121] G. R. Odette and S. J. Zinkle, *Structural alloys for nuclear energy applications*. Elsevier, 2019.

[122] J. M. Bell, Y. D. Chin, and S. Hanrahan, “State-of-the-art of ultra deepwater production technologies,” *Proc. Annu. Offshore Technol. Conf.*, vol. 2005-May, pp. 1875–1887, 2005, doi: 10.4043/17615-ms.

[123] M. Iannuzzi, A. Barnoush, and R. Johnsen, “Materials and corrosion trends in offshore and subsea oil and gas production,” *npj Mater. Degrad.*, vol. 1, no. 1, 2017, doi: 10.1038/s41529-017-0003-4.

[124] T. E. Perez, “Corrosion in the oil and gas industry: An increasing challenge for materials,” *Jom*, vol. 65, no. 8, pp. 1033–1042, 2013, doi: 10.1007/s11837-013-0675-3.

[125] M. D. Uchic, D. M. Dimiduk, J. N. Florando, and W. D. Nix, “Sample dimensions influence strength and crystal plasticity,” *Science (80-.).*, vol. 305, no. 5686, pp. 986–989, 2004, doi: 10.1126/science.1098993.

[126] S. Korte and W. J. Clegg, “Studying plasticity in hard and soft Nb-Co intermetallics,” *Adv. Eng. Mater.*, vol. 14, no. 11, pp. 991–997, 2012, doi: 10.1002/adem.201200175.

[127] F. Östlund *et al.*, “Ductile-brittle transition in micropillar compression of GaAs at room temperature,” *Philos. Mag.*, vol. 91, no. 7–9, pp. 1190–1199, 2011, doi: 10.1080/14786435.2010.509286.

[128] S. Korte, J. S. Barnard, R. J. Stearn, and W. J. Clegg, “Deformation of silicon - Insights from

microcompression testing at 25-500 °c," *Int. J. Plast.*, vol. 27, no. 11, pp. 1853–1866, 2011, doi: 10.1016/j.ijplas.2011.05.009.

[129] D. Kiener, P. Hosemann, S. A. Maloy, and A. M. Minor, "In situ nanocompression testing of irradiated copper," *Nat. Mater.*, vol. 10, no. 8, pp. 608–613, 2011, doi: 10.1038/nmat3055.

[130] T. S. Jun, Z. Zhang, G. Sernicola, F. P. E. Dunne, and T. B. Britton, "Local strain rate sensitivity of single α phase within a dual-phase Ti alloy," *Acta Mater.*, vol. 107, pp. 298–309, 2016, doi: 10.1016/j.actamat.2016.01.057.

[131] T. B. Britton, H. Liang, F. P. E. Dunne, and A. J. Wilkinson, "The effect of crystal orientation on the indentation response of commercially pure titanium: Experiments and simulations," *Proc. R. Soc. A Math. Phys. Eng. Sci.*, vol. 466, no. 2115, pp. 695–719, 2010, doi: 10.1098/rspa.2009.0455.

[132] Y. Liu *et al.*, "Experimentally quantifying critical stresses associated with basal slip and twinning in magnesium using micropillars," *Acta Mater.*, vol. 135, pp. 411–421, 2017, doi: 10.1016/j.actamat.2017.06.008.

[133] T. Glechner *et al.*, "Assessment of ductile character in superhard Ta-C-N thin films," *Acta Mater.*, vol. 179, pp. 17–25, 2019, doi: 10.1016/j.actamat.2019.08.015.

[134] V. Maier-Kiener, B. Schuh, E. P. George, H. Clemens, and A. Hohenwarter, "Nanoindentation testing as a powerful screening tool for assessing phase stability of nanocrystalline high-entropy alloys," *Mater. Des.*, vol. 115, pp. 479–485, 2017, doi: 10.1016/j.matdes.2016.11.055.

[135] A. Leitner, V. Maier-Kiener, and D. Kiener, "Essential refinements of spherical nanoindentation protocols for the reliable determination of mechanical flow curves," *Mater. Des.*, vol. 146, pp. 69–80, 2018, doi: 10.1016/j.matdes.2018.03.003.

[136] M. Burtscher, M. Alfreider, K. Schmuck, H. Clemens, S. Mayer, and D. Kiener, "In situ fracture observations of distinct interface types within a fully lamellar intermetallic TiAl alloy," 2020, doi: 10.1557/jmr.2020.306.

[137] H. Vehoff and W. Rothe, *GASEOUS HYDROGEN EMBRITTLEMENT IN FeSi- AND Ni-SINGLE CRYSTALS.*, no. 30. Pergamon Books Ltd, 1986.

[138] T. Schober and C. Dieker, "Observation of local hydrogen on nickel surfaces," *Metall. Trans. A*, vol. 14, no. 11, pp. 2440–2442, 1983, doi: 10.1007/BF02663321.

[139] M. Koyama, D. Yamasaki, T. Nagashima, C. C. Tasan, and K. Tsuzaki, "In situ observations of silver-decoration evolution under hydrogen permeation: Effects of grain boundary misorientation on hydrogen flux in pure iron," *Scr. Mater.*, vol. 129, pp. 48–51, 2017, doi: 10.1016/j.scriptamat.2016.10.027.

[140] A. Lasia and D. Grégoire, “General Model of Electrochemical Hydrogen Absorption into Metals,” *J. Electrochem. Soc.*, vol. 142, no. 10, pp. 3393–3399, 1995, doi: 10.1149/1.2050267.

[141] W. Shu, K. Okuno, and Y. Hayashi, “Ion-driven permeation of deuterium in metals,” *Jaeri-M*, vol. 43, 1993.

[142] J. Y. Lee and S. M. Lee, “Hydrogen trapping phenomena in metals with B.C.C. and F.C.C. crystals structures by the desorption thermal analysis technique,” *Surf. Coatings Technol.*, vol. 28, no. 3–4, pp. 301–314, 1986, doi: 10.1016/0257-8972(86)90087-3.

[143] B. L. Doyle and D. K. Brice, “Steady state hydrogen transport in solids,” *Radiat. Eff.*, vol. 89, no. 1–2, pp. 21–48, 1985, doi: 10.1080/00337578508220694.

[144] M. Asadipoor, J. Kadkhodapour, A. Pourkamali Anaraki, S. M. H. Sharifi, A. C. Darabi, and A. Barnoush, “Experimental and Numerical Investigation of Hydrogen Embrittlement Effect on Microdamage Evolution of Advanced High-Strength Dual-Phase Steel,” *Met. Mater. Int.*, no. 0123456789, 2020, doi: 10.1007/s12540-020-00681-1.

[145] M. Wang, E. Akiyama, and K. Tsuzaki, “Determination of the critical hydrogen concentration for delayed fracture of high strength steel by constant load test and numerical calculation,” *Corros. Sci.*, vol. 48, no. 8, pp. 2189–2202, 2006, doi: 10.1016/j.corsci.2005.07.010.

[146] H. S. Klapper, J. Klöwer, and O. Gosheva, “Hydrogen embrittlement: The game changing factor in the applicability of nickel alloys in oilfield technology,” *Philos. Trans. R. Soc. A Math. Phys. Eng. Sci.*, vol. 375, no. 2098, 2017, doi: 10.1098/rsta.2016.0415.

[147] H. Yamada, “Fusion Energy,” in *Handbook of Climate Change Mitigation*, W. Y. Chen, J. Seiner, T. Suzuki, and M. Lackner, Eds. New York: Springer US, 2012.

[148] W. Jacob, C. Linsmeier, and M. Rubel, “13th International Workshop on Plasma-Facing Materials and Components for Fusion Applications/1st International Conference on Fusion Energy Materials Science,” *Phys. Scr. T*, vol. T145, 2011, doi: 10.1088/0031-8949/2011/T145/011001.

[149] J. Roth and K. Schmid, “Hydrogen in tungsten as plasma-facing material,” *Phys. Scr. T*, vol. T145, 2011, doi: 10.1088/0031-8949/2011/T145/014031.

[150] A. Manhard, K. Schmid, M. Balden, and W. Jacob, “Influence of the microstructure on the deuterium retention in tungsten,” *J. Nucl. Mater.*, vol. 415, no. 1 SUPPL, pp. S632–S635, 2011, doi: 10.1016/j.jnucmat.2010.10.045.

[151] L. Gao *et al.*, “Deuterium supersaturation in low-energy plasma-loaded tungsten surfaces,” *Nucl. Fusion*, vol. 57, no. 1, p. 16026, 2017, doi: 10.1088/0029-5515/57/1/016026.

[152] Y. Zayachuk, A. Manhard, M. H. J. ’T Hoen, W. Jacob, P. A. Zeijlmans Van Emmichoven, and G. Van Oost, “Depth profiling of the modification induced by high-flux deuterium plasma in

tungsten and tungsten-tantalum alloys," *Nucl. Fusion*, vol. 54, no. 12, 2014, doi: 10.1088/0029-5515/54/12/123013.

[153] J. Bellosta von Colbe *et al.*, "Application of hydrides in hydrogen storage and compression: Achievements, outlook and perspectives," *Int. J. Hydrogen Energy*, vol. 44, no. 15, pp. 7780–7808, 2019, doi: 10.1016/j.ijhydene.2019.01.104.

[154] L. Zhang, M. Wen, M. Imade, S. Fukuyama, and K. Yokogawa, "Effect of nickel equivalent on hydrogen gas embrittlement of austenitic stainless steels based on type 316 at low temperatures," *Acta Mater.*, vol. 56, no. 14, pp. 3414–3421, 2008, doi: 10.1016/j.actamat.2008.03.022.

[155] J. Talonen and H. Hänninen, "Formation of shear bands and strain-induced martensite during plastic deformation of metastable austenitic stainless steels," *Acta Mater.*, vol. 55, no. 18, pp. 6108–6118, 2007, doi: 10.1016/j.actamat.2007.07.015.

[156] R. M. Vennet and G. S. Ansell, "The effect of high-pressure hydrogen upon tensile properties and fracture behavior of 304L stainless steel," *Trans. ASM*, vol. 60, pp. 242–251, 1967.

[157] R. B. Benson, R. K. Dann, and L. W. Roberts, "Hydrogen embrittlement of stainless steel," *Trans. AIME*, vol. 242, pp. 2199–2205, 1968.

[158] R. C. Weast, M. J. Astle, and W. H. Beyer, *CRC handbook of chemistry and physics*, 64th ed. Boca Raton, Florida: CRC Press, 1983.

[159] M. L. Trudeau, "Advanced Materials for Energy Storage," *MRS Bull.*, vol. 24, no. 11, pp. 23–26, Nov. 1999, doi: 10.1557/S0883769400053410.

[160] H. Yu, C. Hebling, and S. Revathi, "Fuel Cells: Microsystems," *Ref. Modul. Mater. Sci. Mater. Eng.*, no. September 2015, pp. 1–15, 2016, doi: 10.1016/b978-0-12-803581-8.01727-6.

[161] I. Krylova, "Painting by electrodeposition on the eve of the 21st century," *Prog. Org. Coatings*, vol. 42, no. 3–4, pp. 119–131, 2001, doi: 10.1016/S0300-9440(01)00146-1.

[162] Y. Liu, M. Wang, and G. Liu, "Effect of hydrogen on ductility of high strength 3Ni-Cr-Mo-V steels," *Mater. Sci. Eng. A*, vol. 594, pp. 40–47, 2014, doi: 10.1016/j.msea.2013.11.058.

[163] T. B. Hilditch, S. B. Lee, J. G. Speer, and D. K. Matlock, "Response to hydrogen charging in high strength automotive sheet steel products," *SAE Tech. Pap.*, no. 724, 2003, doi: 10.4271/2003-01-0525.